Report
R-19-07
January 2019

Gas release from the SFL repository and migration through the geosphere

Report for the safety evaluation SE-SFL

Orlando Silva
Álvaro Sáinz-García
Jorge Molinero

SVENSK KÄRNBRÄNSLEHANTERING AB

SWEDISH NUCLEAR FUEL
AND WASTE MANAGEMENT CO

Box 3091, SE-169 03 Solna
Phone +46 8 459 84 00
skb.se

SVENSK KÄRNBRÄNSLEHANTERING

ISSN 1402-3091
SKB R-19-07
ID 1608977
January 2019

Gas release from the SFL repository and migration through the geosphere

Report for the safety evaluation SE-SFL

Orlando Silva, Álvaro Sáinz-García, Jorge Molinero
Amphos 21 Consulting S.L.

Summary

The work of Silva et al. (2019) was extended to simulate migration both in the near and far field of hydrogen gas formed by anoxic corrosion of steel contained in the waste of the BHK vault of SFL.

Several 2D models have been set up, including a cross-section of the BHK vault and its surroundings. The host rock has been represented using both homogeneous and heterogeneous hydraulic properties. The heterogeneous rock models considered two cross-sections: one of low permeabilities around the vault and the other is considering high permeable well-connected zones. A deformation zone intersecting the BHK vault was considered in some simulation cases.

Simulation cases of gas flow in the near-field were performed to determine the difference between assuming homogeneous and heterogeneous host rock. They showed that similar results are obtained when the average permeability of the heterogeneous rock is close to the value assumed in the homogeneous model. Higher pressures and overpressures were found when the vault is surrounded by zones of low permeability. The average gas pressure and average overpressure in the BHK vault are lower than 54.5 and 3.0 bar, respectively.

The models of gas flow in the far-field showed that the hydrogen fluxes at the regolith-bedrock interface are controlled by the gas production rate and the permeability of the host rock. A highly heterogeneous rock below the regolith induces multi-modal distributions of hydrogen fluxes. By contrast, homogeneous rock causes unimodal distributions of gas fluxes at the regolith bottom. For the heterogeneous cross-sections considered, the dispersion of gas at the regolith is less than 400 m. Buoyancy causes most of gas to exit through the center of the regolith-bedrock interface. Moreover, the evolution of hydrogen fluxes at surface follows the dynamic of gas production within the BHK vault and reaches quasi-steady state over long periods.

The effect of large gas production rates was analyzed both at near and far field scale. The results suggest that gas flowrates in the vault and at the regolith-bedrock interface increases linearly with the production rate and reach quasi-steady state over long periods. Also, in the worst case, increasing the gas generation rate one order of magnitude increases the internal pressures by 2.0 bar.

Even considering very high gas generation rates, the gas saturations in the system are too low (below 13 %) to affect the groundwater flow.

Sammanfattning

Arbetet som presenterades i Silva et al. (2019) expanderades för att möjliggöra simulering av transport av vätgas både i när- och fjärrfältet. Vätgasen bildas genom anoxisk korrosion av det stål som finns i avfallet i bergsalen BHK i SFL.

Flera 2D-modeller har satts upp som alla inkluderar ett tvärsnitt av BHK-bergsalen och dess omgivningar. Det omgivande berget har representerats med både homogena och heterogena hydrauliska egenskaper. De heterogena bergmodellerna beaktade två typer av tvärsnitt: ett med låga permeabiliteter runt bergsalen och ett med övervägande högpermeabla väl kopplade zoner. I vissa simuleringsfall inkluderades en deformationszon som skär BHK- bergsalen.

Simuleringsfall med gasflöde i närfältet utfördes för att uppskatta skillnaden mellan att ansätta homogent eller heterogent berg i modellen. Fallen visade att liknande resultat uppnås då medelvärdet för permeabiliteten hos det heterogena berget ligger nära det värde som antas i den homogena modellen. Högre tryck och övertryck uppnåddes när bergsalen omges av zoner med låg permeabilitet. Det genomsnittliga gastrycket och det genomsnittliga övertrycket i BHK-salen är lägre än 54,5 respektive 3,0 bar.

Modellerna med gasflöde i fjärrfältet påvisade att vätgasflödet vid gränssnittet mellan regolit och bergöverytan styrs av gasproduktionen och permeabiliteten hos berget. En hög heterogenitet hos berget under regoliten inducerar multimodala fördelningar av vätgasflödet. Däremot orsakar homogent berg en homogen fördelning av gasflödet vid underytan av regoliten. För de heterogena tvärsnitten som beaktas är dispersionen av gas vid regoliten mindre än 400 m. Lyftkrafter orsakar att större delen av gasen går ut genom mitten på gränssnittet av regolit och berg. Vidare följer utvecklingen av vätgasflödet vid ytan dynamiken för gasproduktionen i BHK-salen och når kvasi-steady state under långa perioder.

Effekten av stora gasproduktionshastigheter analyserades både i när- och fjärrfältsskala. Resultaten tyder på att gasflödet i bergsalen och vid gränssnittet mellan regolit och berg ökar linjärt med produktionshastigheten samt når kvasi-steady state under långa perioder. I det mest extrema fallet, då gasgenerationshastigheten ökar en storleksordning, ökar det inre trycket med 2,0 bar.

Även då mycket höga gasgenereringshastigheter beaktas är mättnadsgraden av gas i systemet för lågt (under 13 %) för att påverka grundvattenflödet.

Nomenclature

Alphanumeric

a	absorption coefficient in the coefficient form of the PDE module of COMSOL
c	diffusion coefficient in the coefficient form of the PDE module of COMSOL
d	damping coefficient in the coefficient form of the PDE module of COMSOL
e	mass coefficient in the coefficient form of the PDE module of COMSOL
f	source term in the coefficient form of the PDE module of COMSOL
g	gravity acceleration, 9.8 m/s^2
J	"boundary flux" internal function of COMSOL (kg/m^2 s)
k	permeability of the rock (m^2)
k	permeability tensor (m^2)
m	van Genuchten parameter (dimensionless)
n	van Genuchten parameter (dimensionless)
n	unit vector normal to surface Σ
N	number of components
P	pressure (Pa)
ΔP	overpressure (Pa)
q	specific discharge of a phase (m/s)
Q	mass sink/source term of a component in a phase (kg/m^3 s); inflow/outflow rates of gas and water from the BHK vault (m^3/year); total gas mass flowrate through the regolith-bedrock interface (kg/s)
r	hydrogen generation rate (kg/m^3 s); steel corrosion rate (μm/year)
S	saturation of a phase (dimensionless); surface area (m^2)
t	time (s)
T	temperature (K); transmissivity (m^2/s)
u	vector of unknowns in the coefficient form of the PDE module of COMSOL
V	volume (m^3)
x, y, z	spatial coordinates (m)
z	vertical position vector (dimensionless)

Greek letters

α	mass transfer coefficient (m/Pa s)
α	conservative flux convection coefficient in the coefficient form of the PDE module of COMSOL
β	convection coefficient in the coefficient form of the PDE module of COMSOL
ϕ	porosity (m^3/m^3)
γ	conservative flux source term in the coefficient form of the PDE module of COMSOL
Γ	boundary
λ	mobility of a phase (m s/kg)
μ	dynamic viscosity of a phase (kg/m s)
ρ	density of a phase (kg/m^3)
Σ	surface of the BHK vault or the waste compartment

Sub- and super-scripts

c	capillary pressure; corrosion
e	effective
$entry$	entry pressure
ext	external value of a state variable or coordinate
$frac$	fracture
β, i, j	phases β, i and j
ini	initial
H2(g)	hydrogen gas
k	kth component
l, g	liquid and gaseous phases
p	pressure
r	relative; residual
reg	regolith
$rock$	rock
RT90	reference system
s	saturation
w	water
0	reference coordinates used by Vidstrand and Rhén (2011) and Joyce et al. (2019); initial

Acronyms/abbreviations

BDF	backward differentiation formula
BHA	vault for legacy waste
BHK	vault for metallic waste
ECPM	equivalent continuous porous medium
FF	far field
MUMPS	multifrontal massively parallel sparse direct solver
NF	near field
PDE	partial differential equation
SFL	repository for long lived low and intermediate level nuclear waste

Contents

1 Introduction

SKB plans to dispose of long-lived low and intermediate level nuclear waste in SFL. The waste comprises waste from the operation and decommissioning of the Swedish nuclear power plants, legacy waste from the early research in the Swedish nuclear programs, and smaller amounts of waste from hospitals, industry and research. The long-lived low and intermediate level waste from the nuclear power plants consists of neutron-irradiated components and control rods. The total quantity of long-lived waste planned for SFL is estimated to approximately 16 000 m^3, of which about one third originates from the nuclear power plants. The remainder comes from AB SVAFO and Studsvik Nuclear AB, who manage the legacy waste and the waste from hospitals, industry and research.

In the proposed concept (Elfwing et al. 2013), SFL is a deep geological repository with two storage vaults:

- one vault for the metallic waste from the nuclear power plants, and
- one vault for legacy waste from AB SVAFO and Studsvik Nuclear AB.

The vault for the metallic waste (BHK) is designed with a concrete barrier. The waste is segmented, after which the parts are deposited in steel tanks and stabilized with grout. The steel tanks are emplaced in the repository. This section of the repository is backfilled with concrete, which acts as a barrier against groundwater flow and contributes to a low diffusion rate and high sorption of many radionuclides. The concrete in the barrier will create an alkaline environment in the repository section, reducing the corrosion rate of the steel and thus limiting the release rate of radionuclides.

The vault for the legacy waste (BHA) from AB SVAFO and Studsvik Nuclear AB is designed with a bentonite barrier. The waste is deposited in containers designed for SFL and stabilized with grout. These containers are emplaced in the repository. The section is backfilled with bentonite. The bentonite acts as a barrier by limiting the groundwater flow, thereby making diffusion the dominant transport mechanism for radionuclides through the bentonite. Bentonite clay also has the ability to efficiently filter colloids (Elfwing et al. 2013).

Figure 1-1 shows a schematic representation of the repository design, with the BHA vault in the foreground and the BHK vault in the background.

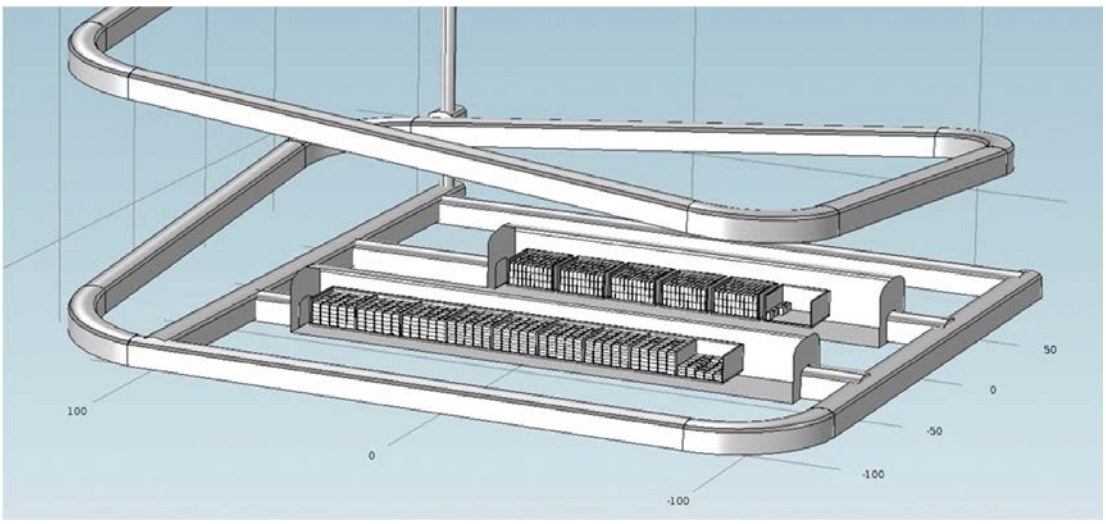

Figure 1-1. *SFL repository design with BHA vault (front) and BHK vault (back) (Abarca et al. 2019).*

With groundwater saturation of the repository, the anoxic corrosion of steel will produce hydrogen gas. This can have important implications on the repository system and the analysis of long term safety. Gas production may

- cause pressure build up potentially harmful to engineered barriers,
- affect the saturation level of the repository system,
- affect the groundwater flow in the vicinity of the repository.

A conceptual and numerical model of hydrogen gas release and migration at the BHK vault of the SFL repository was developed by Silva et al. (2019). The influence of gas production and migration in the near field (NF) was analyzed for two cases: (i) assuming the bedrock surrounding the repository as homogeneous and (ii) simulating a fracture zone within the homogeneous matrix. This study extends the work of Silva et al. (2019).

1.1 Objectives

The main objective of the present work is to extend the work of Silva et al. (2019) by introducing more realistic permeability fields and analyzing the influence of significantly larger hydrogen gas production. Specific objectives are:

- The comparison between the homogeneous rock concept (with and without a fracture zone) with the heterogeneous rock concept in the NF of the BHK vault, in terms of: (a) pressure build-up in the concrete barrier and (b) saturation level in BHK over time and the effect on the hydraulic behavior of the concrete barriers.
- Extending the NF two-phase flow models of Silva et al. (2019) to the far field (FF) until the bedrock-regolith interface above the BHK vault.
- The modeling of gas migration in the NF and FF until the bedrock-regolith interface above the BHK vault considering: (a) the heterogeneity of the rock, (b) the influence of gas release and migration on groundwater flow, (c) the effect of deformation zones on gas release and migration.
- Quantifying hydrogen gas fluxes at the regolith/bedrock interface resulting from gas release from the BHK vault.
- Analyze the influence of larger hydrogen gas production in both, NF and FF models.

1.2 Overview of calculation cases

The present modeling work is divided into the following tasks:

– Task 1. Comparison between homogeneous and heterogeneous rock in the NF model.

– Task 2. Influence of larger hydrogen gas production in the NF models.

– Task 3. Development of a heterogeneous model for gas migration from the vault to the regolith-bedrock interface.

– Task 4. Influence of larger hydrogen gas production in the FF models.

The effect of different factors on gas release from BHK and migration through the host rock in the NF and FF is studied through 21 simulation cases. The factors considered include host rock heterogeneity, regional groundwater flow and gas production rates. All the simulations assumed different water retention curves for the waste compartment and the backfill. Hereafter, “water retention” refers to the retention of water into a porous medium due to capillarity. Table 1-1 summarizes the main features of each simulation case. The motivation for each of these cases is explained below.

In the simulation Cases 1 to 15 the system is simplified by assuming hydrostatic conditions. These cases are intended to study different aspects of gas production and migration in the NF of the BHK vault.

Table 1-1. Summary of simulation cases to study hydrogen generation in the BHK vault and its impact at NF and FF scale.

Case No	Task	Domain extension	Embedded fracture	Rock	Boundary and initial conditions	Gas generation rate
1	1	NF	–	homogeneous	hydrostatic	$r_{H2(g)}$
2			fracture			
3			–	heterogeneous (Section A)		
4				heterogeneous (Section B)		
5			fracture	heterogeneous (Section A)		
6	2		–	homogeneous		$2r_{H2(g)}$
7			fracture			
8			–	heterogeneous (Section A)		
9				heterogeneous (Section B)		
10			fracture	heterogeneous (Section A)		
11			–	homogeneous		$10r_{H2(g)}$
12			fracture			
13			–	heterogeneous (Section A)		
14				heterogeneous (Section B)		
15			fracture	heterogeneous (Section A)		
16	3	FF	–	heterogeneous (Section A)	regional groundwater flow	$r_{H2(g)}$
17				heterogeneous (Section B)		
18	4			heterogeneous (Section A)		$2r_{H2(g)}$
19				heterogeneous (Section B)		
20				heterogeneous (Section A)		$10r_{H2(g)}$
21				heterogeneous (Section B)		

Nomenclature

NF and FF: near field and far field, respectively.

Fracture: including a fracture zone intersecting the BHK vault as studied in Silva et al. (2019).

$r_{H2(g)}$: Gas generation rate considered in Silva et al. (2019) (see Equation (2-4)).

Sections A and B are cross-sections of the host rock with zones of lower and higher permeability in the NF (see Section 2.1.2).

Hydrostatic: initial hydrostatic water pressure.

Regional groundwater flow: initial water pressures taken from the regional hydrology model (Joyce et al. 2019).

The group of simulation Cases 1 to 5 compares the flow behavior obtained with homogeneous and heterogeneous host rock models, which is the objective of Task 1. In these simulations, the hydrogen generation rate is that considered in Silva et al. (2019). Fracture or deformation zones may constitute a preferential pathway, affecting the gas release from the BHK vault and its migration through the rock (Vidstrand et al. 2010, Abarca et al. 2016). Thus, Case 2 considers homogeneous rock including a fracture zone. Cases 1 and 2 were already analyzed in Silva et al. (2019) and are included in this report for the comparison with other models (they were re-run in this work using finer spatial meshes). Rock heterogeneity in both, permeability and porosity, is addressed through Cases 3 and 4. In Case 3 the BHK vault is enclosed by a very low permeability zone (Section A, see Section 2.1.2). In Case 4 the vault is crossed by a high permeability zone well connected to the top of the system (Section B, see Section 2.1.2). Case 5 considers heterogeneous rock (Section A) including a fracture zone with a thickness of 1.0 m. The fracture zone statistics considered in Silva et al. (2019) shows that 95 % of the fracture permeability data is lower than 6.18×10^{-12} m^2. Therefore, in both, Case 2 and Case 5, the fracture zone permeability is set at this value, which is consistent with transmissivity measurements of minor deformation zones in Laxemar (Rhen et al. 2008).

The next group of simulation Cases, 6 to 15, aim to study the impact of larger hydrogen gas production rates on gas migration in the NF, which is the aim of Task 2. Sequences of Cases 6 to 10, and Cases 11 to 15, are equivalent to that of Cases 1 to 5, but considering a gas generation rate 2 and 10 times higher, respectively.

The simulations Cases 16 to 21 address the gas release from BHK and its migration in the FF. In these cases, the host rock is assumed to have heterogeneous permeability and porosity fields. Furthermore, the initial and boundary water pressure distribution are taken from the regional groundwater flow model (Joyce et al. 2019). That is, they are the pressure distributions corresponding to Section A and Section B. Cases 16 and 17 correspond to Sections A and B, respectively (see Section 2.6.2). The results of these simulation cases are the base of Task 3. Finally, the effect of larger gas production rates (Task 4) is analyzed comparing Cases 16 and 17 with Cases 18 and 19 (double corrosion rate), and Cases 20 and 21 (gas production rate ten times higher than in Silva et al. 2019).

1.3 Outline of the report

Chapter 2 describes the model methodology. Five models are used to study gas production and migration in the NF of the BHK vault: a homogeneous rock model, a model of homogeneous rock including a fracture zone, 2 heterogeneous rock models (Sections A and B), and a model of heterogeneous rock (Section A) including a fracture zone. Furthermore, the heterogeneous rock models are extended to the FF. The models enable evaluation of the impact of gas production and migration at a larger spatial scale and estimate the gas fluxes at the bedrock-regolith interface. The geometry, boundary conditions, hydraulic and transport properties considered in each of these models are described. The hydrogen generation rates assumed in these models are also explained.

Chapter 3 shows the numerical implementation of the NF and FF models into Comsol Multiphysics 5.3. The spatial discretization, time stepping, and the solvers used in each model are described.

Chapter 4 analyses the results computed with the NF models. First, the simulation Cases 1-5 described in Section 1.2 (Table 1-1) are compared to determine the difference between assuming homogeneous and heterogeneous host rock. Heterogeneity is represented by a case of a homogeneous rock that includes a fracture zone, and two cross-sections of different hydraulic connectivity. The comparison is made in terms of the evolution of the gas saturation distribution, gas streamlines, the average pressure and overpressure in the BHK vault, and the inflow and outflow rates of gas and water to/from the vault. Then, the results of the simulations Cases 5-15 aimed to evaluate the effect of larger gas production are presented. The resultant gas saturation distributions, average gas pressure and overpressures in the BHK vault are compared with those obtained in the Cases 1-5.

Chapter 5 presents the results obtained with the FF models. First, Cases 16 and 17 study the gas release from the BHK vault and its migration in the FF through a heterogeneous medium. Heterogeneity is assumed in both the rock permeability and porosity. Two cross-sections of different hydraulic connectivity are compared considering the same gas generation rates used by Silva et al. (2019). The evolution of gas fluxes at the regolith-rock interface is also calculated. Next, four additional cases are simulated to evaluate the effect of increasing the gas production rate by 2 (Cases 18 and 19) and 10 times (Cases 20 and 21).

Chapter 6 summarizes the main results and conclusions of the work.

2 Model description

This section presents the modeling methodology. The same governing equations of immiscible two-phase flow in porous media and constitutive relationships presented in Silva et al. (2019) are used in this work. The novelty is the application of these equations in some models to study the evolution of gas in the far field and its impact on flow in the geosphere.

The geometry and parameterization of the system is also explained. This includes the procedure to select two cross-sections of the heterogeneous rock around the SFL repository. Also, it includes the hydrogen generation rates and the hydraulic and transport properties of the BHK vault and the host rock in the SFL repository.

2.1 General framework

2.1.1 The SFL repository

A schematic representation of the SFL layout is shown in Figure 1-1 and Figure 2-1. Figure 2-2 shows a schematic cross-section of the BHA and BHK vaults, the later in focus in this work. In the BHK vault the waste is segmented, after which the parts are deposited in steel tanks and stabilized with grout. The steel tanks are emplaced in concrete compartments which are also grouted. Upon closure, the entire vault will be backfilled with concrete.

The modeling set-up in this work considers 2D cross-sections of the BHK vault at the reference position and orientation of 500 m depth described by Abarca et al. (2016). The BHK system components are represented by a waste domain and a backfill domain.

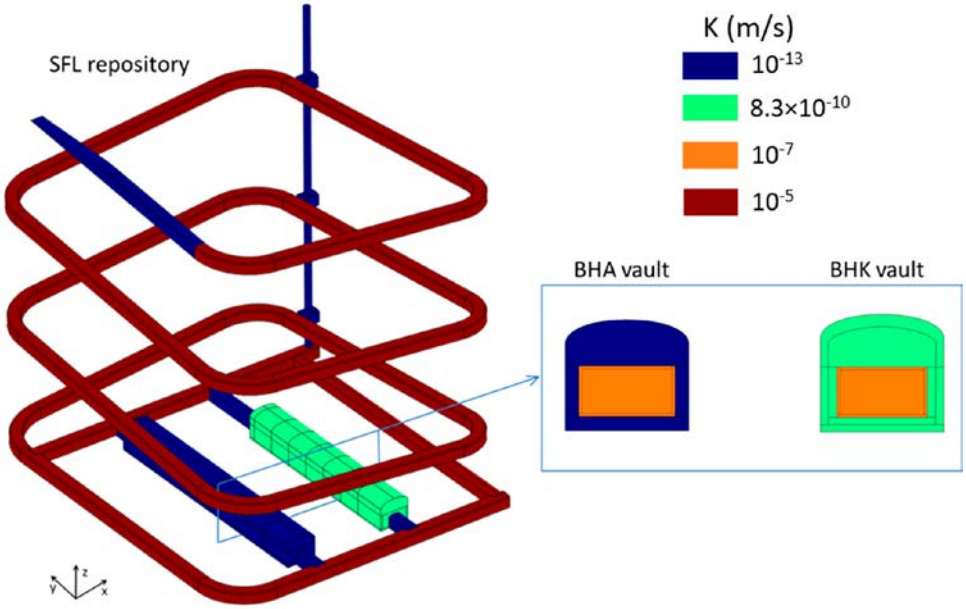

Figure 2-1. *Assignment of hydraulic conductivity to the materials in the SFL model domains (Abarca et al. 2016). The BHK vault is highlighted by the green color associated with the backfill material.*

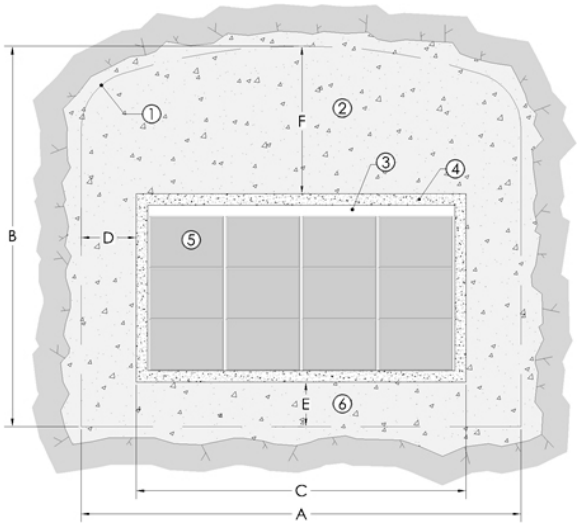

Figure 2-2. *Schematic cross-sectional layout of the BHK vault for metallic waste (from Elfwing et al. 2013). Legend: 1.) Theoretical tunnel contour. 2) Concrete backfill. 3) Grout. 4) Concrete structure. (0.5 m). 5) Steel tanks. 6) Concrete. Approximated dimensions: A = 20.6 m, B = 19.6 m, C = 15 m, D = 2.8 m, E = 2.4 m, F = 8.8 m.*

2.1.2 Selection of cross-sections

The host rock heterogeneity is considered in the NF and FF models through two different cross-sections. The porosity and permeability tensor fields were obtained from the regional geohydrology model (Joyce et al. 2019). The criteria to select these two cross-sections are explained below.

Figure 2-3 shows the distribution of the rock permeability tensor (**k**) at the longitudinal section crossing the center of the BHK vault (x = 8 043.7 m). In general, the three components of the permeability tensor display similar distributions. Figure 2-3 at right shows the vertical component of the permeability (k_{zz}) where black lines represent zx 2D sections crossing the BHK vault at four different y coordinates: Y 7154, Y 7187, Y 7224 and Y 7264. The vertical component of the permeability at these xz cross-sections are presented in Figure 2-4. Section Y 7154 presents a zone of high permeability (10^{-14} m^2) crossing the BHK vault (enclosed by the black ellipsis in Figure 2-4). This zone is connected to very high permeability ($\geq 10^{-13}$ m^2) zones located at lower depths. Section Y 7187 shows a zone of low permeability (10^{-16} m^2) enclosing the vault, which is in the middle of a zone of high permeability that extends to the bottom of the system. Section Y 7224 also displays a zone of high permeability crossing the BHK vault. However, this highly permeable area is disconnected from the rest of the rock above the vault. By contrast, in the section Y 7264 the vault is surrounded by a very low permeability (10^{-17} m^2) zone (enclosed by the black ellipsis in Figure 2-4). In addition, the permeability distribution in the upper part of this cross-section is noticeably more heterogeneous than in the other three sections.

Because sections Y 7264 and Y 7154 represents two cases of opposite hydraulic behavior, they were selected to develop the NF and FF models considering the rock heterogeneity. Hereafter, these sections are named “Section A” and “Section B”, respectively. Also, “very high”, “high”, “low” and “very low” permeability zones refer to zones with permeabilities in the order of 10^{-13}, 10^{-14}, 10^{-16} and 10^{-17} m^2, respectively. The vertical permeability distributions at the selected Sections A and B are shown in Figure 2-5 and Figure 2-6.

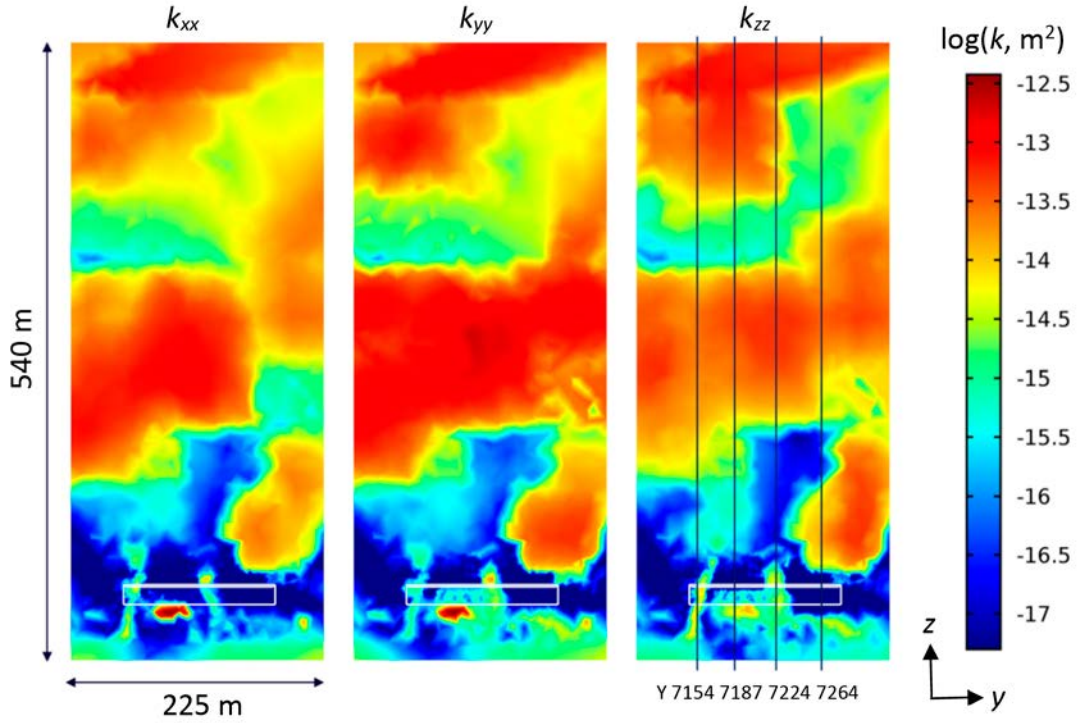

Figure 2-3. *Rock permeability distribution at x = 8 043.7 m (center of the BHK vault). The location of the BHK vault is denoted by white lines. Black lines in the vertical permeability field indicates the y coordinates of the cross-sections plotted in Figure 2-4.*

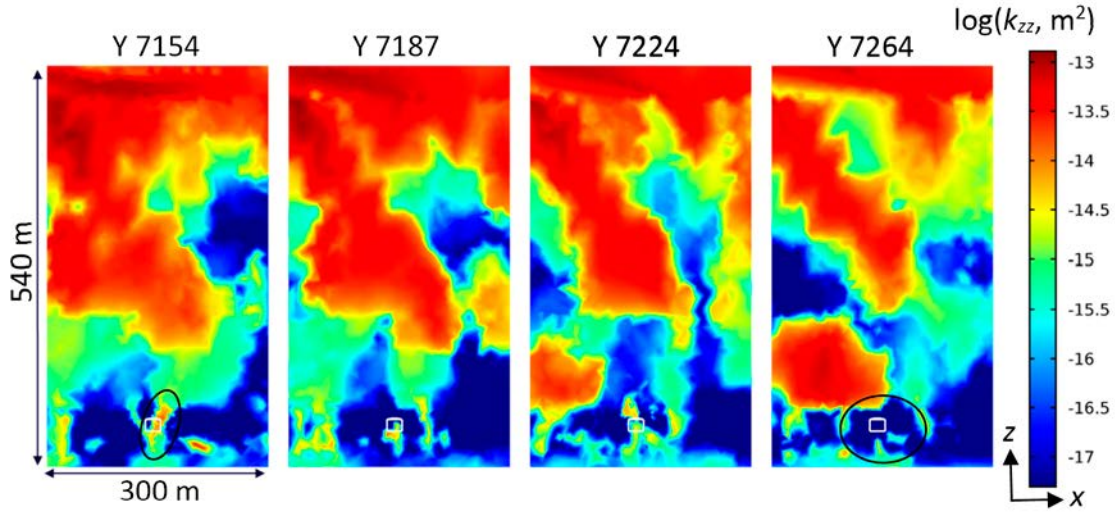

Figure 2-4. *Vertical rock permeability distribution at different cross-sections along the vault. The location of BHK vault is denoted by white lines. Black ellipsis show a high permeability zone crossing the BHK vault at y= 7 154 m, and a very low permeability zone enclosing it at y = 7 264 m.*

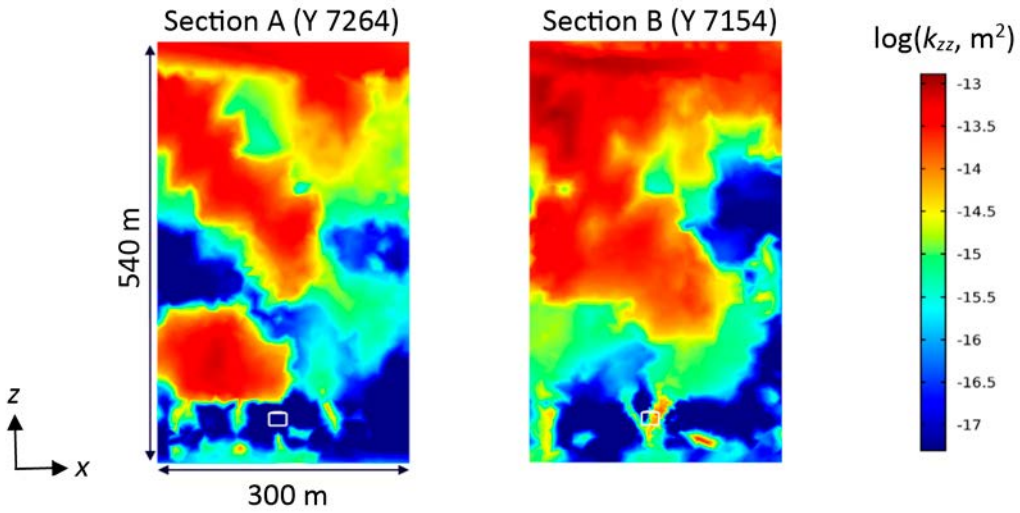

Figure 2-5. *Selected cross-sections to model gas migration from the BHK vault to the far field. Section A has a very low permeability zone enclosing the BHK vault at y = 7264 m. Section B presents a high permeability zone crossing the BHK vault at y= 7154 m.*

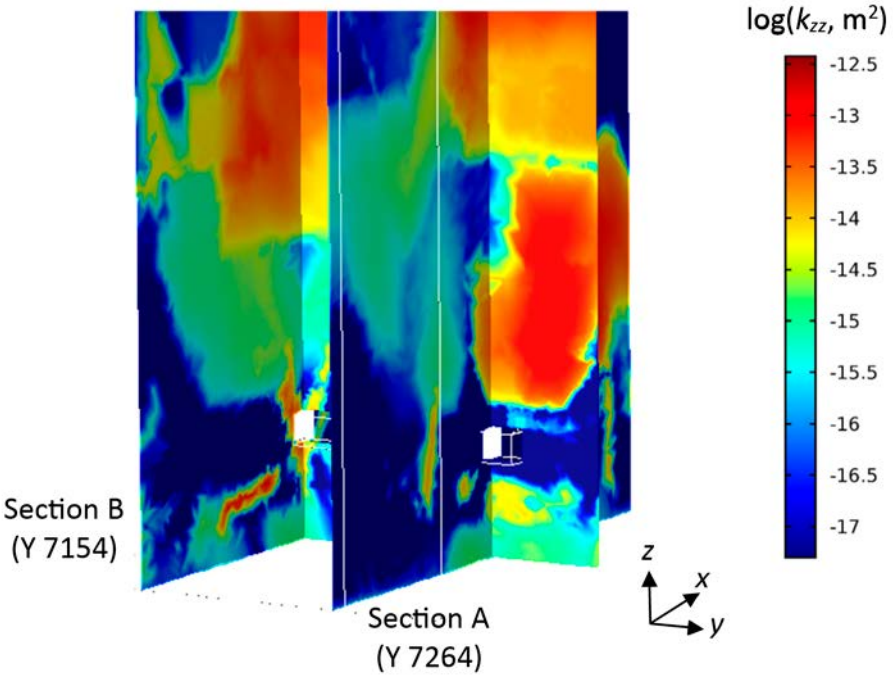

Figure 2-6. *3D view of vertical rock permeability distribution showing the selected Sections A (y = 7264 m) and B (y = 7154 m). The location of BHK vault is denoted by white lines.*

2.1.3 Model equations

The same governing equations and constitutive relationships described in Silva et al. (2019) are considered in this work. In summary, the mathematical approach is based on solving the flow equation of the gas phase and the sum of the liquid and gas flow equations

$$\phi\rho_g \frac{\partial S_g}{\partial t} + \nabla\cdot\left(\rho_g \mathbf{q}_g\right) + \frac{\partial\left(\phi\rho_g\right)}{\partial t} S_g = \sum_{k=1}^{N} Q_g^k \qquad \text{(Eq 2-1)}$$

$$\phi\left(\rho_g - \rho_l\right)\frac{\partial S_g}{\partial t} + \nabla\cdot\left(\rho_l \mathbf{q}_l + \rho_g \mathbf{q}_g\right) + \frac{\partial\left(\phi\left(\rho_g - \rho_l\right)\right)}{\partial t} S_g = -\frac{\partial\left(\phi\rho_l\right)}{\partial t} + \sum_{k=1}^{N}\left(Q_l^k + Q_g^k\right) \qquad \text{(Eq 2-2)}$$

where $\mathbf{q}_i$ (m/s) is the specific discharge of phase i ($i = l, g$), ϕ (m^3/m^3) the soil porosity, S_g is the gas phase saturation, ρ_i (kg/m^3) the density of phase i, Q_i^k (kg/m^3 s) a mass sink/source term of a component k in the phase i (sinks are assigned with negative values of Q_i^k while the sources are positive). $\mathbf{q}_i$ is calculated according to the generalized Darcy's law (Bear and Bachmat 1991)

$$\mathbf{q}_i = -\mathbf{k}\lambda_i\left(\nabla P_i + \rho_i g\mathbf{z}\right) \qquad \text{(Eq 2-3a)}$$

$$\lambda_i = \frac{k_{ri}}{\mu_i} \qquad \text{(Eq 2-3b)}$$

In Equation (2-3), $\mathbf{k}$ (m^2) is the permeability tensor of the soil, $g\mathbf{z}$ (m/s^2) the gravity vector, λ_i (m s/kg) the mobility, k_{ri} (dimensionless) the relative permeability, μ_i (kg/m s) the dynamic viscosity, and P_i (Pa) the pressure of phase i.

Liquid pressure, P_l (Pa) and gas saturation (S_g) are chosen as the state variables of the governing Equations (2-1) and (2-2). This formulation is called pressure-saturation (P-S) approach.

2.1.4 Equations of state and constitutive relationships

The system is assumed isothermal at 14.7 °C, which is the temperature at the depth of the BHK (~ 500 m) vault (Joyce et al. 2019). Liquid density and viscosity are assumed constant at this temperature: ρ_l is set at 1 003 kg/m^3 (Abarca et al. 2019) assuming a salinity of 0.12 % and μ_l is set at 2×10^{-3} Pa-s (Joyce et al. 2019). Gas density and viscosity are calculated according to the Peng-Robinson equation of state (Peng and Robison 1976) and Chung correlation (Chung et al. 1988), respectively. The water retention curve and relative permeabilities are described by van Genuchten functions (van Genuchten 1980) with representative parameters for each material (SKB 2014).

2.1.5 Gas production rates

In the BHK vault, hydrogen gas is produced within the waste due to the steel corrosion. Thus, the hydrogen generation rates are calculated from the steel corrosion rates and the stoichiometry of associated chemical reactions as explained in Silva et al. (2019). Hydrogen gas production is represented in the governing equations (Silva et al. 2019) by a gas source term applied over the waste sub-domain (see Figure 2-7). The waste in the BHK is composed mainly by carbon and stainless steel. Thus, the hydrogen generation rate ($r_{H2(g)}$) considered in some simulations (Cases 1 to 5, 16 and 17) is obtained from adding the rates associated with the corrosion of carbon steel and stainless steel (Silva et al. 2019).

$$r_{H_2(g)} = \begin{cases} 4.95\times10^{-12}\ \text{kg/m}^3\text{s} & t \le t_{c,ss} \\ 2.67\times10^{-12}\ \text{kg/m}^3\text{s} & t_{c,ss} < t \le t_{c,cs} \\ 0 & t > t_{c,cs} \end{cases} \qquad \text{(Eq 2-4)}$$

To study the possible effects of higher gas generation, two more rates are analyzed. The rate estimated by Silva et al. (2019) is increased by 2 (Cases 6 to 10, 18 and 19) and by 10 (Cases 11 to 15, 20 and 21). As the same initial mass of steel is assumed in all simulation cases, under these higher corrosion rates steel is consumed faster. Also, because the corrosion rates are constant, the mass of steel decreases linearly with time. Therefore, the corrosion times of stainless steel ($t_{c,ss}$ = 74 920 years) and carbon steel ($t_{c,cs}$ = 615 313 years) are divided accordingly by 2 and 10, respectively.

As in Silva et al. (2019), water consumption is disregarded in all simulation cases.

2.2 NF homogeneous host rock model

2.2.1 Geometry

In the simplest representation of the system the rock surrounding the BHK vault is assumed to be homogeneous. Figure 2-7 shows the geometry and boundary conditions assumed for the case of hydrostatic conditions (Cases 1, 6 and 11; see Section 1.2 and Table 1-1). The domain dimensions are the same considered in Silva et al. (2019). They found that a rock domain of 120 m × 120 m is adequate, such that boundary conditions do not affect the flow and transport in the NF of the vault.

The lower left corner of the BHK vault in the model domain is set at x = 8 033.4 m and z = -500.6 m, coinciding with the local coordinate system of Abarca et al. (2016). Comsol local coordinates are calculated as $x = x_{RT90} - x_0$, $y = y_{RT90} - y_0$, where x_{RT90} and y_{RT90} are the coordinates of the reference system RT90 and x_0 = 1 539 000 and y_0 = 6 360 000 (see Vidstrand and Rhén 2011, Table 6-8, Joyce et al. 2019). The plane intersecting the BHK vault is assumed to be located at an arbitrary y position.

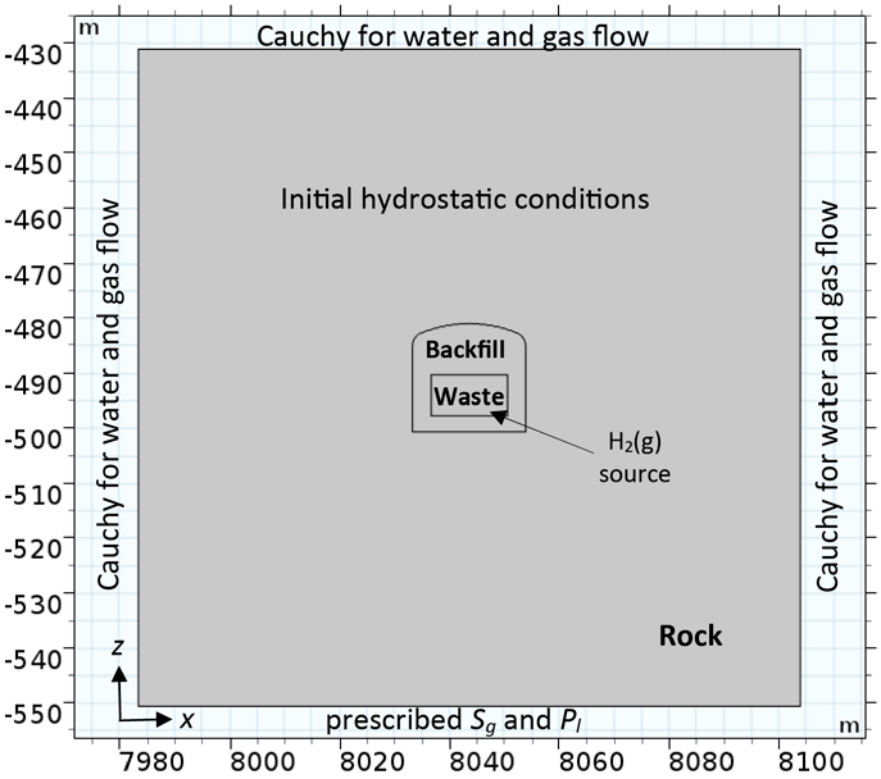

Figure 2-7. *Geometry and boundary conditions implemented in the COMSOL model of immiscible two-phase flow in the NF of the BHK vault.*

2.2.2 Initial and boundary conditions

In the NF models (see Figure 2-7), hydrostatic conditions are assumed initially and the water pressure field, $P_{l,ini}$ (Pa), within the system is set to

$$P_{l,ini} = 101325 + \rho_l g z \qquad \text{(Eq 2-5)}$$

where ρ_l (kg/m^3) is the liquid density, g = 9.81 m/s^2 the gravity and z (m) the vertical coordinate. The initial saturation of the gas phase ($S_{g,ini}$) is set at zero throughout the domain.

Mixed-type (Cauchy) boundary conditions are used to address the arrival of gas to a given boundary and its impact on water flow at that boundary (see Figure 2-7). In this work, Cauchy boundary conditions are applied at the top and lateral boundaries. This is because, under the hydraulic conditions considered, the gas generated in the BHK vault flows upwards and higher corrosion rates can cause a significant spreading of the gas bubble. As explained by Silva et al. (2019), the Cauchy boundary conditions at a given boundary (Γ) are expressed as

$$\sum_{k=1}^{N} Q_g^k = Q_g = -\rho_g \left\{ \alpha_g^s \left(S_{g,ext} - S_g \right) - \alpha_g^p \left(P_{l,ext} - P_l \right) \right\} \qquad (x,z) \in \Gamma \qquad \text{(Eq 2-6a)}$$

$$\sum_{k=1}^{N} Q_l^k = Q_l = \rho_l \alpha_l^p \left(P_{l,ext} - P_l \right) \qquad (x,z) \in \Gamma \qquad \text{(Eq 2-6b)}$$

Above, $S_{g,ext}$ and $P_{l,ext}$ are external values of the state variables, which in this work are assumed to be equal to the initial values evaluated at the boundary. α_g^s (m/Pa s) and α_g^p (m/Pa s) are mass transfer coefficients for gas flow due to saturation and pressure variations, and α_l^p is a mass transfer coefficient for liquid flow due to pressure variations. These boundary conditions are implemented in Comsol as *weak contribution* to the flow equations. The Cauchy boundary condition specifies that the flow (Q_β, $\beta = l, g$) through that boundary is proportional to the pressure difference between the calculated pressure (P_β) and a prescribed external pressure ($P_{\beta,ext}$). The coefficients of proportionality α_β^p, $\beta = l, g$ which are phase-dependent, can be extracted from the following form of Darcy flow for each phase

$$\begin{aligned} Q_\beta = \rho_\beta k \lambda_\beta \nabla P_\beta &= \rho_\beta \frac{k\lambda_\beta}{\left(y_{ext} - y \right)} \left(P_{\beta,ext} - P_\beta \right) \\ &= \rho_\beta \alpha_\beta^p \left(P_{\beta,ext} - P_\beta \right) \qquad \beta = l, g \end{aligned} \qquad \text{(Eq 2-7a)}$$

$$\alpha_\beta^p = \frac{k\lambda_\beta}{\left(r_{ext} - r \right)} \qquad \text{(Eq 2-7b)}$$

In the above equations, k (m^2) is the permeability of the rock, r (m) is the position of the boundary in the direction perpendicular to that boundary, and r_{ext} (m) is the respective coordinate at the external position. In terms of the state variables (S_g and P_l) the gas flux reads

$$\begin{aligned} Q_g = \rho_g k \lambda_g \nabla P_g &= \rho_g k \lambda_g \left(\nabla P_c + \nabla P_l \right) = \rho_g k \lambda_g \left(-\frac{\partial P_c}{\partial S_l} \nabla S_g + \nabla P_l \right) \\ &= -\rho_g \frac{k\lambda_g}{\left(r_{ext} - r \right)} \frac{\partial P_c}{\partial S_l} \left(S_{g,ext} - S_g \right) + \rho_g \frac{k\lambda_g}{\left(r_{ext} - r \right)} \left(P_{l,ext} - P_l \right) \end{aligned} \qquad \text{(Eq 2-8a)}$$

$$Q_g = -\rho_g \left\{ \alpha_g^s \left(S_{g,ext} - S_g \right) - \alpha_g^p \left(P_{l,ext} - P_l \right) \right\} \qquad \text{(Eq 2-8b)}$$

$$\alpha_g^s = \alpha_g^p \frac{\partial P_c}{\partial S_l} \qquad \text{(Eq 2-8c)}$$

The external variables $S_{g,ext}$ and $P_{l,ext}$ are assumed to be equal to the initial values evaluated at the boundary ($S_{g,ext} = 0$ and $P_{l,ext}$ given by Equation 2-5). The distance from the external position to the boundary where the Cauchy condition is imposed, $\Delta r_{ext} = |r_{ext} - r|$, controls the water and gas fluxes. As this distance decreases, the Cauchy condition approaches a Dirichlet condition (prescribed S_g and P_l). Δr_{ext} was tuned such that the gas saturation gradient at the boundary is smooth (no gas accumulation or depletion).

At the bottom of the system, the liquid pressure and the gas saturation are prescribed to their initial values.

2.2.3 Hydraulic and transport properties

The water retention curves of the different materials are assumed to follow the van Genuchten model (van Genuchten 1980)

$$P_c = P_0\left(S_e^{-1/m} - 1\right)^{1/n}$$
$$S_e = \frac{S_l - S_{lr}}{1 - S_{lr} - S_{gr}}, \quad m = 1 - \frac{1}{n} \qquad \text{(Eq 2-9)}$$

Above, P_c is the capillary pressure defined as the difference between the gas and liquid pressures ($P_c = P_g - P_l$), S_e is the effective saturation of the liquid phase, P_0 (Pa) a scaling pressure related to the gas entry pressure P_{entry} (Pa), S_{lr} and S_{gr} are the residual saturation of the liquid and gas phase, respectively, and n is a parameter related to the pore size distribution. The relative permeabilities of the liquid and gas phases are also calculated per the van Genuchten model (van Genuchten 1980)

$$k_{rl} = S_e^{0.5}\left(1 - \left(1 - S_e^{1/m}\right)^m\right)^2 \qquad \text{(Eq 2-10a)}$$

$$k_{rg} = \left(1 - S_e^2\right)\left(1 - S_e\right)^2 \qquad \text{(Eq 2-10b)}$$

The gas entry pressure is estimated as $P_{entry} = P_0(1 - 0.9S_{entry}{}^{-0.5})^{1/m}/[1 - (1 - 0.9S_{entry}{}^{-0.5})^{1/m}]$ (Silva et al. 2019) where S_{entry} is the effective saturation at which $k_{rl} = 0.9$.

Porosity and permeability of the rock were obtained from the regional geohydrology model of SFL (Joyce et al. 2019). These properties were calculated in a box of 500 m × 500 m × 180 m ($7\,750 \le x \le 8\,250$; $7\,000 \le y \le 7\,500$; $-580 \le z \le -400$) enclosing the 2D domain used in the present simulations. Histograms of the obtained porosity and the components of the permeability tensor are shown in Figure 2-8. They provide an idea of the heterogeneity of the regional hydrogeological system of SFL (Joyce et al. 2019) in the NF of the BHK vault.

The minimum, maximum and average values of these hydraulic properties are shown in Table 2-1. In the current model, the permeability is assumed to be an isotropic tensor. The permeability values shown in Table 2-1 were calculated as the arithmetic mean of the components of the rock permeability tensor ($k = (k_{xx} + k_{yy} + k_{zz})/3$, see Figure 2-8). Also, the rock porosity and permeability were set at $\phi = 4.37 \times 10^{-4}$ and $k = 6.67 \times 10^{-15}$ m^2, respectively. These values are slightly lower than the average values presented in Table 2-1, but may represent better the hydraulic properties of the rock in the NF of the BHK vault. The van Genuchten parameters of rock were assumed to be equal to the arithmetic average between the values reported by Finsterle and Pruess (1995) and Jarsjö et al. (2001).

Table 2-1. Minimum, maximum and average values of rock porosity and permeability derived from the regional geohydrology model (Joyce et al. 2019).

Parameter	Minimum	Maximum	Average
Porosity, ϕ	3.20×10^{-5}	1.59×10^{-2}	6.24×10^{-4}
Permeability, k (m^2)	5.00×10^{-18}	2.65×10^{-12}	1.33×10^{-14}

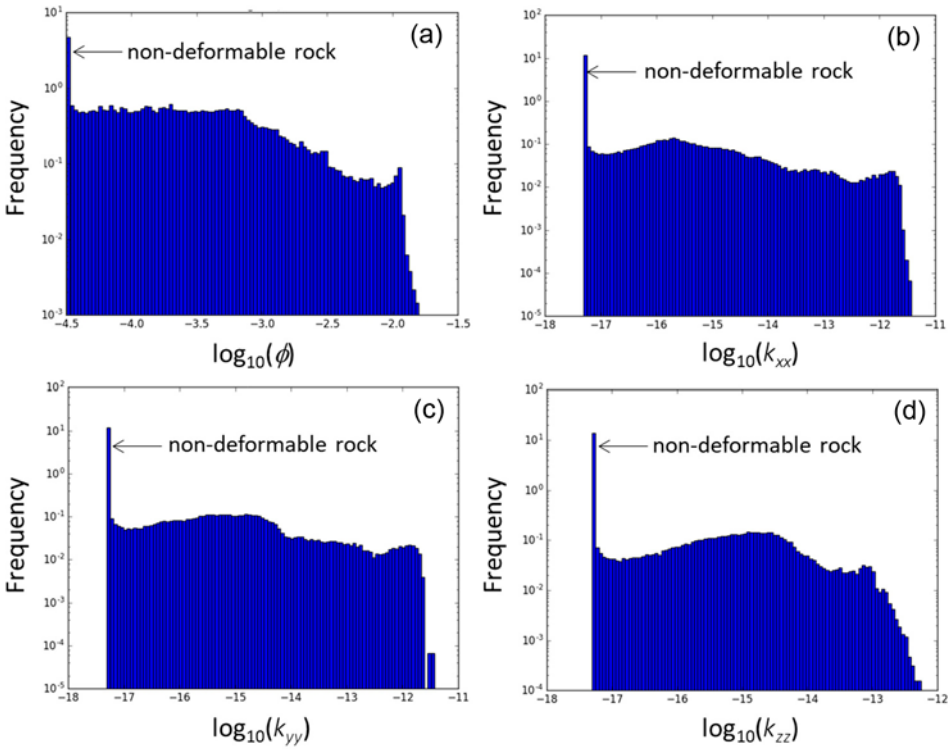

Figure 2-8. *Histograms of rock (a) porosity and permeability in the (b) x lateral, (c) y lateral and (d) z vertical directions obtained with ConnectFlow (Amec 2014) and the regional geohydrology model of SFL (Joyce et al. 2019).*

The porosity and permeability of the waste and the backfill were taken from SKB (2014). The van Genuchten parameters of these materials were taken from Xu et al. (2008) and Baroghel-Bouny et al. (1999), respectively.

Table 2-2 summarizes the hydraulic parameters corresponding to each material. The water retention and permeability functions of the different materials are displayed in Figure 2-9.

A sensitivity analysis regarding the parameters of the water retention curve of the different materials was not considered in this work. Silva et al. (2019) compared cases where the water retention properties of the backfill and the waste are the same and different. They found that when different water retention curves are applied to the waste and backfill materials, gas tends to accumulate in the top backfill and is released faster. Also, they showed that a contrast of water retention properties can lead to higher local pressures, especially in the top backfill. A sensitivity analysis to the water retention properties of the host rock could be a matter of future research.

Table 2-2. Hydraulic parameters assumed for the different materials of the BHK vault and the surrounding rock.

Parameter	Waste	Backfill	Rock
Porosity, ϕ	0.3	0.11	4.37×10^{-4}
Permeability, k (m^2)	2.0×10^{-14}	1.7×10^{-16}	6.67×10^{-15}
Residual liquid saturation, S_{lr}	0.0	0.0	0.0
Residual gas saturation, S_{gr}	0.0	0.0	0.0
n	2.00	1.78	2.32
Scaling pressure, P_0 (MPa)	0.050	1.677	0.871

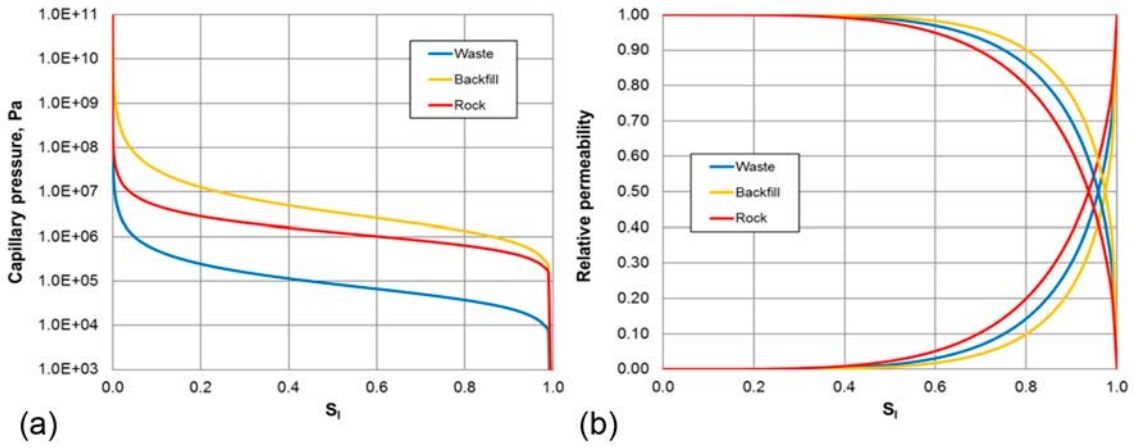

Figure 2-9. *(a) Water retention and (b) relative permeability functions of the different materials in BHK.*

2.3 NF model of homogeneous rock and a fracture zone

2.3.1 Geometry

A fracture zone has been added to the model in an alternate representation of the granitic host rock. The fracture zone is conceptualized as an equivalent continuous porous medium (ECPM), with its respective permeability, porosity and water retention curve. As in Silva et al. (2019), an arbitrary fracture zone of 1 m thickness was included, such that it intersects the BHK vault (see Figure 2-10).

2.3.2 Hydraulic properties

The water retention curves and permeability functions of the host rock and the BHK materials are assumed to be equal to the functions considered in the homogeneous rock model (see Section 2.2.3).

Probability functions derived by Silva et al. (2019) showed that 95 % of fracture permeability data of Rhén et al. (2008) is lower than 6.18×10^{-12} m^2. Also, Silva et al. (2019) showed that, for this permeability value, the fracture zone has a significant impact on the gas flow out from the BHK vault. Accordingly, in the present work the permeability of the fracture zone is set to 6.18×10^{-12} m^2.

The fracture zone porosity was assumed constant and equal to 0.01. This value was estimated using the correlation given in Rhén et al. (2008) for kinematic porosity of deformation zones and the coefficients suggested by Hjerne et al. (2010).

There is a high uncertainty on the hydraulic characterization of fracture zones in Laxemar under two-phase flow conditions. Because of that, the van Genuchten parameter n of the fracture zone is set arbitrarily to 2, while the scaling pressure P_0 is set to 10^5 Pa, which is lower than the scaling pressure assumed for rock and backfill. The rule is that, the lower P_0, the easier for the gas to enter a fracture zone. Also, the water retention curve of the fracture zone is estimated by scaling the water retention curve of the rock by the Leverett factor, $(T_{rock}/T_{frac})^{1/3}$ (Jarsjö et al. 2001). T_{rock} (m^2/s) and T_{frac} (m^2/s) are the transmissivities of the rock and fracture zone, respectively. From the statistics of fracture transmissivity presented in Rhén et al. (2008), the scaling factor ranges between 0.065 and 0.5. This is consistent with the difference displayed in Figure 2-11 between the red and green lines. Thus, the above parameters of the water retention curve can be considered representative of the fracture zone. Note that increasing P_0 reduces the capillary contrast between the fracture and the rock, approaching the system to the homogeneous host rock case. In the limit, when the water retention curves are the same, fluid flow through the fracture is only driven by the fracture zone permeability. As shown in Figure 2-11, the water retention curve of the fracture zone lies in between the water retention curves of the waste and the rock. Because of the above assumptions, the relative permeability of the fracture zone coincides with the relative permeability of the waste (see Equation (2-10) and Figure (2-9b)).

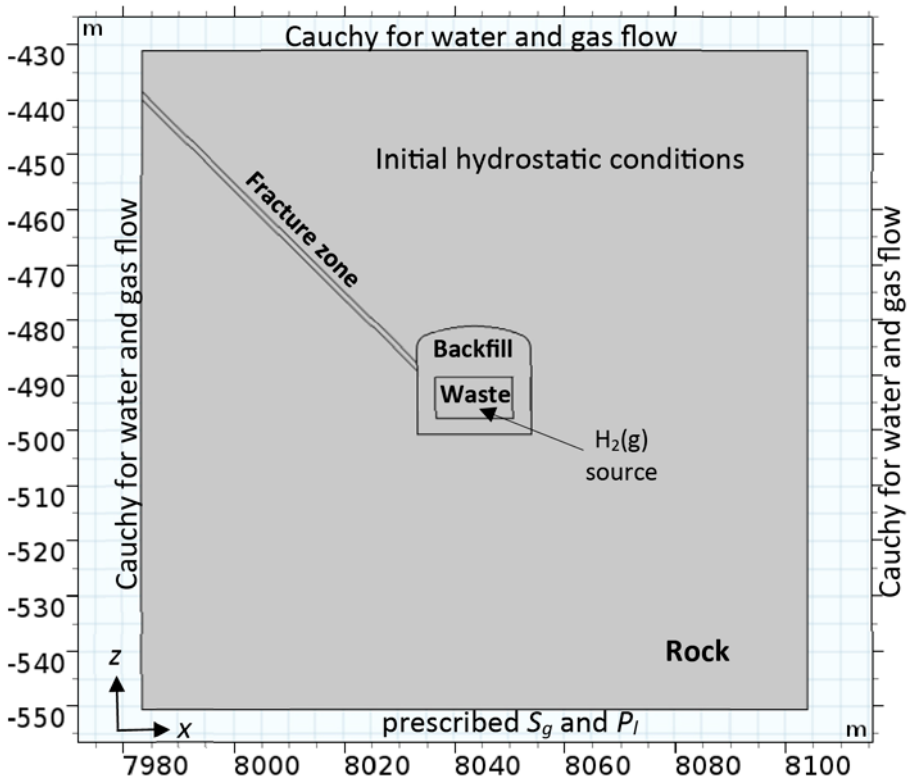

Figure 2-10. *Geometry and boundary conditions implemented in the COMSOL model of immiscible two-phase flow in the NF of the BHK vault for the case including a fracture zone.*

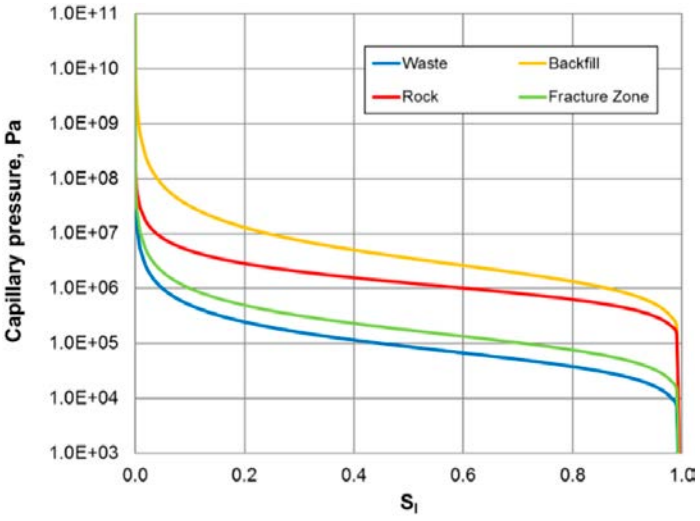

Figure 2-11. *Water retention curves considered to simulate immiscible two-phase flow in the BHK vault including a fracture zone.*

2.4 NF heterogeneous host rock model

Two models of gas flow in the NF of the BHK vault with heterogeneous host rock were also studied (Cases 3, 4, 8, 9, 13 and 14; see Section 1.2 and Table 1-1). The porosity field and permeability tensor obtained from the regional hydrological model (Joyce et al. 2019) are used in these models. They correspond to the selected Sections A and B (see Section 2.1.2), which are shown in Figure 2-12. The plane intersecting the BHK vault is at the position y = 7 264 m and y = 7 154 m, respectively.

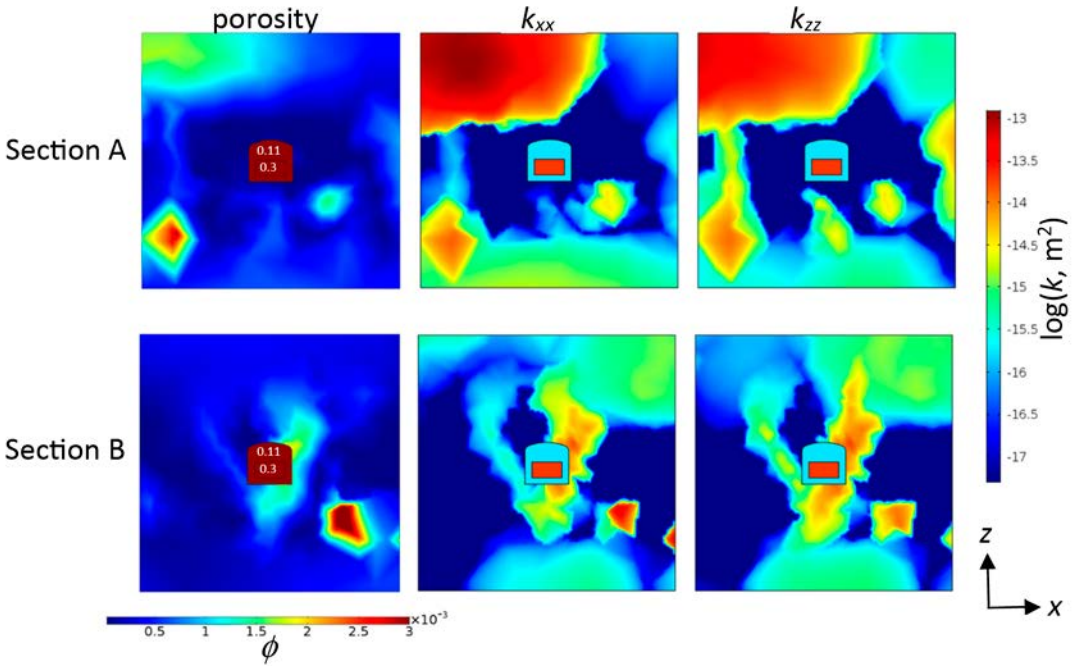

Figure 2-12. *Porosity and permeability distributions for cross-sections A and B used in the NF model with heterogeneous host rock.*

The water retention curves and permeability functions of the heterogeneous host rock and the BHK vault materials are assumed to be equal to the functions considered in the homogeneous rock model (see Section 2.2.3). Including the heterogeneity on the water retention properties of the host rock or performing a sensitivity analysis to these parameters could be a matter of future research.

2.5 NF model of heterogeneous rock and a fracture zone

A fracture zone has been added to the NF model with heterogeneous rock of low permeability around the BHK vault (Section A, y = 7 264 m). In this alternate heterogeneous model (see Figure 2-13), the fracture zone has the same geometric configuration and properties considered in the NF model with homogeneous rock and fracture zone (Section 2.3).

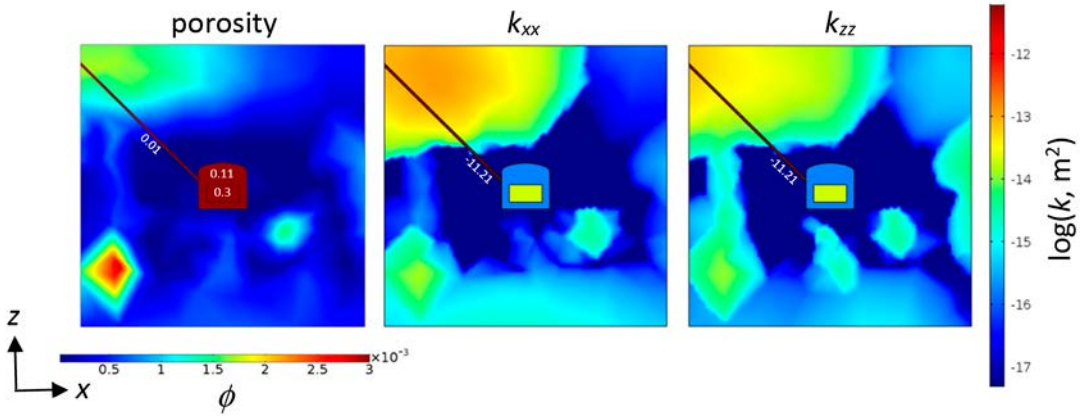

Figure 2-13. *Porosity and permeability distributions for cross-section A used in the NF model with heterogeneous host rock and a fracture zone.*

The water retention curves and permeability functions of the heterogeneous host rock and BHK vault materials are assumed to be equal to the functions considered in the homogeneous rock model (see Section 2.2.3). Moreover, the same water retention curve and permeability function, as well as porosity and permeability, of the fracture zone given in Section 2.3.2 are considered in this model.

2.6 FF heterogeneous host rock model

2.6.1 Geometry

The set-up of the FF model considers the cross-sections A and B (see Section 2.1.2). As in the NF models, the BHK vault components are represented by the waste and backfill domains. The surrounding rock is assumed to be heterogeneous in both, permeability and porosity.

Figure 2-14 shows the geometry and boundary conditions assumed in this model (Cases 16–21; see Section 1.2 and Table 1-1). The rock domain is a rectangle of 535 m deep × 403.6 m width. The location of the BHA vault and the ramp are indicated in the figure, but have been disregarded in the model. The present model assumes a uniform regolith thickness. The top boundary of the domain coincides with the interface between the regolith and the bedrock. This is assumed to be located 15.6 m below the ground surface. This simplification is in accordance with the variation in the regolith thickness, which ranges between 4 and 23 m (Lindström et al. 2000). Preliminary test simulations showed that the domain geometry and dimensions are such that boundary conditions do not affect the flow and transport, neither in the NF nor in the FF of the BHK vault.

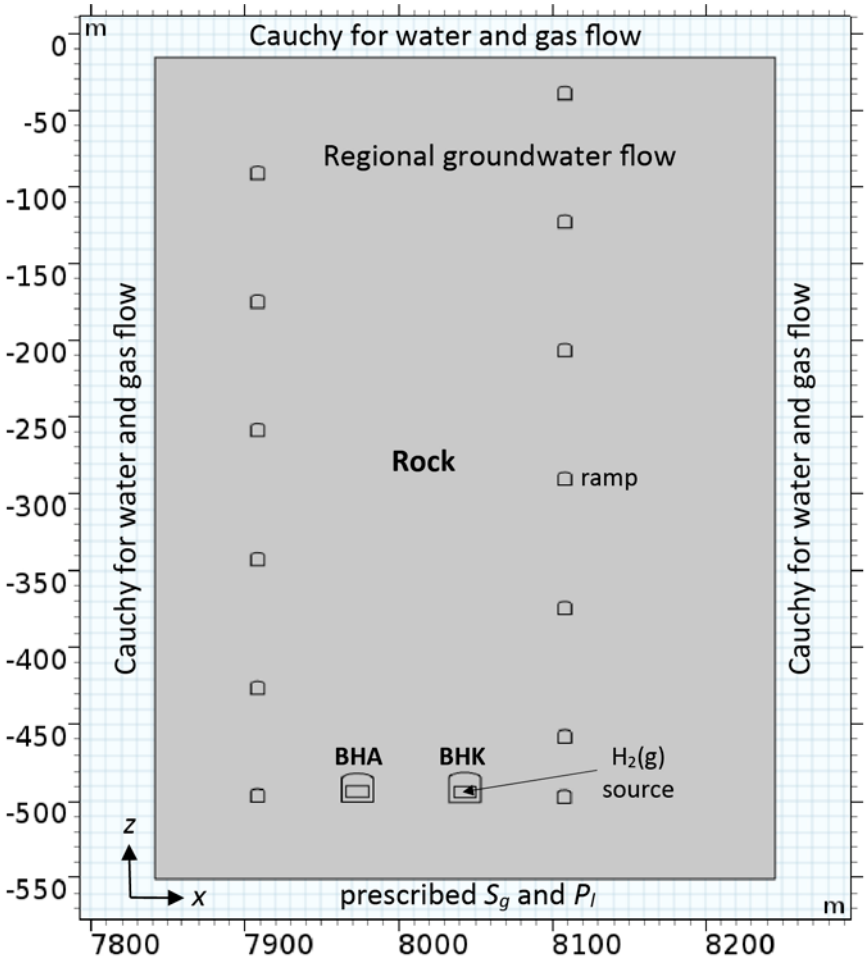

Figure 2-14. *Geometry and boundary conditions implemented in the COMSOL model of immiscible two-phase flow in the FF of the BHK vault. The location of the BHA vault and ramp are shown for reference.*

The lower left corner of the model domain is set at x = 7 841.9 m and z = −550.6 m (with the lower left corner of the BHK vault located at x = 8 033.4 m and z = −500.6 m). The plane intersecting the BHK vault is at the coordinate y = 7 264 m for Section A, and y = 7 154 m, for Section B.

2.6.2 Initial and boundary conditions

Regional groundwater flow conditions are assumed initially. The initial water pressure distribution is taken from the regional groundwater hydrology model (Joyce et al. 2019) and is presented in Figure 2-15. Note that CONNECTFLOW (Amec 2014) uses the residual pressure, P_r (Pa), as independent variable, which is defined by

$$P_r = P_l + \rho_0 g(z - z_0) \qquad \text{(Eq 2-11)}$$

where P_l (Pa) is the liquid pressure, ρ_0 = 1 000 kg/m^3 is the density of freshwater (Abarca et al. 2016), and z_0 = 0 m is a datum. The initial liquid pressure used in the COMSOL models are calculated through Equation (2-5).

The initial distribution of residual pressure clearly displays a spatial variation (see Figure 2-16). This is also reflected in the initial water velocity field, which is shown in Figure 2-17. Groundwater flow is mainly horizontal near the regolith-bedrock interface and higher in Section B. Also, in the high conductive zones near the vaults, water flows mainly downwards.

The initial saturation of the gas phase ($S_{g,ini}$) is set at zero throughout the domain. As in the NF models, Cauchy boundary conditions (Equation (2-6)) are applied at the top and lateral boundaries. The liquid pressure and gas saturation are prescribed at the bottom boundary (see Figure 2-14).

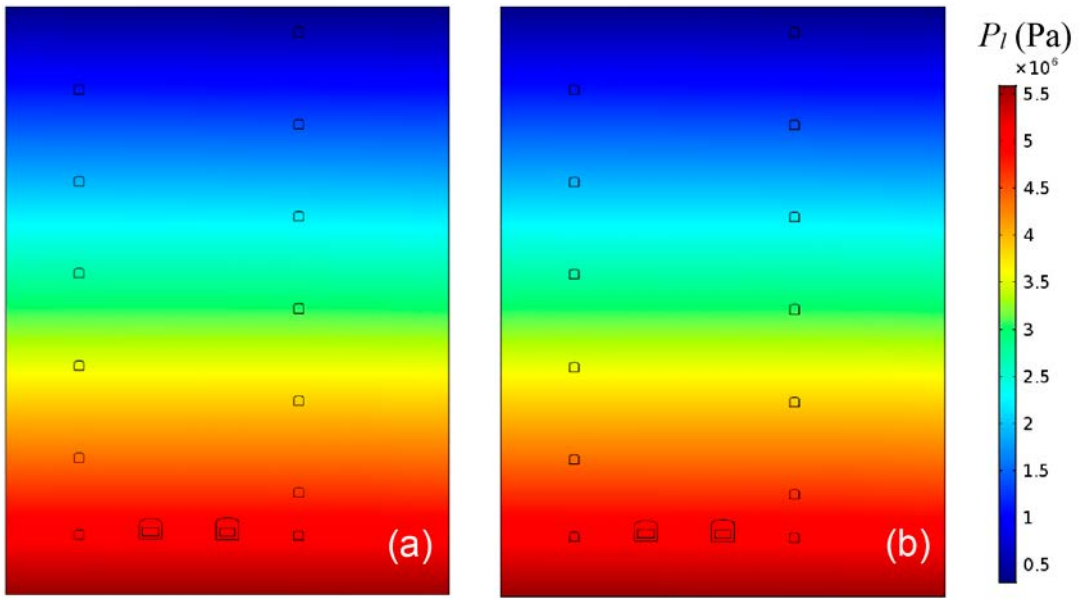

Figure 2-15. *Initial water pressure distribution under regional groundwater flow for: (a) Section A and (b) Section B.*

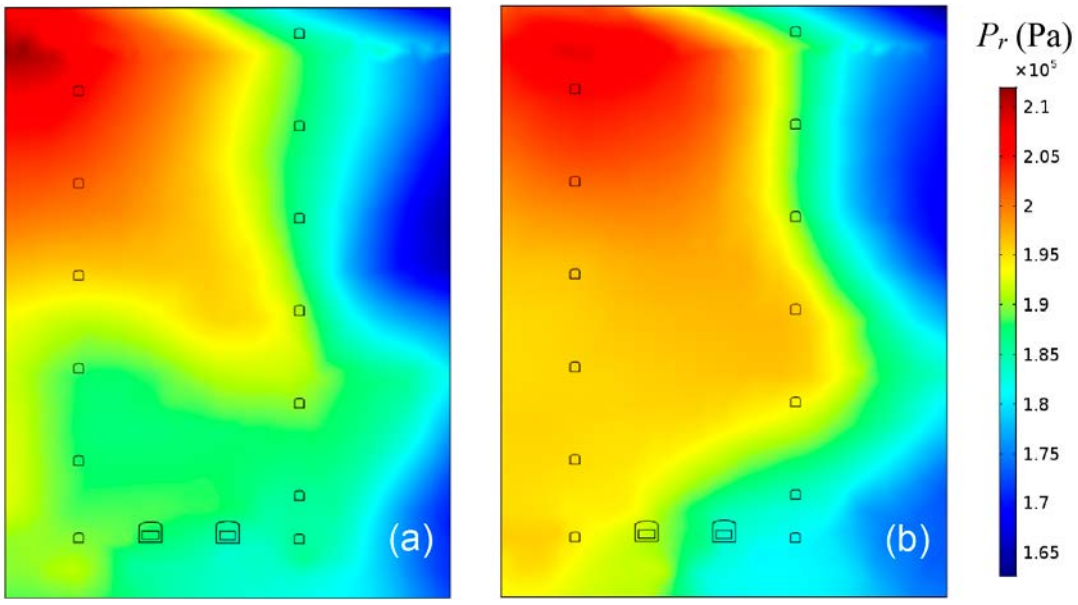

Figure 2-16. *Initial residual pressure distribution under regional groundwater flow for: (a) Section A and (b) Section B.*

2.6.3 Hydraulic and transport properties

The same water retention curves and relative permeability functions considered in the NF models are used in the FF models (see Section 2.2.3). The porosity field and permeability tensor obtained from the regional hydrological model (Joyce et al. 2019, Silva et al. 2019) are used in these models. The vertical component of the rock permeability and the porosity fields of the two selected cross-sections are shown in Figure 2-17 and Figure 2-18, respectively.

The density of the liquid phase was set at 1 000 kg/m^3, to be consistent with the initial liquid pressures (see Section 2.6.2). Excepting the liquid density, the remaining transport parameters of the liquid and gas phases are the same as in the NF models (see Section 2.1.4).

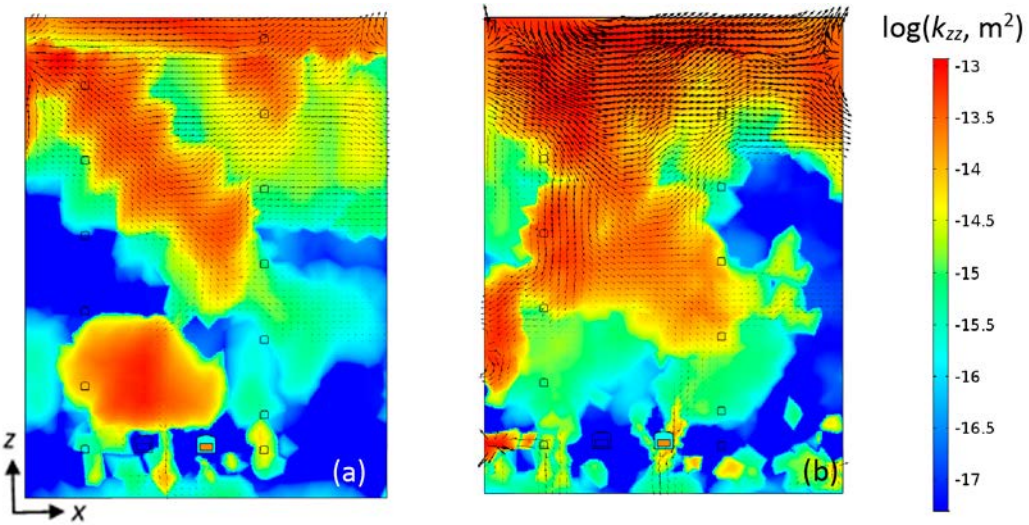

Figure 2-17. *Vertical permeability and initial water velocity fields (black arrows) of (a) Section A and (b) Section B. Arrows are plotted with the same logarithmic scale.*

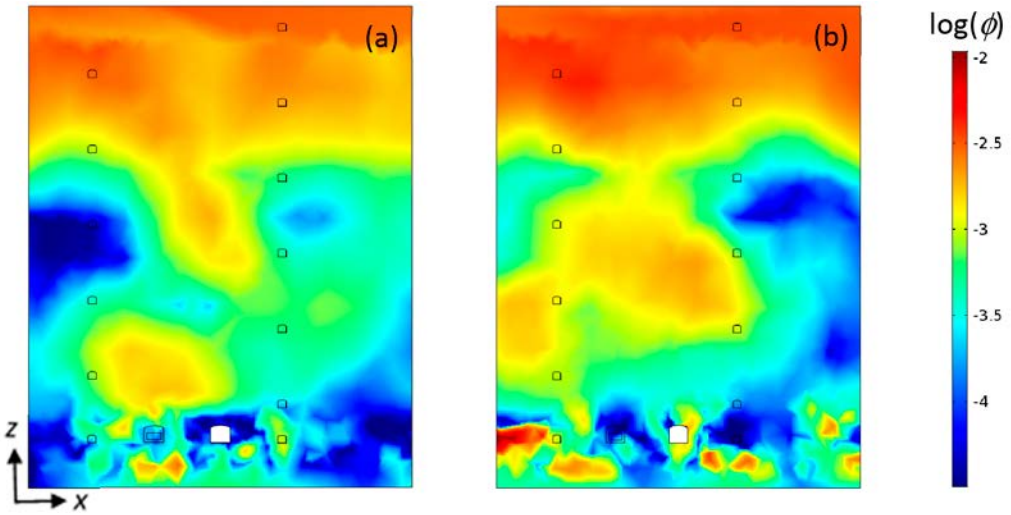

Figure 2-18. *Rock porosity fields of (a) Section A and (b) Section B.*

3 Numerical implementation

The governing equations of the P-S approach (see Section 2.1.3) were implemented in COMSOL Multiphysics 5.3 (https://www.comsol.com/) using the coefficient form of the partial differential equation (PDE) modelling interface

$$\mathbf{e_a}\frac{\partial^2\mathbf{u}}{\partial t^2}+\mathbf{d_a}\frac{\partial\mathbf{u}}{\partial t}+\nabla\cdot\left(-\mathbf{c}\nabla\mathbf{u}-\boldsymbol{\alpha}\mathbf{u}+\boldsymbol{\gamma}\right)+\boldsymbol{\beta}\cdot\nabla\mathbf{u}+\mathbf{a}\mathbf{u}=\mathbf{f} \qquad \text{(Eq 3-1)}$$

where $\mathbf{u}=(u_1,\ldots,u_k,\ldots,u_N)^T$ is a vector of N unknowns, $\mathbf{e_a}$ the mass coefficient, $\mathbf{d_a}$ the damping coefficient, $\mathbf{c}$ the diffusion coefficient, $\boldsymbol{\alpha}$ the conservative flux convection coefficient, $\boldsymbol{\beta}$ the convection coefficient, $\mathbf{a}$ the absorption coefficient, $\boldsymbol{\gamma}$ the conservative flux source term, and $\mathbf{f}$ the source term.

The P-S approach of two-phase flow is based on Equations (2-1) and (2-2). The state variables are the saturation of the gas phase (S_g) and the liquid pressure (P_l). Note that using the definition of capillary pressure the Darcy's flux of gas phase (Equation (2-3a)) can also be expressed as

$$\mathbf{q}_g=-\mathbf{k}\lambda_g\left(\nabla P_l+\frac{\partial P_c}{\partial S_g}\nabla S_g+\rho_g g\mathbf{z}\right) \qquad \text{(Eq 3-2)}$$

Substituting Equation (3-2) and the Darcy's flux of the liquid phase (Equation (2-3a)) into Equations (3-1) and (3-2), produces the following flow equations

$$\phi\rho_g\frac{\partial S_g}{\partial t}+\nabla\cdot\left(-\mathbf{k}\lambda_g\rho_g\nabla P_l-\mathbf{k}\lambda_g\rho_g\frac{\partial P_c}{\partial S_g}\nabla S_g-\mathbf{k}\lambda_g\rho_g^2 g\mathbf{z}\right)+\frac{\partial\left(\phi\rho_g\right)}{\partial t}S_g=\sum_{k=1}^{N}Q_g^k \qquad \text{(Eq 3-3)}$$

$$\begin{aligned}\phi\left(\rho_g-\rho_l\right)\frac{\partial S_g}{\partial t}+\nabla\cdot\left(-\mathbf{k}\left(\lambda_g\rho_g+\lambda_l\rho_l\right)\nabla P_l-\mathbf{k}\lambda_g\rho_g\frac{\partial P_c}{\partial S_g}\nabla S_g-\mathbf{k}\left(\lambda_g\rho_g^2+\lambda_l\rho_l^2\right)g\mathbf{z}\right)\\ +\frac{\partial\left(\phi\left(\rho_g-\rho_l\right)\right)}{\partial t}S_g=-\frac{\partial\left(\phi\rho_l\right)}{\partial t}+\sum_{k=1}^{N}\left(Q_l^k+Q_g^k\right)\end{aligned} \qquad \text{(Eq 3-4)}$$

Comparing Equations (3-3) and (3-4) with (3-1) the unknowns and coefficients for the P-S approach can be identified as

$$\mathbf{u}=\left(S_g,P_l\right)^T \qquad \text{(Eq 3-5a)}$$

$$\mathbf{e_a}=\mathbf{0} \qquad \text{(Eq 3-5b)}$$

$$\mathbf{d_a}=\begin{pmatrix}\phi\rho_g & 0\\ \phi\left(\rho_g-\rho_l\right) & 0\end{pmatrix} \qquad \text{(Eq 3-5c)}$$

$$\mathbf{c}=\begin{pmatrix}\lambda_g\rho_g\mathbf{k}\dfrac{\partial P_c}{\partial S_g} & \lambda_g\rho_g\mathbf{k}\\ \lambda_g\rho_g\mathbf{k}\dfrac{\partial P_c}{\partial S_g} & \left(\lambda_g\rho_g+\lambda_l\rho_l\right)\mathbf{k}\end{pmatrix} \qquad \text{(Eq 3-5d)}$$

$$\boldsymbol{\alpha}=\mathbf{0} \qquad \text{(Eq 3-5e)}$$

$$\boldsymbol{\gamma}=\begin{pmatrix}-\lambda_g\rho_g^2 g\mathbf{k}\mathbf{z}\\ -\left(\lambda_g\rho_g^2+\lambda_l\rho_l^2\right)g\mathbf{k}\mathbf{z}\end{pmatrix} \qquad \text{(Eq 3-5f)}$$

$$\boldsymbol{\beta} = \mathbf{0} \qquad \text{(Eq 3-5g)}$$

$$\mathbf{a} = \begin{pmatrix} \dfrac{\partial(\phi\rho_g)}{\partial t} & 0 \\ \dfrac{\partial(\phi(\rho_g - \rho_l))}{\partial t} & 0 \end{pmatrix} \qquad \text{(Eq 3-5h)}$$

$$\mathbf{f} = \begin{pmatrix} \sum_{j=1}^{N} Q_g^j \\ -\dfrac{\partial(\phi\rho_l)}{\partial t} + \sum_{j=1}^{N}\left(Q_l^j + Q_g^j\right) \end{pmatrix} \qquad \text{(Eq 3-5i)}$$

The partial derivatives in Equations (3-5d), (3-5h) and (3-5i) are calculated internally in COMSOL.

3.1 Model mesh, time-stepping and solver

The carbon steel corrosion time is 615 313 years (Section 2.1.5). The simulation time was set at 1 000 000 years to include the 2 steel corrosion regimes (Equation (2-4)), and the system evolution once gas generation has stopped.

3.1.1 NF models

The geometry of the NF models is discretized into 50 178 triangular elements. The mesh is illustrated in Figure 3-1.

Preliminary test simulations showed that the high contrast of hydraulic properties between the different materials of the vault causes abrupt changes of gas saturation at the interfaces. This negatively impacts numerical convergence. The difference in the hydraulic properties between the waste and backfill is significantly higher than between the backfill and the host rock (see Table 2-2 and Figure 2-9). For that reason, the mesh refinement in the waste and backfill sub-domains is higher than in the rock.

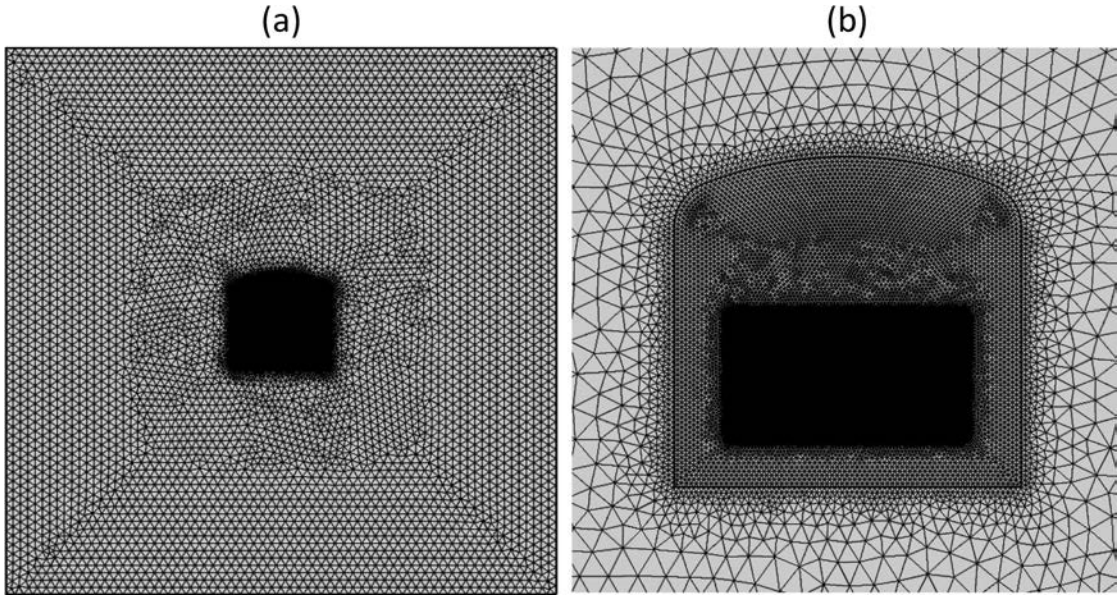

Figure 3-1. *(a) Numerical mesh of the full NF modelling domain and (b) a zoom in around the vault.*

Implicit Backwards Differentiation Formula (BDF, with maximum order of interpolating polynomial adjustable from 1, i.e. backward Euler, to 2) is used for time stepping. Steps taken by the solver are set as free with an initial step of 10^{-10} yr. The direct solver MUMPS with a memory allocation factor of 2 is used with the Newton-Raphson method using a constant damping factor of 1.0, a tolerance of 10^{-4} and a maximum number of iterations of 10. Test simulations showed that, for tolerances lower than 10^{-4}, the solution changes in less than 0.01 % when decreasing the tolerance in one order of magnitude.

The governing equations are solved in a coupled way with a Segregated Solver, using the constant Newton-Raphson method updating the Jacobian at all iterations.

3.1.2 NF models with a fracture zone

The geometry of the NF models including a fracture zone intersecting BHK is discretized into 57 892 triangular elements (see Figure 3-2). The discretization of the BHK vault is the same used in the NF model with homogeneous host rock. Moreover, the mesh refinement in the fracture zone and at the interface with the rock is high. This is to avoid numerical instabilities that can be derived from the high contrast of hydraulic properties between these subdomains.

The same solver used to solve the NF model $\phi$with homogeneous host rock was used to solve the model including a fracture zone.

3.1.3 FF model

The geometry of the FF model is discretized into 197 825 triangular elements (see Figure 3-3). The discretization of the BHK vault is the same used in the NF models (see Figure 3-1 and Figure 3-2). The same solver options used in the NF models were considered to solve the FF model.

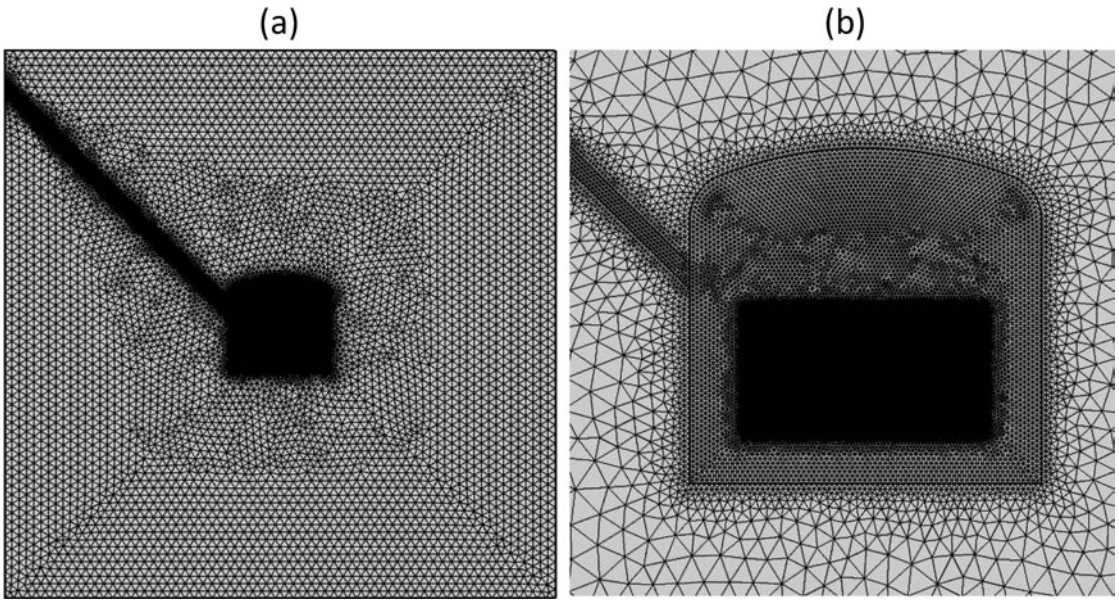

Figure 3-2. *(a) Numerical mesh of the full NF modelling domain with a fracture and (b) a zoom in around the vault.*

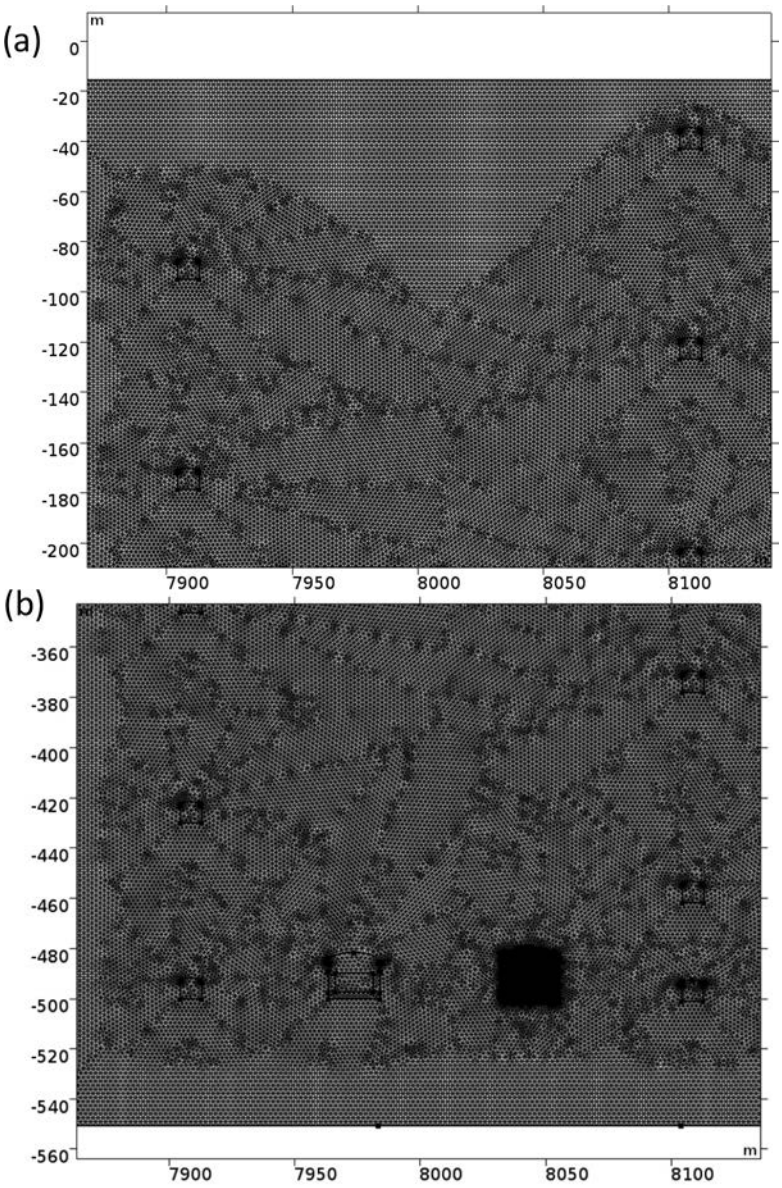

Figure 3-3. *Numerical mesh of the FF modelling domain (a) in the bottom and (b) in the top of the system.*

4 Results of NF models

The immiscible two-phase flow model presented in Section 2.1 to Section 2.5, is used to simulate several cases of hydrogen gas generation and migration in the NF. First, five simulation cases (see Section 1.2 and Table 1-1) are run to compare the flow behavior obtained assuming homogeneous and heterogeneous host rock. Rock heterogeneity is represented by a case of a homogeneous rock that includes a fracture zone, and two cross-sections of different hydraulic connectivity. In these simulation cases the gas generation rates are those described in Section 2.1.5 (Equation (2-4)). The main results of these simulations are described and discussed in Section 4.1. Next, the impact of larger gas production rates is evaluated through 10 additional simulation cases, whose results are presented in Section 4.2.

The methodology presented in Silva et al. (2019) is also used in the analysis of the results of the present work. This is based on the evolution of the following variables:

- Gas saturation distributions.
- Gas streamlines and velocity fields.
- Gas pressure at specific locations in and around the BHK vault.
- Average gas pressure ($\overline{p_g}$) and average gas overpressure ($\Delta\overline{p_g}$) in the BHK vault, calculated as

$$\overline{p_g}(t) = \frac{1}{V_{BHK}} \int_{V_{BHK}} p_g(t) dV \qquad \text{(Eq 4-1a)}$$

$$\overline{\Delta p_g}(t) = \overline{p_g}(t) - \overline{p_g}(0) \qquad \text{(Eq 4-1b)}$$

  In Equation (4-1a), V_{BHK} (m^3) is the volume of the BHK vault. The average gas pressure and average gas overpressure are a measure of the response of the BHK vault to the hydrogen generation and the departure of the system from its initial state, respectively. Also, they are used as indicators of the mechanical stability of the BHK vault (see Silva et al. 2019).

- Inflow ($Q_{\beta,in}$) and outflow ($Q_{\beta,out}$) rates (m^3/s) of water and gas to/from the BHK vault and waste compartment, given by

$$Q_{\beta,in} = \int_{\Sigma, \mathbf{q}_\beta \cdot \mathbf{n} \geq 0} \mathbf{q}_\beta \cdot \mathbf{n} dS \qquad \text{(Eq 4-2a)}$$

$$Q_{\beta,out} = \int_{\Sigma, \mathbf{q}_\beta \cdot \mathbf{n} < 0} \mathbf{q}_\beta \cdot \mathbf{n} dS \qquad \text{(Eq 4-2b)}$$

  In Equation (4-2), Σ is the surface of the BHK vault or the waste compartment, **n** is the unit vector normal to that surface, and $\beta = l, g$.

4.1 Comparison between homogeneous and heterogeneous host rock

The aim of Task 1 is to compare between the homogeneous (with and without a fracture zone) and heterogeneous rock concepts in the NF of the BHK vault. The description of the homogeneous and heterogenous rock models (geometry, initial and boundary conditions, flow and transport parameters) is given in Section 2.2 to Section 2.5. The numerical settings used to solve these NF models are found in Section 3.1.1 and Section 3.1.2.

Five simulation cases (see Table 1-1 and Table 4-1) were run for this task. Their motivation is explained in Section 1.2.

Table 4-1. Cases to study the influence of rock type on gas migration in the NF of the BHK vault.

Case #	Rock	Embedded fracture
1	homogeneous	–
2	homogeneous	fracture
3	heterogeneous (Section A)	–
4	heterogeneous (Section B)	–
5	heterogeneous (Section A)	fracture

4.1.1 Gas flow behavior

The evolution of the gas saturation distribution simulated in Cases 1 to 5 is shown in Figure 4-1 to Figure 4-8. Gas saturations of Case 1 and Case 2 are equal to those presented in Silva et al. (2019) when the water retention curves of the waste and backfill are the same. This helped to verify the homogeneous rock models, as the present simulations consider a finer spatial mesh and different boundary conditions at the lateral boundaries.

During the first 100 years the gas generated by the waste's steel corrosion does not escape from the BHK vault. Also, because hydrostatic conditions are considered in Cases 1 to 5, the gas flow pattern is not affected by the surrounding host rock (see, e.g. Figure 4-1 showing the gas distributions at 65 years).

The rock permeability around the BHK vault in Section A is about 2 orders of magnitude lower than in the homogeneous rock model. Also, although Section B presents a zone of high permeability crossing the vault, there are zones of permeability lower than the homogeneous rock permeability. Consequently, the gas flows in heterogeneous rock model (Cases 3 and 4) at lower velocities than in the homogeneous host rock model (Case 1), reaching the rock later (see, e.g. Figure 4-2). In all the cases, after a given time the gas reaching the rock starts to migrate upwards due to buoyancy.

In Section B (Case 4), the rock is highly heterogeneous near the vault. After 110 years, the gas starts to flow preferentially through these zones of high rock permeability (Figure 4-3d). By contrast, gas flow through the rock in Section A (Case 3) is still very slow at that time (Figure 4-3c). However, including a fracture zone in Section A (Case 5) increases the gas release from the vault (compare Figure 4-3c and Figure 4-3e), leading to a flow pattern like the one developed under homogeneous rock (Case 2). At 120 years, while in Case 4 the gas has reached the top of the system, in Case 3 it is still in the very near field of the vault (Figure 4-4). In the Case 4, at 120 years the gas has reached the top of the system. In contrast, in the Case 3 the gas is still very close to the vault (Figure 4-5). The gas saturations on top are remarkably lower than the saturations simulated in Case 1 and Case 4. In contrast, due to the very low rock permeability around the vault, the gas saturation in this zone is higher (Figure 4-5c) than in the remaining cases. The rock permeability in a zone localized left and above the vault of Section B (Case 4) also is very low. After 150 years, this causes local gas saturations of the same order as saturations around the vault in Case 3.

Silva et al. (2019) showed that a quasi-steady state gas flow in homogeneous rock is obtained within 1 000 years. The same occurs when the host rock is heterogeneous. The exception is when the rock permeability around the vault is low, which causes slow gas flow. For Case 3, the initial quasi-steady state is reached between 1 000 and 1 500 years. The maximum saturation of gas is approximately 2.3 %, 2.2 %, 6.5 %, 3.2 % and 4.3 % for Cases 1, 2, 3, 4 and 5, respectively (see, Figure 4-6). Silva et al. (2019) showed that when the host rock is homogeneous, the gas accumulates in the top backfill. This also happens when the rock is heterogeneous (see, e.g. Figure 4-3 and Figure 4-4). However, the heterogeneity degree around the near field of the vault can have a large effect on the gas amount and gas distribution within the backfill. As shown in Figure 4-6c, because the rock permeability very near the vault in Section A is almost homogeneous, the gas is distributed uniformly in the top backfill. In contrast, rock permeability around the vault in Section B is very heterogeneous. Therefore, the gas distribution on top backfill is non-symmetric (Figure 4-6d). Symmetry of gas distribution is also broken by including a fracture zone in Section A, as it is shown in Figure 4-6e. In Case 3, the maximum gas saturation is developed in the interface between the backfill top and rock. In Case 4, it is reached in the low permeability zone of the rock that is above the vault.

Both carbon and stainless steels corrosion proceed during the first 74 920 years. After this time, the hydrogen generation rate reduces to the corresponding value of carbon steel corrosion (see Equation (2-4)). This reduces the gas pressures in the vault and, accordingly, the gas saturation decreases through the most part of the vault, as it is shown in Figure 4-9.

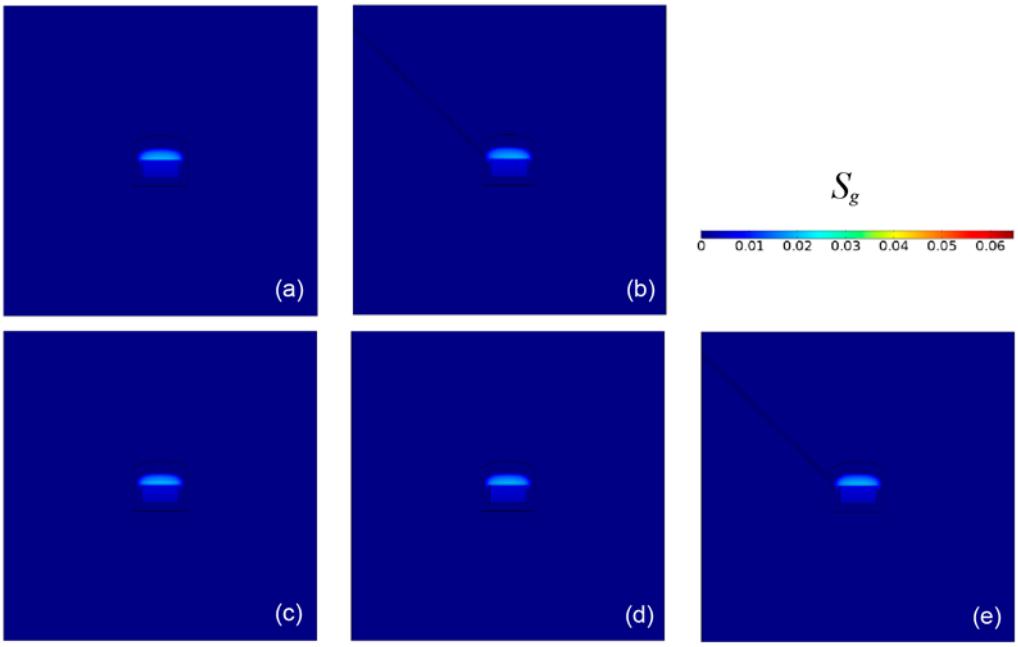

Figure 4-1. *Gas saturation at 65 years for (a) Case 1, (b) Case 2, (c) Case 3, (d) Case 4, (e) Case 5.*

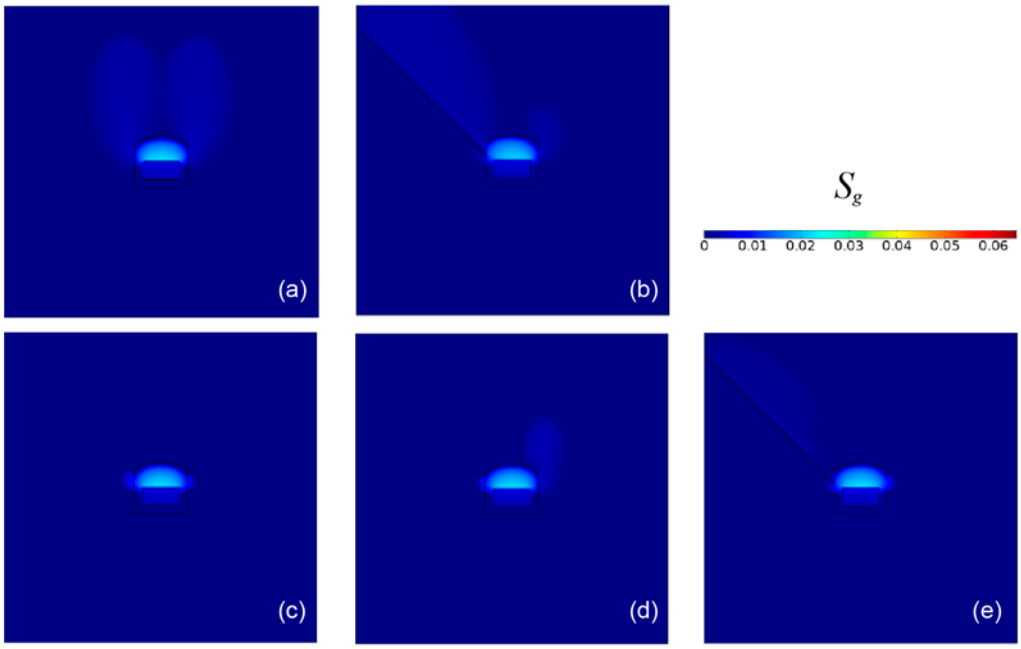

Figure 4-2. *Gas saturation at 105 years for (a) Case 1, (b) Case 2, (c) Case 3, (d) Case 4, (e) Case 5.*

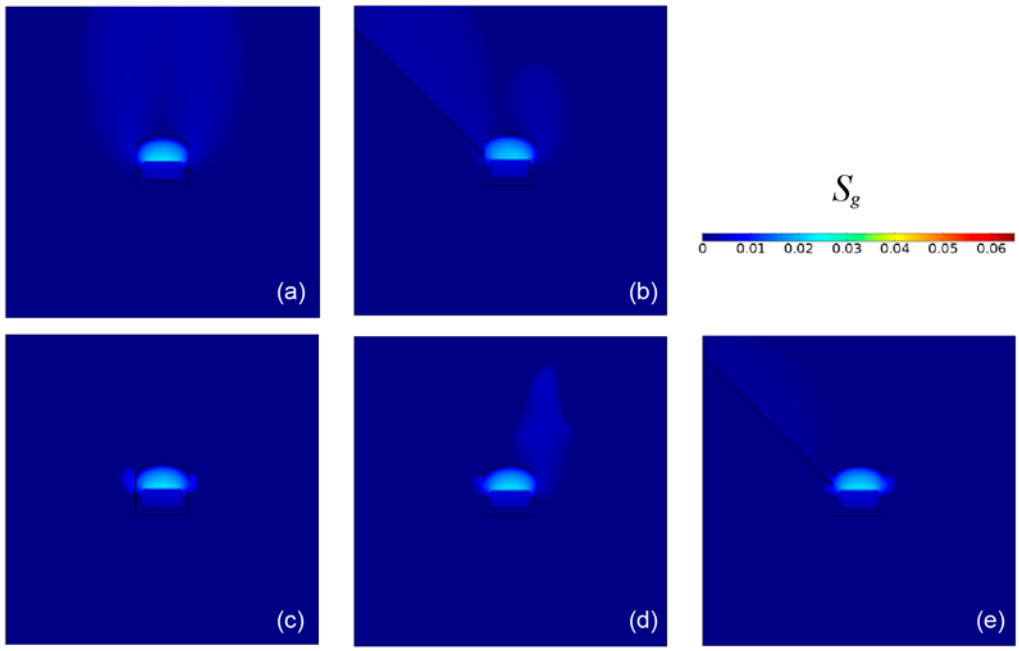

Figure 4-3. *Gas saturation at 110 years for (a) Case 1, (b) Case 2, (c) Case 3, (d) Case 4, (e) Case 5.*

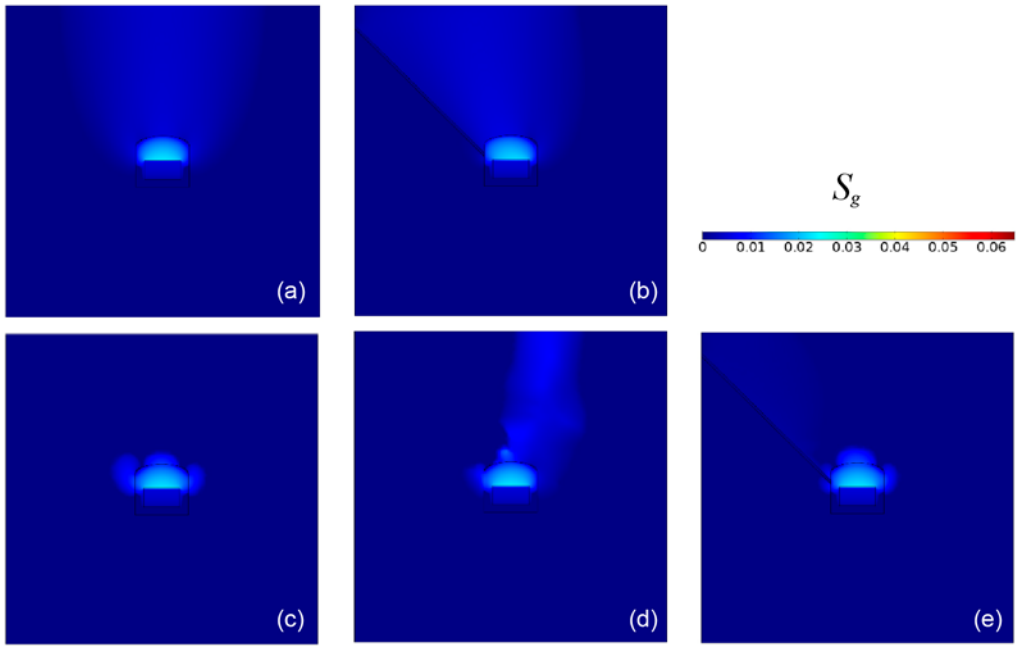

Figure 4-4. *Gas saturation at 120 years for (a) Case 1, (b) Case 2, (c) Case 3, (d) Case 4, (e) Case 5.*

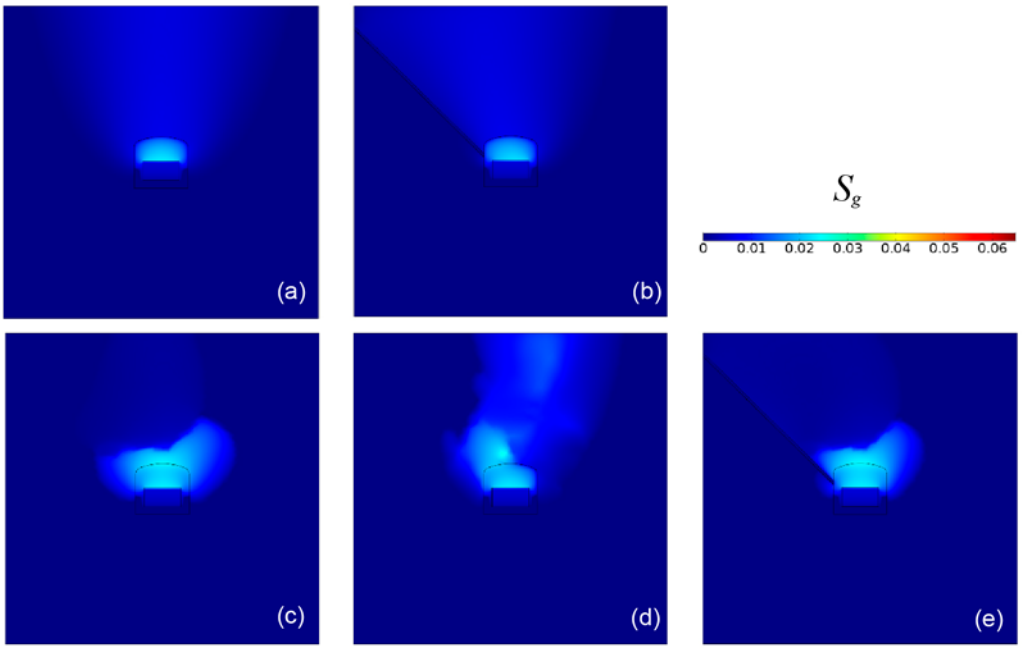

Figure 4-5. *Gas saturation at 150 years for (a) Case 1, (b) Case 2, (c) Case 3, (d) Case 4, (e) Case 5.*

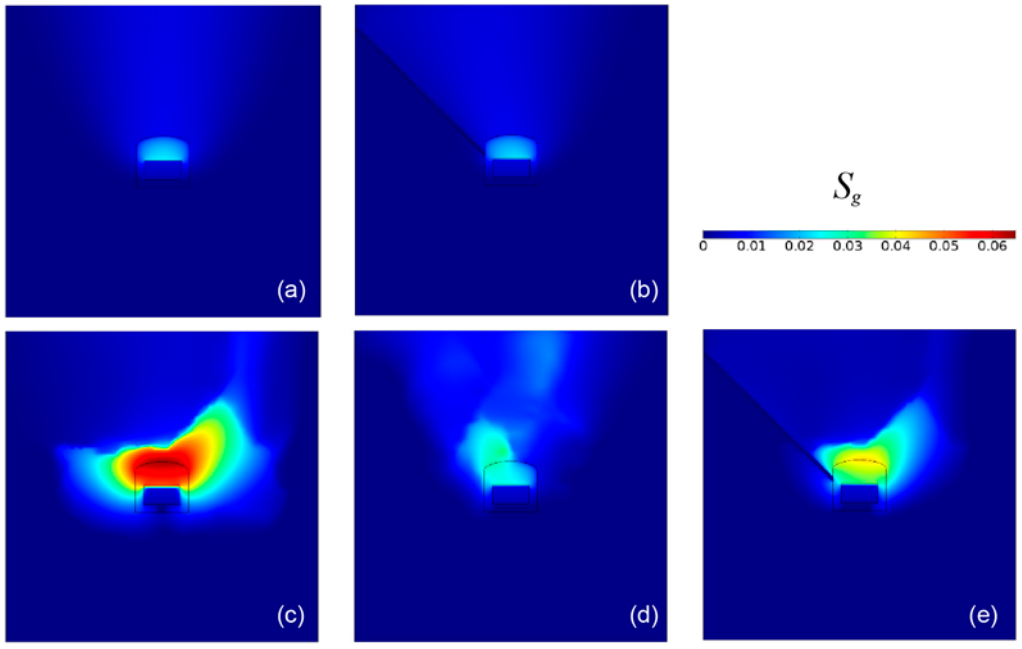

Figure 4-6. *Gas saturation at 1 000 years for (a) Case 1, (b) Case 2, (c) Case 3, (d) Case 4, (e) Case 5.*

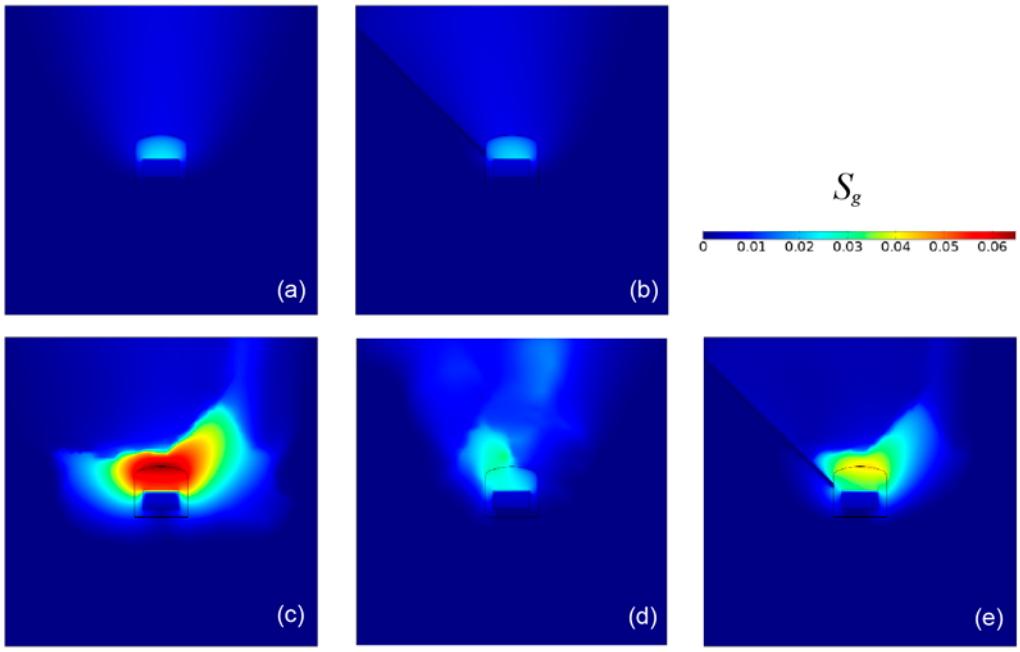

Figure 4-7. *Gas saturation at 1 500 years for (a) Case 1, (b) Case 2, (c) Case 3, (d) Case 4, (e) Case 5.*

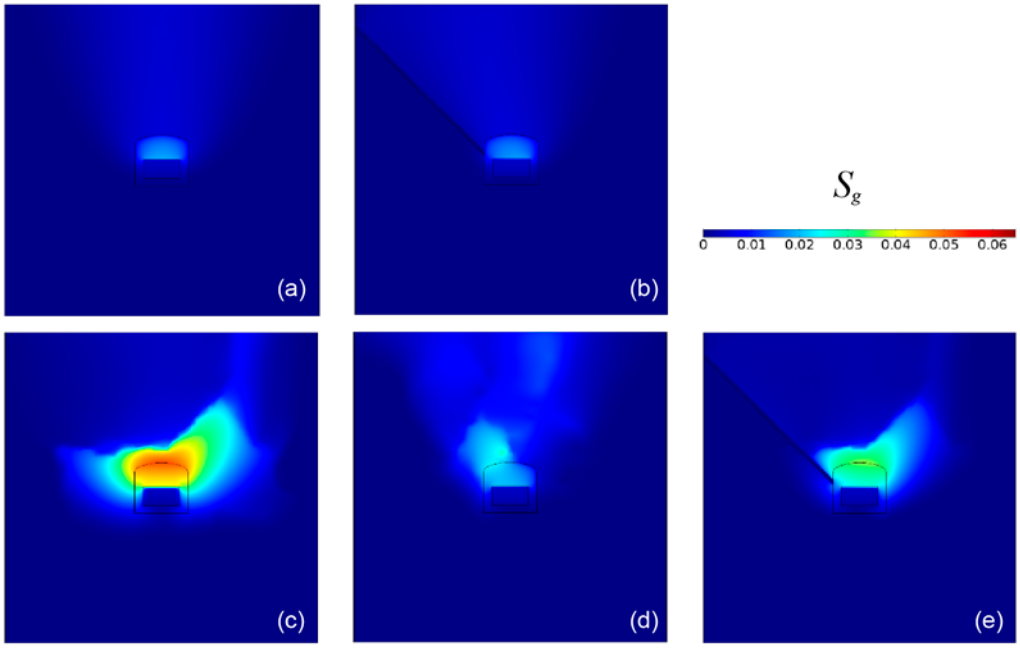

Figure 4-8. *Gas saturation at 615 500 years for (a) Case 1, (b) Case 2, (c) Case 3, (d) Case 4, (e) Case 5.*

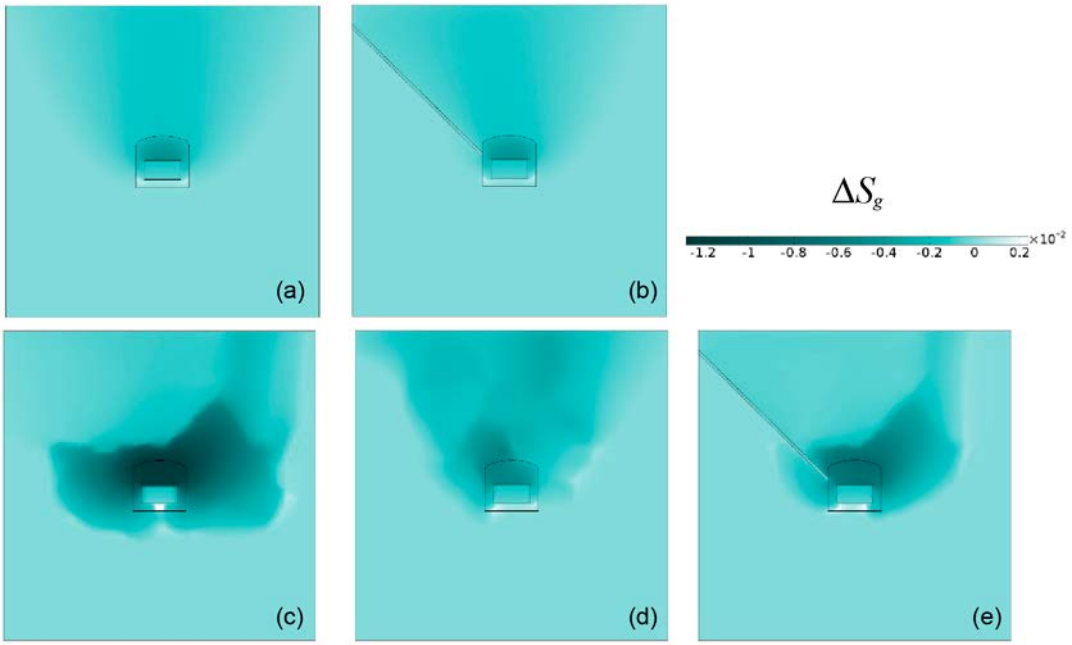

Figure 4-9. *Difference between the gas saturation distributions obtained after 615 500 and 1 000 years for (a) Case 1, (b) Case 2, (c) Case 3, (d) Case 4, (e) Case 5.*

Streamlines help identify gas pathways through the rock. Figure 4-10, Figure 4-11 and Figure 4-12 show the distribution of 100 gas streamlines reaching the top and lateral boundaries of the domain, after 150, 200 and 1 000 years, respectively. After 150 years, the gas has reached the top of the system in all cases. Compared to the homogeneous rock Case 1, a fracture zone (Case 2) causes gas to flow through the fracture and in the rock parallel to the fracture (see, e.g. Figure 4-10). Also, at early times, gas spreading in homogeneous rock (Case 1) is higher than in heterogeneous rock (Case 3 and Case 4). As the gas reaches zones of high permeability in Sections A and B, its spreading increases in these heterogeneous media (see, e.g. Figure 4-11c and Figure 4-11d). Interestingly, the inclusion of a fracture zone in Section A increases the number of streamlines flowing from the vault that reach the top boundary (compare Figure 4-10e with Figure 4-10c). This enhanced gas flow is caused by a zone where the fracture is in contact with a rock of high permeability.

Note that Section B has a zone of high permeability crossing the BHK vault obliquely, from left to right. Comparison of Figure 4-11b and Figure 4-11d suggests that this high permeability zone in Case 4 affects the gas flow in a similar way done by a fracture zone included in a homogeneous rock (Case 2). The shape of the streamlines extension is similar, but they are oriented in the opposite direction followed by the fracture zone considered in Case 2 and Case 5.

In summary, the gas released from the BHK vault flows in the heterogeneous host rock preferentially through zones of high permeability.

Rock heterogeneity also impacts the internal gas flow patterns of the vault. In heterogeneous rock, after 1 000 years, low permeability zones surrounding the BHK vault promote the formation of gas recirculation cells within the vault. This behavior is because, for low permeability host rock, the gas is less able to escape from the vault and accumulates on the top backfill due to buoyancy. This gas on top of the vault is then pushed by the new gas generated in the waste. This new gas tends to flow laterally due to the reduced flow of the gas that is close to the interface backfill-rock. As a result, a gas recirculation flow pattern within the backfill is generated close to the zones of the host rock with low permeability (see Figure 4-13 and Figure 4-14). This effect is more pronounced in the Case 3, where the vault is surrounded by a very low permeability zone (Section A). It is also found in Case 4 (Section B), for which a recirculation cell locates within the backfill that is directly in contact with a very low rock permeability zone (Figure 4-12d).

Note that for homogeneous host rock (Case 1), after 200 years, small gas recirculation cells are also developed in the backfill, above the top corners of the waste (Figure 4-11a and Figure 4-12a). This also happens in Case 2, but the fracture zone contributes to the disappearance of the recirculation cell in the left side of the vault (Figure 4-11b and Figure 4-12b).

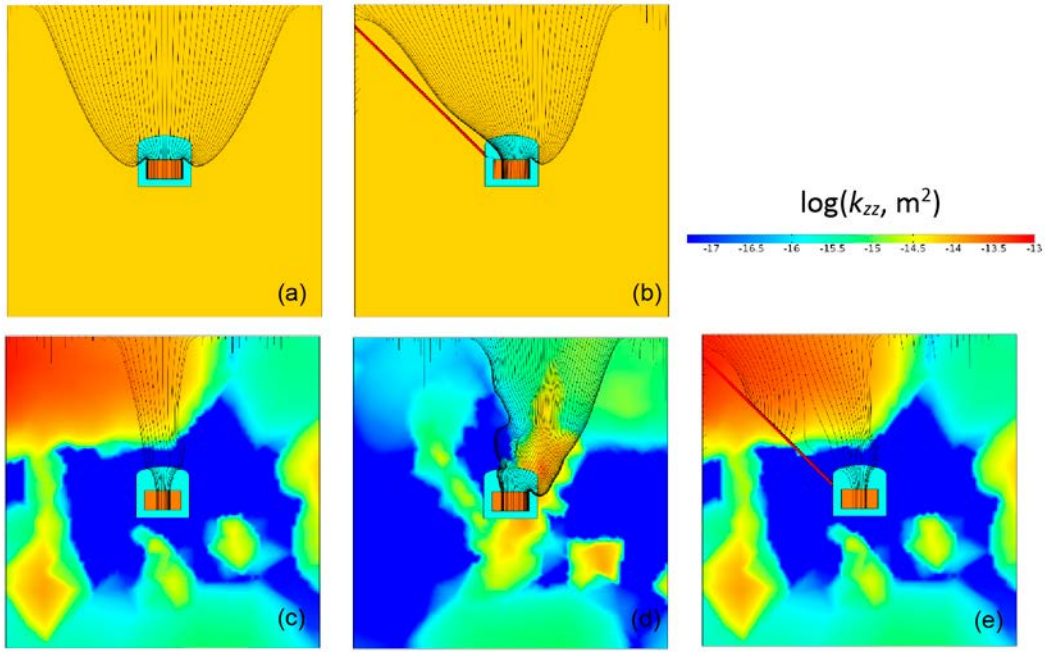

Figure 4-10. *Gas streamlines at 150 years for (a) Case 1, (b) Case 2, (c) Case 3, (d) Case 4, (e) Case 5. The vertical permeability of the rock is included as heterogeneity reference.*

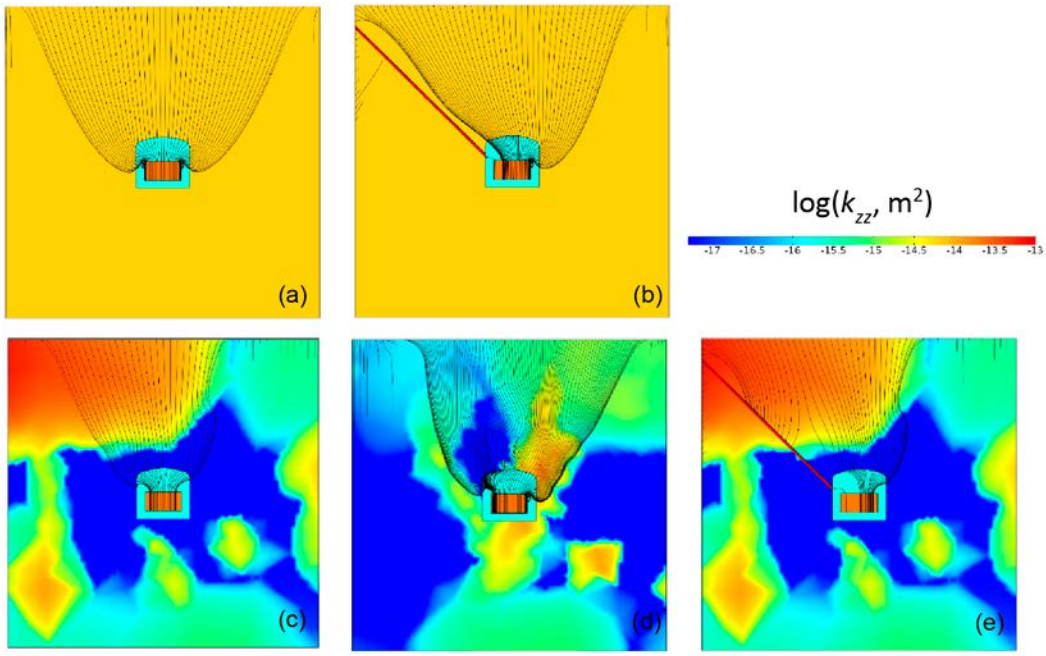

Figure 4-11. *Gas streamlines at 200 years for (a) Case 1, (b) Case 2, (c) Case 3, (d) Case 4, (e) Case 5. The vertical permeability of the rock is included as heterogeneity reference.*

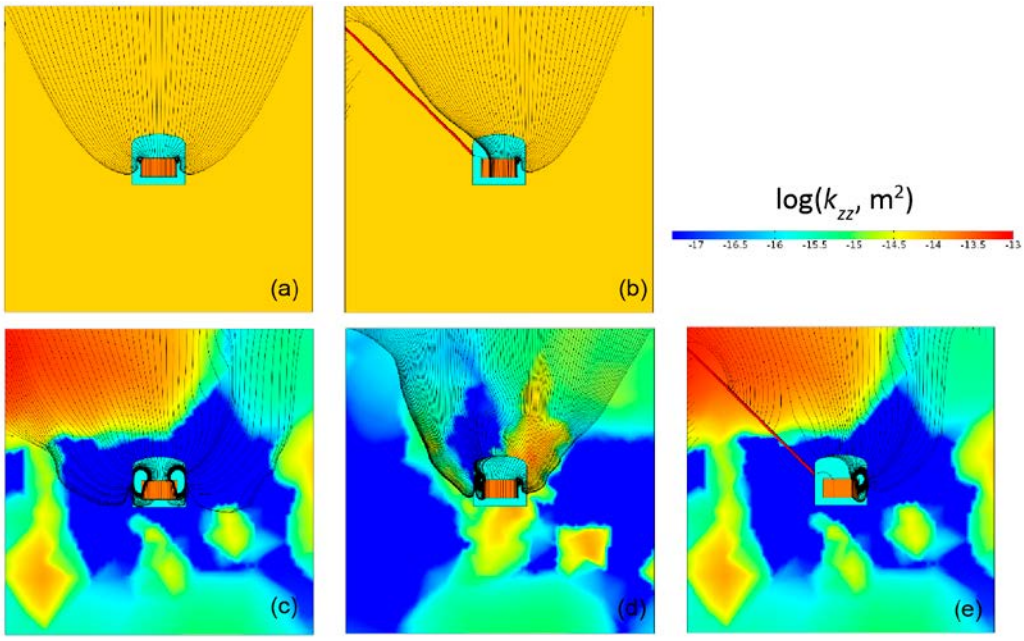

Figure 4-12. *Gas streamlines at 1 000 years for (a) Case 1, (b) Case 2, (c) Case 3, (d) Case 4, (e) Case 5. The vertical permeability of the rock is included as heterogeneity reference.*

A detailed view of the gas flow within the BHK vault is depicted in Figure 4-13 and Figure 4-14. These show the gas saturation distribution and streamlines, and the gas velocity field and magnitude after 1 000 years, respectively. In Case 3 (Section A) the host rock closest to the vault is homogeneous and has low permeability (see Figure 4-12c). This causes the gas flow pattern within the vault to be symmetric (see Figure 4-13c and Figure 4-14c). In contrast, Case 4 (Section B) presents much more heterogeneity of the rock closest to the vault. This results in asymmetric internal gas recirculation patterns (see Figure 4-13d and Figure 4-14d). Analogously, including a fracture zone in Section A (Case 5) affects the symmetry of the gas flow within the vault (see Figure 4-13e and Figure 4-14e). Note that the location of the gas recirculation cells within the backfill coincides with the location of low permeability zones in the rock (compare, e.g. Figure 4-13c, d and e with Figure 4-12c, d and e, respectively). This shows that rock permeability has a large impact on the internal flow of the BHK vault. Low rock permeabilities promote higher internal gas recirculation and an increase in the gas saturation and pressure within the vault.

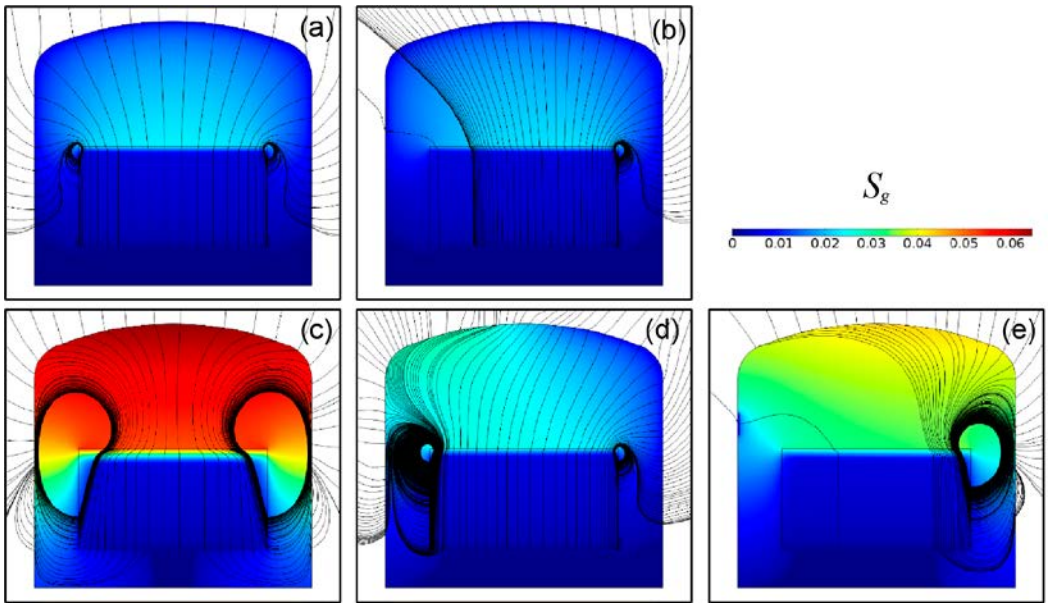

Figure 4-13. *Gas saturation and streamlines within the BHK vault at 1 000 years for (a) Case 1, (b) Case 2, (c) Case 3, (d) Case 4, (e) Case 5.*

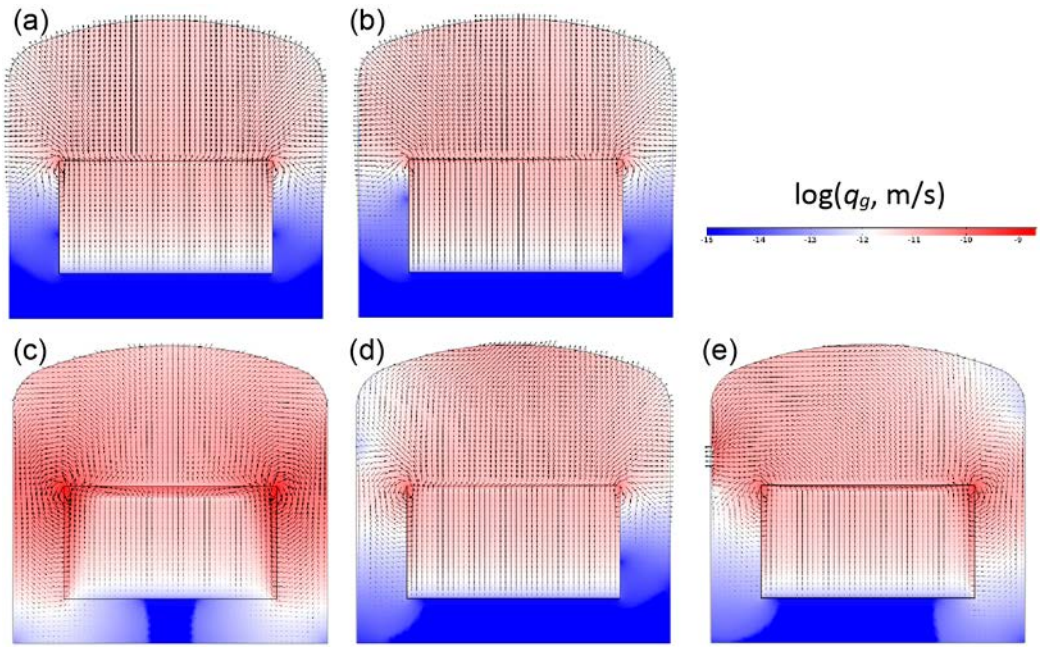

Figure 4-14. *Gas velocity field and magnitude within the BHK vault at 1 000 years for (a) Case 1, (b) Case 2, (c) Case 3, (d) Case 4, (e) Case 5.*

4.1.2 Gas pressures and overpressures

Figure 4-15 shows the evolution of the gas pressure at 6 different observation points distributed within and around the vault (Silva et al. 2019). These plots reflect mainly the hydrogen generation rates due to the corrosion of two types of steel. They also show the effect of the hydrogen migration through and around the BHK vault on local gas pressures. Note that rock heterogeneity does not impact the pressures within the waste compartment (OP2), except when the host rock includes a fracture zone (Cases 2 and 5). Also, host rock heterogeneity of Section B (Case 4) causes an evolution of local gas pressure that is like the one obtained in the homogeneous rock Case 1. This is because the average rock permeability of Section B in the very near field of the vault is close to the homogeneous rock permeability considered in Case 1. Additionally, when corrosion stops, the initial pressures in the rock are recovered faster when the host rock is homogeneous (compare solid grey, red and blue lines in Figure 4-15f).

The gas flow and pressures within the backfill are controlled by the permeability contrast between the waste and the backfill and between this and the host rock. Figure 4-16 shows the evolution of gas pressure within the vault during the stainless-steel corrosion period obtained in Case 1. The gas generated in the waste flows out, tending mainly to float and accumulate in the top backfill because the waste permeability is higher than the backfill permeability. However, after 10 000 years the gas also starts to fill the bottom backfill. This causes the pressure in the backfill to be higher than in the waste, leading to the gas pressure trend through OP1 to OP5 that is observed in Figure 4-15.

The rock heterogeneity not only affect the gas release but also its redistribution within the vault, which in turn can affect the evolution of internal pressures. Despite the gas pressures at OPs in the vault obtained in Case 1 and Case 4 are similar (Figure 4-15), the gas pressure distributions within the vault are different (compare Figure 4-16 and Figure 4-17). In Case 1 the gas pressure distributions are symmetric. In contrast, for Case 4, after 150 years the gas pressures at the top right are 2 bar lower than at the top left. This pressure difference coincides with a difference of about 3 orders of magnitude in the permeability of the adjacent zones of the rock. The presence of a fracture zone in a homogeneous rock (Case 2) also causes an asymmetric distribution of gas pressures in the vault (see Figure A-1). Lower pressures are developed in the backfill close to the contact with the fracture zone. The opposite occurs in Case 3. Because in Section A the rock closest to the vault is homogeneous, the gas pressure distributions within the vault are symmetric (see Figure A-2). Similar conclusions are derived for Case 5 (Figure A-3).

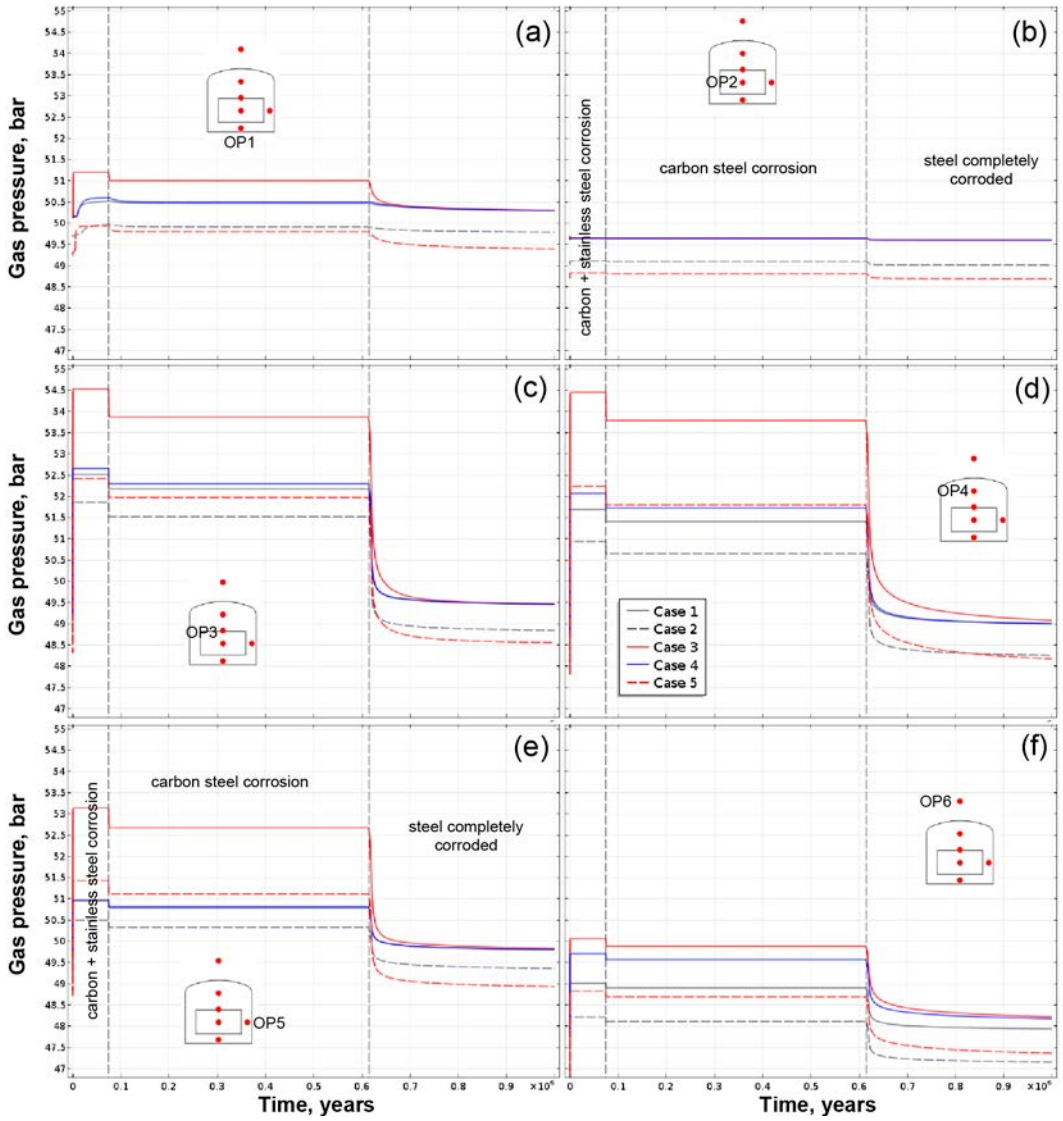

Figure 4-15. *Evolution of the gas pressure at 6 observation points distributed in and around the BHK vault: (a) OP1 backfill down, (b) OP2 waste, (c) OP3 above waste, (d) OP4 backfill up, (e) OP5 backfill right, (f) OP6 rock up.*

On the other hand, the gas recirculation flow pattern developed within the backfill correlates well with the gas pressure increase caused by rock parts of low permeability. For instance, the gas pressure within the backfill (OP3, OP4, OP5) simulated in Case 3 is about 2 to 3 bar higher than the respective pressures obtained in the other cases. Incidentally, observation points OP3, OP4 and OP5 lie close to gas recirculation cells. Moreover, including a fracture zone in the rock (grey and red dashed lines in Figure 4-15) leads to a reduction of the gas pressures (Case 1 versus Case2, Case 3 versus Case 5). This pressure reduction is higher in heterogeneous host rock (Case 5) than in homogeneous rock (Case 2). This is because the permeability of the rock in Section A (Cases 3 and 5) closest to the vault is 3 orders of magnitude lower than the permeability of the homogeneous rock assumed in Cases 1 and 2. Therefore, the fluid flow from the backfill to the rock is lower in Cases 3 and 5 than in Cases 1 and 2. Consequently, the gas flow through the fracture in Case 5 is higher than in Case 3.

The average gas pressure in the BHK vault in each case is shown in Figure 4-18b. In general, the differences found in the average gas pressure are due to the difference in the permeability of the rock that is close to the vault. Case 3 results in gas pressures and overpressures higher than for the other cases (about 1.5 bar higher than in Case 1). This is because the permeability of the rock surrounding the vault is uniform and very low. In contrast, the rock closest to the vault in Section B (Case 4) is more heterogeneous. The average rock permeability near the vault is close to the permeability of the homogeneous rock used in Cases 1 and 2. Consequently, the evolution of the average gas pressure in Case 4 is similar that obtained for the homogeneous rock Case 1.

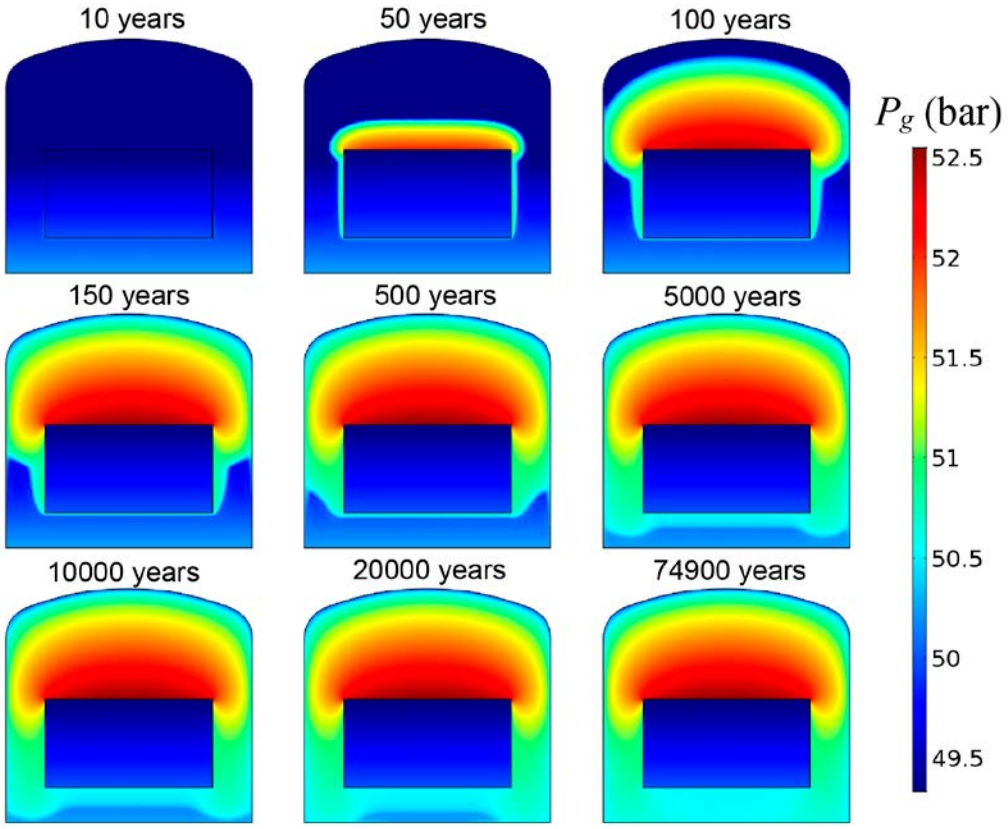

Figure 4-16. *Evolution of the gas pressure within the BHK vault during the stainless-steel corrosion period obtained in Case 1.*

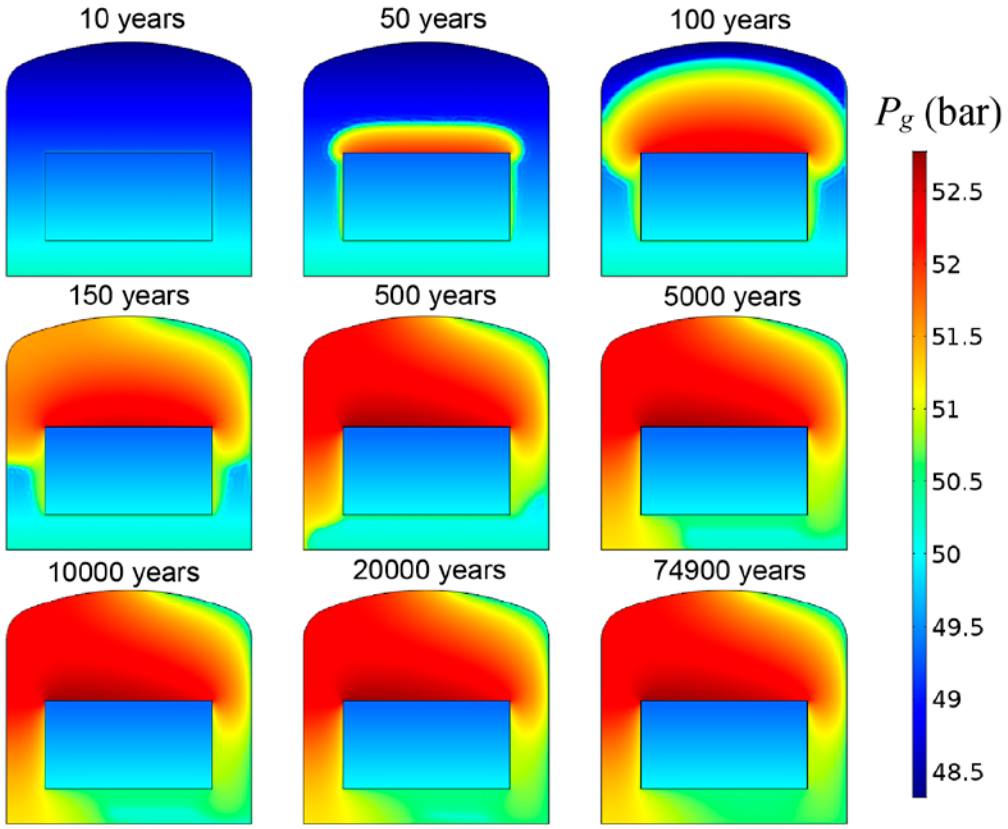

Figure 4-17. *Evolution of the gas pressure within the BHK vault during the stainless-steel corrosion period obtained in Case 4.*

The effect of the fracture zone on the average gas pressure within the BHK vault is shown in Figure 4-18a. The results show that the pressure in the vault is reduced when a fracture zone is included in the model (Case 1 versus Case2, Case 3 versus Case 5). As with the local gas pressures, this pressure reduction is higher in heterogeneous host rock (~ 1.5 bar) than in homogeneous rock (~ 0.7 bar).

Figure 4-18b also shows the average overpressure, which is the difference between the average gas pressure in the BHK vault and its initial value. Silva et al. (2019) demonstrated that including a fracture zone in a homogeneous host rock modifies the initial water pressure distribution. Because of the increased release of gas and water, the presence of the fracture zone helps to decrease the pressure within and around the BHK vault. This perturbation in the initial pressure field is more important as the permeability of the fracture zone is higher. Cases 3 and 4 considering heterogeneous host rock also modify the initial pressure distribution compared to Case 1. The initial average gas pressures in the BHK vault (equal to the initial average liquid pressure) are 49.33, 48.67, 49.38, 49.33, 48.41 bar for Cases 1, 2, 3, 4, 5, respectively. These pressures are due to the permeability contrast between the rock and the backfill. The host rock permeability closest to the vault in Cases 3 and 5 is 3 orders of magnitude lower than the permeability of the homogeneous rock assumed in Cases 1 and 2.

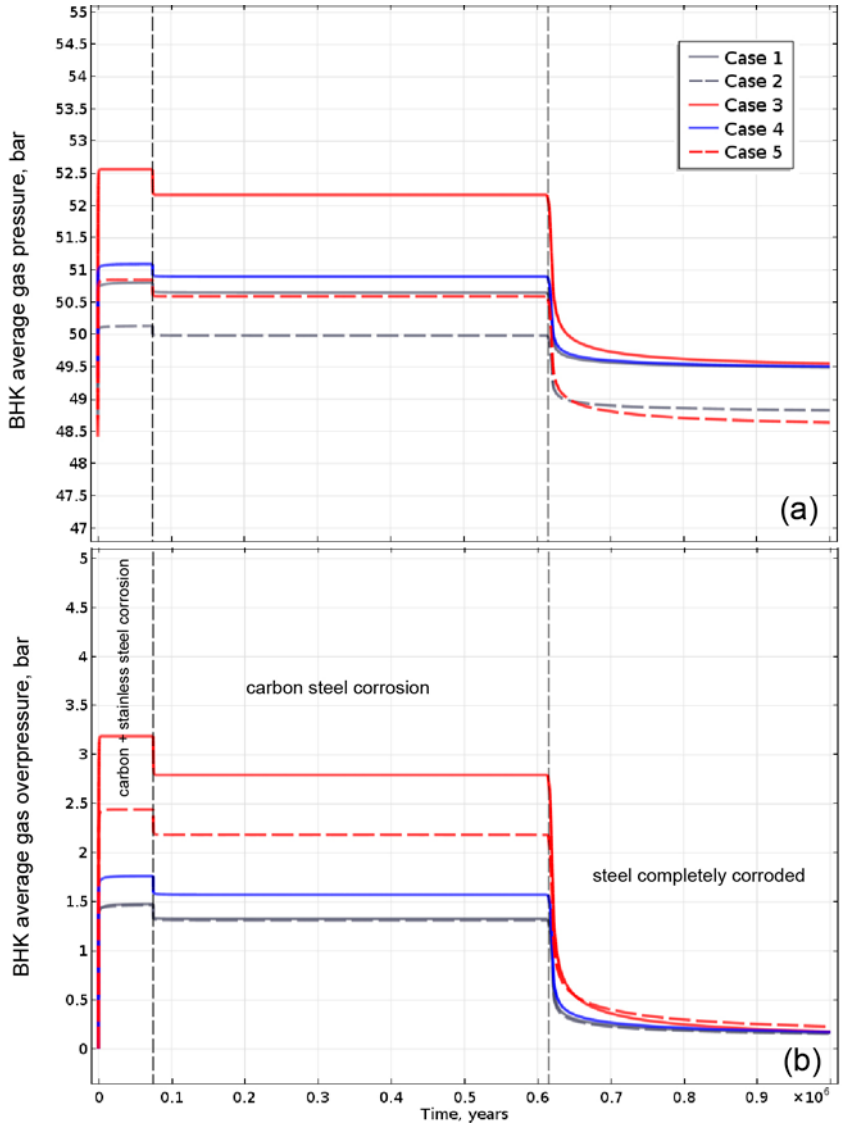

Figure 4-18. *Evolution of (a) the average gas pressure and (b) overpressure, in the BHK.*

Therefore, the average fluid flow from the backfill to the rock is lower in Cases 3 and 5 than in Cases 1 and 2, respectively. In contrast, the average rock permeability close to the vault in Case 4 is similar to the homogeneous rock permeability. This causes the initial average gas pressure to be the same in Case 1 and Case 4. The introduction of a conductive fracture zone has the effect to release the gas at a lower pressure. The overpressure reduction due to the fracture zone is not significant when the rock is homogeneous (Case 1 versus Case 2). Nevertheless, including a fracture zone in a heterogeneous rock with very low permeability closest to the vault (Section A), leads to a significant reduction in the overpressure. Note that, in Case 5, the difference between the permeabilities of the rock and the fracture is about 5 orders of magnitude. This causes a difference of about 0.5 bar in the gas overpressure obtained in Cases 3 and 5 (see the solid and dashed red lines in Figure 4-18b).

Finally, the maximum gas overpressure is in the range of 1.5 to 3.2 bar and is reached when both stainless and carbon steel corrode (Figure 4-18b). After the complete corrosion of stainless steel, the overpressure decreases by approximately 0.2 bar in Cases 1, 2, 4 and 5. This reduction is about 0.5 bar in Case 3. When corrosion stops, the overpressure decreases significantly, approaching 0.2 bar after 1 000 000 years in all the cases. Note that neglecting gas miscibility into water is a plausible approximation for the purposes of the present work. In practice, lower gas saturations and pressures will be obtained in the long term because H_2 gas dissolution into the groundwater. Also, hydrogen dissolution has a small effect on the water density. Thus, neglecting gas miscibility is an unfavorable scenario from the point of view of pressure build-up in the BHK vault.

Summarizing, pressures and overpressures obtained in a heterogeneous host rock including very low permeability zones, are higher than those obtained when the permeability of a homogeneous rock is relatively high. The selected 2D cross-sections of the host rock represent two limiting cases of very low and high rock permeability closest to vault. It should be noticed that Sections A and B do not account for the whole rock heterogeneity found across the length of the vault. In these 2D models the gas and water flow through the longitudinal axis of the vault is disregarded. The gas pressures in the BHK vault simulated in a 3D heterogeneous rock model could be lower than in 2D. This is due to the connectivity of high conductive rock areas through the backfill in the longitudinal direction.

4.1.3 Groundwater flow

Figure 4-19 shows the liquid pressure distributions obtained after 1 000 years in Cases 1 to Case 5 (see Table 4-1). Silva et al. (2019) showed that when no fracture zone is included in the model, the initial liquid pressure distribution is independent from the water retention curve of the BHK vault materials because the system is water saturated. The present results also show that rock heterogeneity does not affect the groundwater pressure field in the NF in Cases 3 and 4 (compare Figure 4-19a, c and d). This is because the simulated hydrogen generation rates (Equation (2-4)) cause gas saturations which are lower than 6 % (see Figure 4-6). These gas saturations are not sufficiently high to have an appreciable impact on the water pressure field. Thus, water flow is close to quasi-stationary throughout the entire simulation in Cases 1, 3 and 4.

Silva et al. (2019) also showed that when a fracture zone is included in a model with homogeneous rock, the system around the fracture zone close to the vault is depressurized (Figure 4-19b). When the fracture zone is included in the Section A, the water flow through the fracture zone increases significantly above the zone of low permeability (compare Figure 4-19b and Figure 4-19e). The liquid Darcy flux through the fracture zone obtained in Case 5 is about 1 order of magnitude higher than the liquid flux obtained in Case 2. This is because the rock permeability above the zone closest to the vault in Case 5 is more than one order of magnitude higher than the homogeneous rock permeability in Case 2. This increases the liquid flow from the rock to the fracture in this zone. In addition, the gas flow through the fracture zone obtained in Case 5 is about 5 times higher than in Case 2 (Figure 4-20). The combined effect is a higher flow of water through the fracture zone, as is shown in Figure 4-19e.

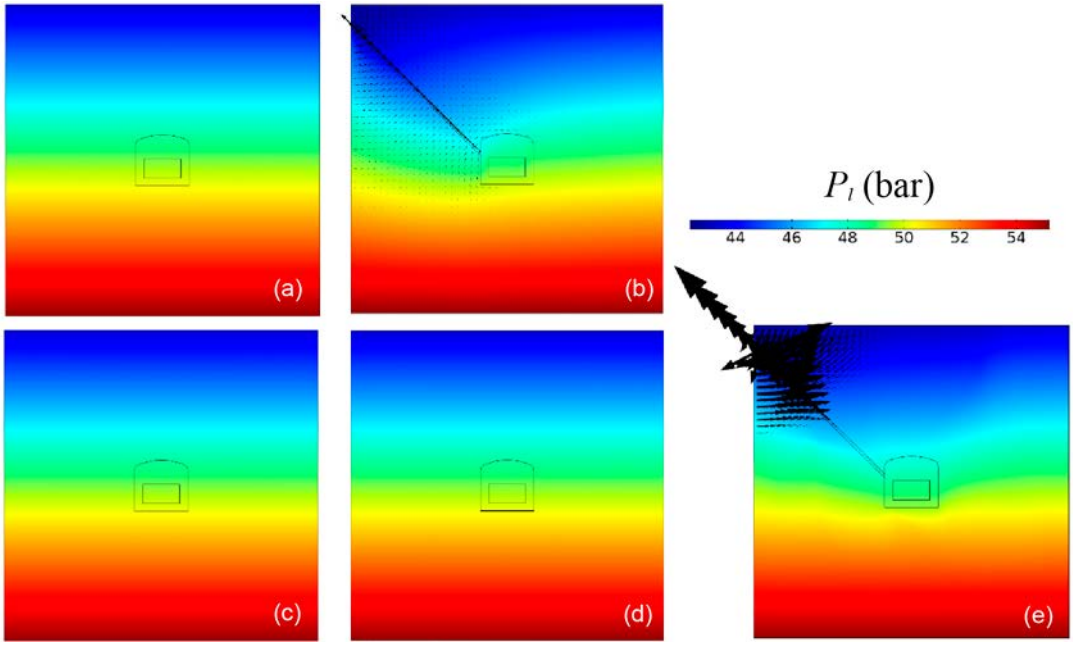

Figure 4-19. *Water pressure distribution obtained after 1 000 years for (a) Case 1, (b) Case 2, (c) Case 3, (d) Case 4, (e) Case 5.*

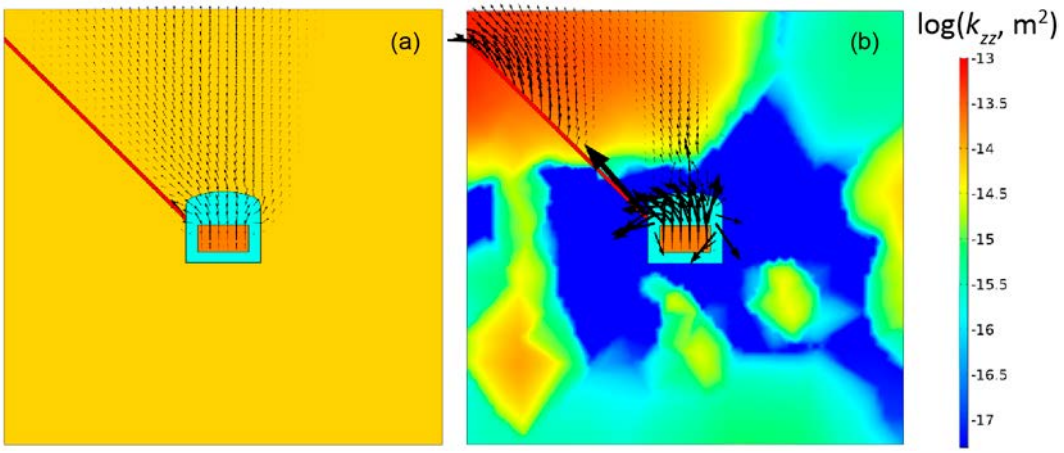

Figure 4-20. *Gas Darcy flux vector (black arrows) at 1 000 years for (a) Case 2, (b) Case 5. The vertical permeability of the rock is included as heterogeneity reference.*

4.1.4 Inflow and outflow rates

Table 4-2 summarizes the inflow and outflow rates to/from the BHK vault and the waste compartment (see Equation (4-2)) for simulation Cases 1 to 5. Note that these flowrates do not represent the actual magnitude of the fluxes (full scale of the vault), as they have been calculated assuming a vault thickness of 1.0 m. Therefore, they are used here only for comparison purposes.

As in Silva et al. (2019), in Cases 1, 3 and 4 the inflow and outflow rates of water to/from the BHK vault and waste are zero. This is because initial hydrostatic conditions are assumed and the effect of gas generation on the water pressure field is too small. Rock heterogeneity and the contrast of permeability between the backfill and the host rock affects the outflow rates of gas. For instance, after 1 000 years, the gas outflow rates from the vault simulated in Case 1 and Case 4 are similar. This is because, on average, the rock permeability of Section B is close to the rock permeability

considered in Case 1. Note that the number and distribution of streamlines crossing the vault, simulated in Cases 1 and 4 are similar (compare Figure 4-12a and Figure 4-12d). At the same time, the gas outflow rates from the vault calculated in Case 3 are slightly lower. In contrast, the recirculation cell flow pattern developed within the backfill in Case 3 at 1 000 years (see Figure 4-12c) enhances the gas inflow and outflow rates from the waste compartment. This is because the Darcy gas fluxes to and from the waste compartment are higher in Case 3 (see Figure 4-14c). Consequently, the gas inflow and outflow rates calculated according to Equation (4-2) are about 8 and 6 times higher than in Case 1 and Case 4, respectively.

On the other hand, Silva et al. (2019) showed that for homogeneous rock including a fracture, initially the system around the fracture close to the vault is depressurized. The departure from the initial hydrostatic conditions (homogeneous rock without a fracture) is higher for higher fracture zone permeabilities. Consequently, the fracture significantly affects the water inflow and outflow rates from the vault (compare the third and fourth columns of Cases 1 and 2 in Table 4-2). This also occurs when the heterogeneous rock (Section A) includes a fracture zone. Nevertheless, the impact on water inflow and outflow rates is lower. This is because the very low permeability of the rock adjacent to the vault in Section A, reduces the water flow in this zone (compare the third and fourth columns of Cases 3 and 5 in Table 4-2). Moreover, the gas outflow rates from the vault and waste increases in about 5 % and 8 %, respectively, when the host rock is homogeneous (compare the fifth and eight columns of Cases 1 and 2 in Table 4-2). The gas outflow rates from the waste obtained in Case 5 are 3 times lower than the gas outflow rates obtained in Case 3 (compare the eighth column of Cases 3 and 5 in Table 4-2). This is because the fracture zone reduces the internal gas recirculation flow (compares Figure 4-13c and e, and Figure 4-14c and e).

Table 4-2. Inflow and outflow rates (m^3/year) of water (Q_l) and gas (Q_g) to/from the BHK vault and the waste compartment.

Time, years		BHK vault			Waste compartment		
		$Q_{l,in}$	$Q_{l,out}$	$Q_{g,out}$	$Q_{l,in}$	$Q_{l,out}$	$Q_{g,out}$
Case 1	0	0	0	0	0	0	0
	1 000	0	0	3.87E−03	0	0	3.60E−03
	74 900	0	0	3.21E−03	0	0	2.98E−03
	615 000	0	0	8.86E−04	0	0	6.23E−04
	1 000 000	0	0	1.25E−05	0	0	1.20E−05
Case 2	0	3.89	3.89	0	4.92E−01	4.92E−01	0
	1 000	3.30	3.46	4.06E−03	3.62E−01	3.60E−01	3.90E−03
	74 900	3.28	3.45	4.06E−03	3.58E−01	3.56E−01	3.91E−03
	615 000	3.34	3.51	2.09E−03	3.71E−01	3.68E−01	2.01E−03
	1 000 000	3.74	3.93	1.00E−08	4.74E−01	4.67E−01	2.56E−09
Case 3	0	0	0	0	0	0	0
	1 000	0	0	3.62E−03	0	0	2.76E−02
	74 900	0	0	3.48E−03	0	0	2.62E−02
	615 000	0	0	1.82E−03	0	0	1.17E−02
	1 000 000	0	0	2.16E−08	0	0	3.27E−09
Case 4	0	0	0	0	0	0	0
	1 000	0	0	3.83E−03	0	0	4.56E−03
	74 900	0	0	3.83E−03	0	0	4.56E−03
	615 000	0	0	2.00E−03	0	0	2.35E−03
	1 000 000	0	0	1.08E−08	0	0	2.80E−09
Case 5	0	4.69E−02	4.69E−02	0.	3.75E−02	3.75E−02	0
	1 000	3.57E−02	3.79E−02	3.86E−03	3.10E−02	3.06E−02	6.91E−03
	74 900	3.52E−02	3.75E−02	3.87E−03	3.08E−02	3.02E−02	6.94E−03
	615 000	3.64E−02	3.87E−02	2.01E−03	3.16E−02	3.11E−02	3.50E−03
	1 000 000	4.35E−02	4.56E−02	2.55E−08	3.64E−02	3.57E−02	3.59E−09

The influence of rock heterogeneity in a system including a fracture zone is analyzed by comparing Case 2 and Case 5. For these cases water inflow and outflow rates to/from the vault and the waste decreases during the stainless-steel corrosion period. Gas outflow from the vault increases in this period. The fracture zone causes that water outflow rates from the vault are higher than water inflow rates from the vault. For Case 2, the maximum relative difference is about 5.1 %. The corresponding maximum difference between the in and out water flowrates in the waste is about 1.5 %. For Case 5, these differences are 6.5 % and 2 %, respectively. Also, water flowrates through the vault in Case 5 are 2 orders of magnitude lower than in Case 2. Meanwhile, water flowrates through the waste in Case 5 are 1 order of magnitude lower than in Case 2. This is because the permeability of the host rock closest to the vault in Section A is about 3 orders of magnitude lower than the permeability of the homogeneous rock in Case 2. In addition, during the first 74 900 years, the gas outflow rates from the vault in Case 5 is about 5 % lower than in Case 2. In contrast, the gas outflow rates from the waste in Case 5 is nearly 2 times the flow rates obtained in Case 2. This shows that the low permeability of the rock closest to the vault in Section A (Case 5) causes that gas flows out preferentially through the fracture zone.

4.2 Influence of larger hydrogen gas production

In the following set of simulation cases the effect of larger gas generation rates is studied. The objective of Task 2 is to analyze the influence of larger hydrogen gas production in the NF of the BHK. To that end, the five models considered in Section 4.1 (Task 1) were run again by increasing the hydrogen generation rates by a factor of 2 and 10. Note that, when the corrosion rate is higher the steel corrodes faster, because the initial mass of steel is assumed to be the same. Because the corrosion rates are constant, the initial mass of steel decreases linearly with time. Therefore, when the hydrogen generation rate is doubled, the corrosion times of stainless and carbon steel are $t_{c,ss}$ = 37 460 years and $t_{c,cc}$ = 307 656.5 years. For a hydrogen generation rate 10 times higher than $r_{H2(g)}$, the corrosion times are $t_{c,ss}$ = 7 492 years and $t_{c,cc}$ = 61 531.3 years. The description of the homogeneous rock models is given in Sections 2.2 and 2.3. The heterogeneous host rock models are detailed in Sections 2.4 and 2.5. The numerical settings used to solve these NF models are found in Section 3.1.1 and Section 3.1.2.

The above results in a total of 10 new simulation cases (see Table 1-1 and Table 4-3), whose motivation is explained in Section 1.2. Sequences of Cases 6 to 10, and Cases 11 to 15, are equivalent to that of Cases 1 to 5 (Table 4-1), but considering a gas generation rate 2 and 10 times higher, respectively.

Table 4-3. Cases to study the impact of higher gas production rates on gas migration in the NF ofthe BHK vault.

Case #	Rock	Embedded fracture	Gas generation rate
6	homogeneous	–	
7	homogeneous	fracture	
8	heterogeneous (Section A)	–	$2r_{H2(g)}$
9	heterogeneous (Section B)	–	
10	heterogeneous (Section A)	fracture	
11	homogeneous	–	
12	homogeneous	fracture	
13	heterogeneous (Section A)	–	$10r_{H2(g)}$
14	heterogeneous (Section B)	–	
15	heterogeneous (Section A)	fracture	

The simulation cases that consider homogeneous host rock are analyzed first. Next, the impact of higher gas production when the host rock is heterogeneous is studied in Section 4.2.2. The effect of heterogeneity on the groundwater flow is analyzed in Section 4.2.3.

4.2.1 Homogeneous host rock

Here the simulation Cases 6, 7, 11 and 12 (Table 4-3) are compared to Cases 1 and 2 (Table 4-1). The gas saturation distributions obtained during the first 1 000 years is shown in Figure 4-21 to Figure 4-24. During this period, both stainless and carbon steel corrode simultaneously in all the cases. Qualitatively, the evolution of the gas in the NF is similar for different hydrogen generation rates.

As expected, higher gas generation rates lead to a faster gas release and flow through the rock. After 20 years, for Cases 1 and 2 the gas generated in the waste still does not leave the waste (Figure 4-21a and Figure 4-21b). For double gas production rate (Cases 6 and 7), a small amount of mass has reached the backfill (Figure 4-21c and Figure 4-21d). On the contrary, for gas production rates 1 order of magnitude higher the gas has filled a large extension of the top backfill and is released from the vault (Figure 4-21e). It has covered the whole fracture zone in Case 7 (Figure 4-21f).

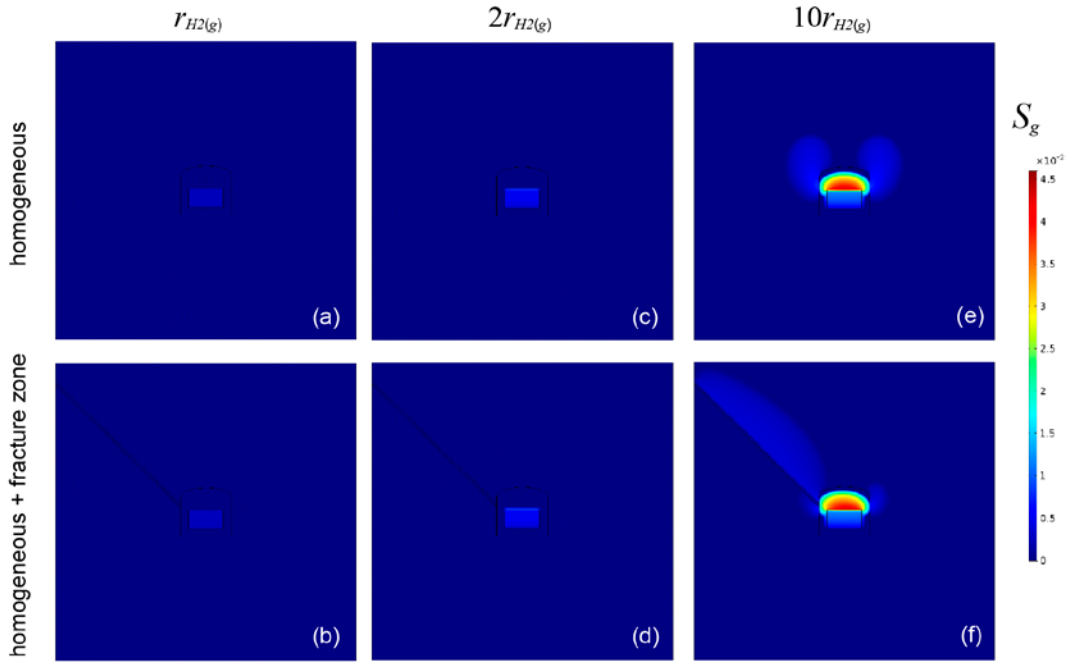

Figure 4-21. *Gas saturation at 20 years for (a) Case 1, (b) Case 2, (c) Case 6, (d) Case 7, (e) Case 11, (f) Case 12.*

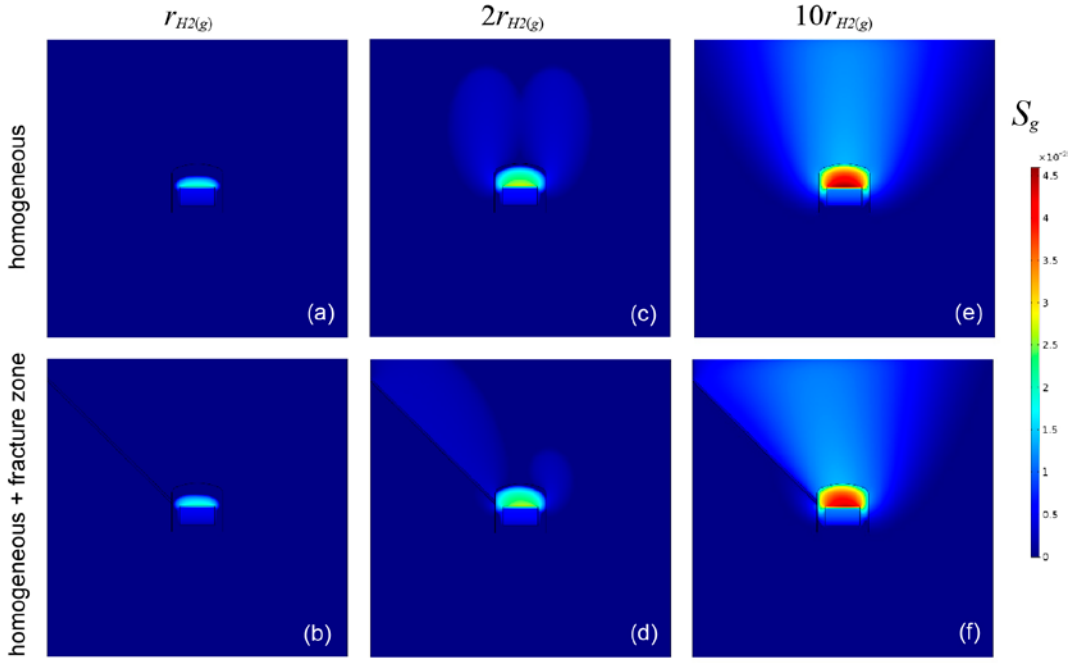

Figure 4-22. *Gas saturation at 65 years for (a) Case 1, (b) Case 2, (c) Case 6, (d) Case 7, (e) Case 11, (f) Case 12.*

After 65 years, the gas has almost reached the quasi-steady state under very high gas production rates (Case 11). For instance, the gas saturation distributions in Figure 4-22e is very similar to the distributions found at 100 and 1 000 years, shown in Figure 4-23e and Figure 4-24e, respectively. This occurs even sooner when the host rock includes a fracture zone (Case 12). For Case 6 (double corrosion rate), the gas still has not reached the top boundary after 65 years. Likewise, in Case 7 gas has migrated through the entire fracture zone and in the rock above the fracture.

In Cases 1 and 2 gas flow occurs only inside the vault after 65 years. The quasi-steady state gas flow is reached after 1 000 years in all the cases. As in Cases 1 and 2, the maximum gas saturations develop within the backfill and are 2.9 %, 2.8 %, 4.6 % and 4.4 % for Cases 6, 7, 11 and 12, respectively. Thus, the maximum gas saturation is only doubled by increasing the gas production rate in 1 order of magnitude.

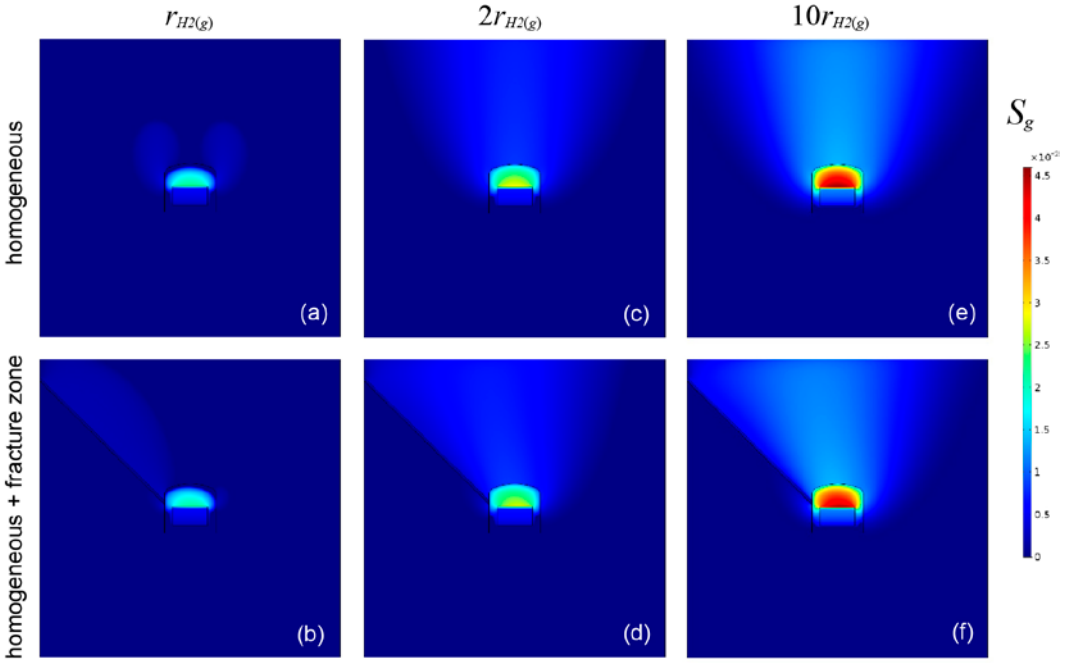

Figure 4-23. *Gas saturation at 100 years for (a) Case 1, (b) Case 2, (c) Case 6, (d) Case 7, (e) Case 11, (f) Case 12.*

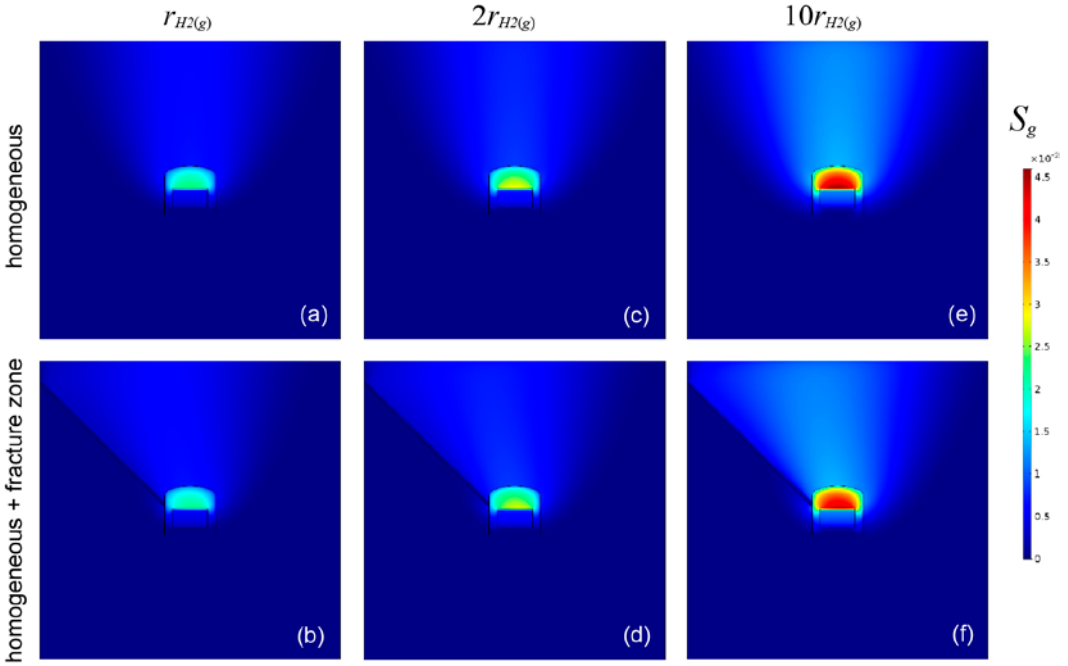

Figure 4-24. *Gas saturation at 1 000 years for (a) Case 1, (b) Case 2, (c) Case 6, (d) Case 7, (e) Case 11, (f) Case 12.*

The influence of gas generation rate (Equation (2-4)) on the average gas pressure and overpressure in the BHK vault when the host rock is homogeneous is presented in Figure 4-25. The effect of including a fracture zone is displayed in Figure 4-26. As shown in Figure 4-25a, the average gas pressure in the BHK vault increases about 1.0 bar when the hydrogen generation rate increases 1 order of magnitude (Case 11). Figure 4-25a shows that the maximum overpressure in the BHK vault increases in 0.2 and 0.8 bar, when the hydrogen generation rate increases 2 and 10 times, respectively. Moreover, the fracture zone contributes to reduce the pressure with about 0.5 bar (compare Figure 4-25a and Figure 4-26a). The effect of higher gas production rates on overpressures when the host rock includes a fracture zone (Cases 7 and 12) is almost the same of that displayed by the homogeneous rock models (Cases 6 and 11). This is because the difference in permeability of the fracture and the homogeneous rock is only about 3 orders of magnitude (see Section 4.1.2). Comparison of Figure 4-25b with Figure 4-26b confirms that the overpressure reduction due to the fracture zone is not significant when the rock is homogeneous.

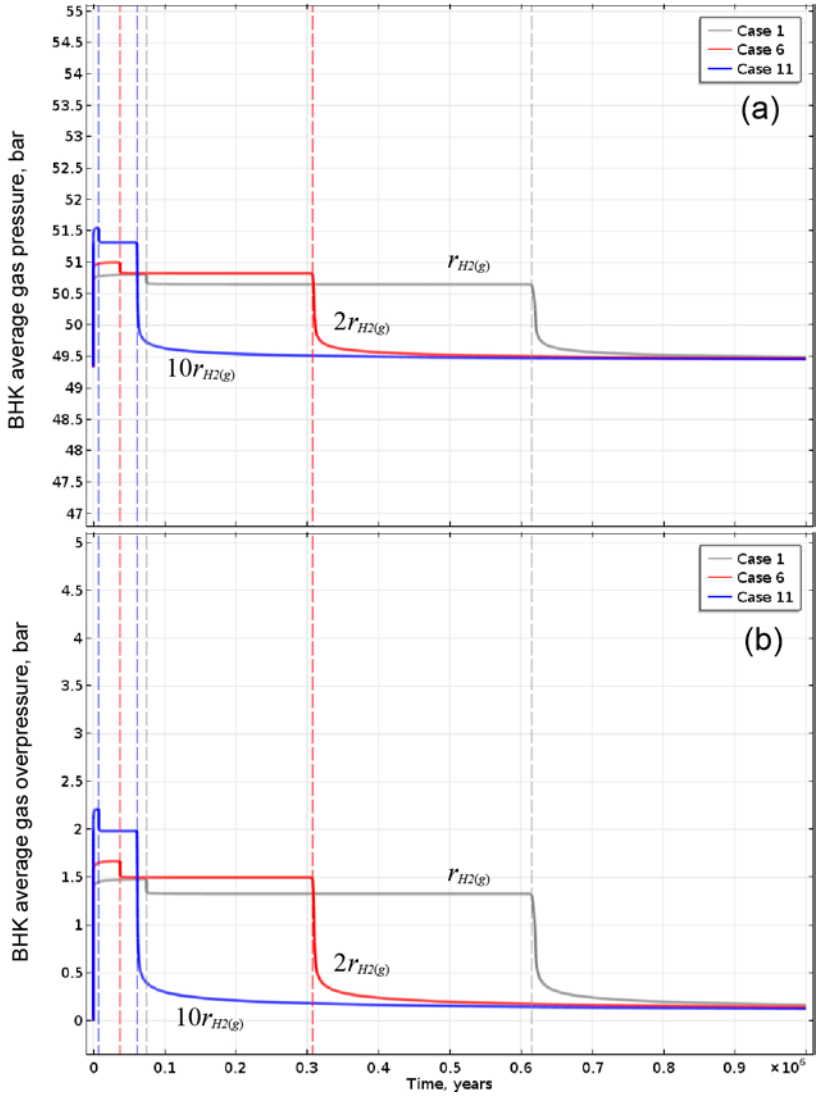

Figure 4-25. *Effect of the gas production rate on the evolution of (a) the average gas pressure and (b) overpressure, in the BHK, when the rock is homogeneous (vertical dashed lines denote the duration of the two corrosion regimes, for each gas production rate).*

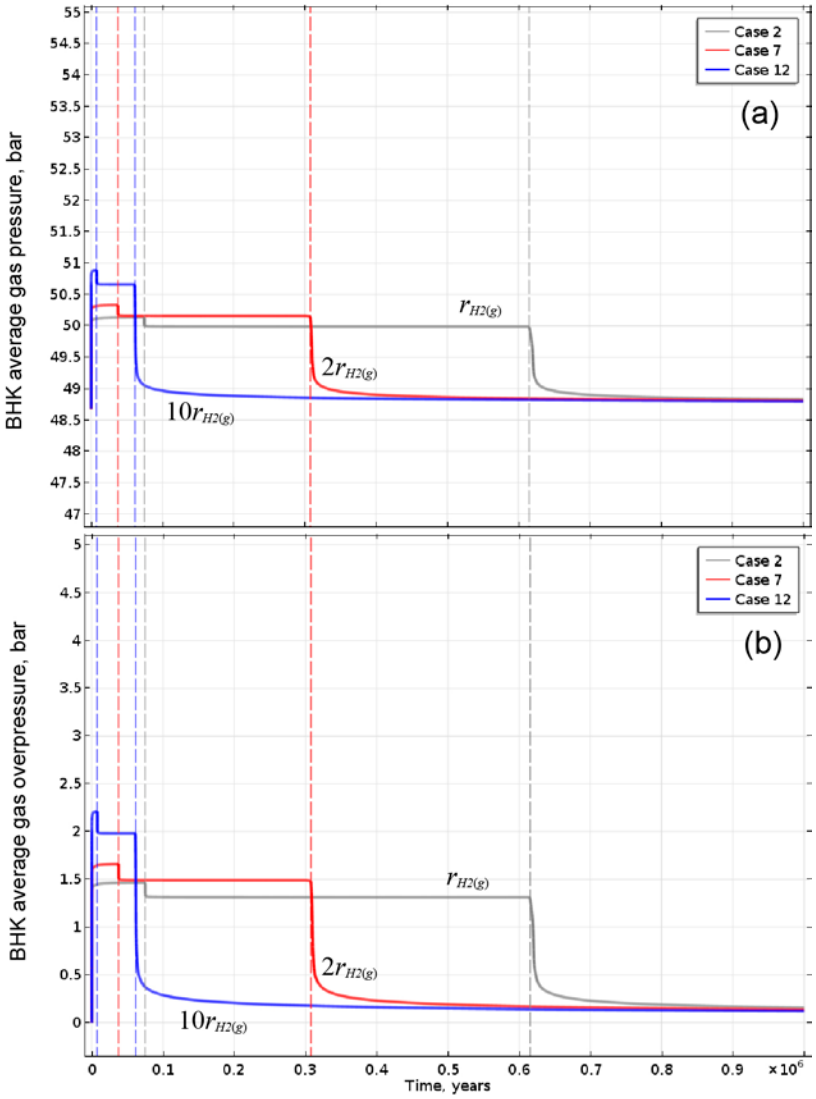

Figure 4-26. *Effect of the gas production rate on the evolution of (a) the average gas pressure and (b) overpressure, in the BHK, when the rock is homogeneous and include a fracture zone (vertical dashed lines denote the duration of the two corrosion regimes, for each gas production rate).*

4.2.2 Heterogeneous host rock

The influence of larger gas production on gas flow when the host rock is heterogeneous is analyzed by comparing the simulation Cases 8, 9, 10, 13, 14 and 15 (Table 4-3) with Cases 3, 4 and 5 (Table 4-1). Figure 4-27 to Figure 4-30 show the evolution of the gas saturation distributions during the first 1 000 years. When the rock is heterogeneous the evolution of the gas in the NF is similar for different hydrogen generation rates. Larger gas production rates speed up the gas release and flow through the rock, and increases the gas saturations during the period of maximum steel corrosion.

Gas flow in heterogeneous host rock is slower than in homogeneous host rock. As explained in Section 4.1.1, this because in Sections A and B of the host rock the permeability is lower than the permeability considered in the homogeneous rock model. As shown in Figure 4-27, even after 20 years the gas still is within the waste for double gas production rates (Cases 8, 9 and 10). Unlike in the homogeneous rock models, for very high gas production rates (Cases 13, 14 and 15) the gas does not fill the top backfill (Figure 4-27g, Figure 4-27h and Figure 4-27i).

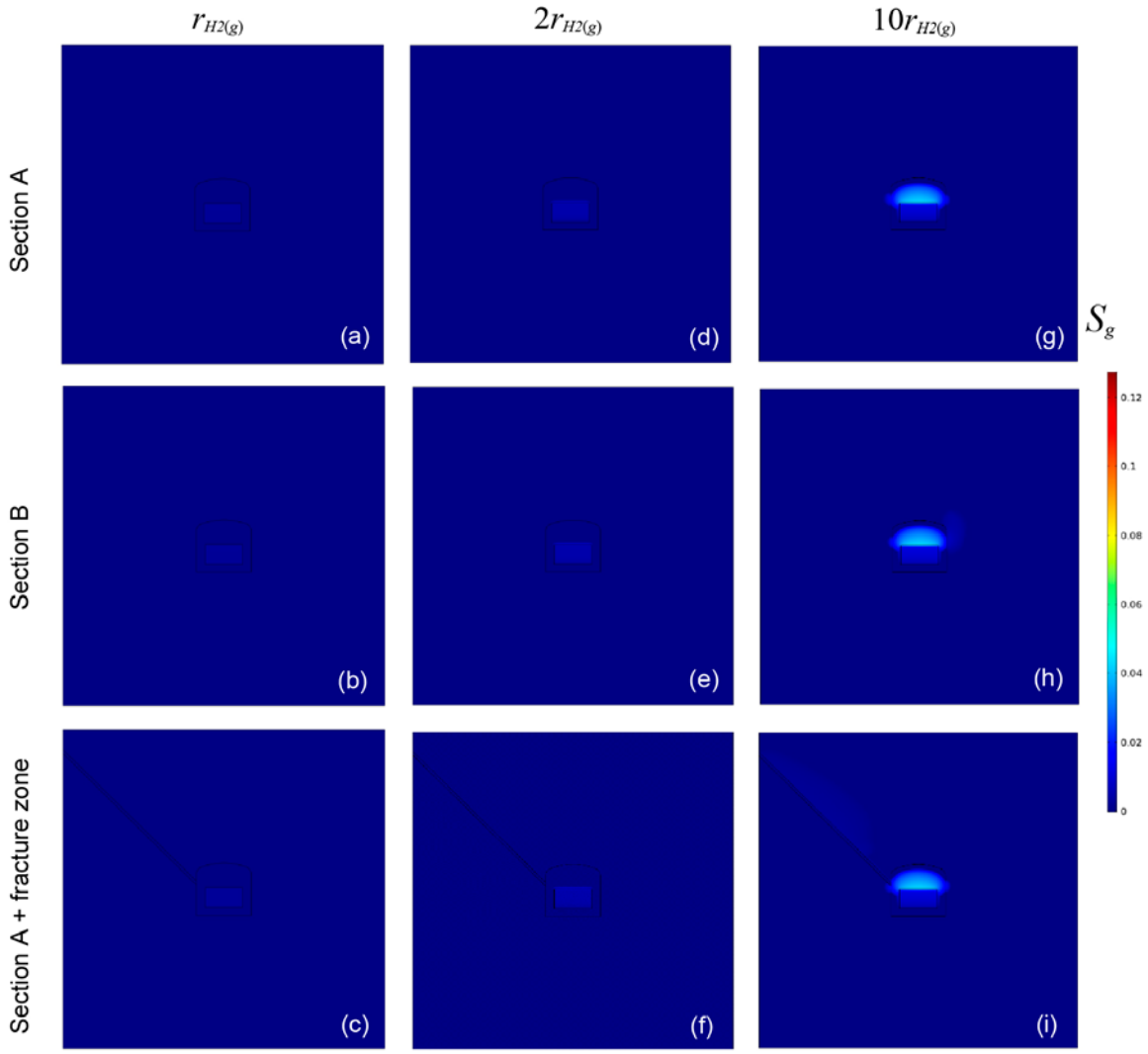

Figure 4-27. *Gas saturation at 20 years for (a) Case 3, (b) Case 4, (c) Case 5, (d) Case 8, (e) Case 9, (f) Case 10, (g) Case 13, (h) Case 14, (i) Case 15.*

For double gas production rates (Cases 8 and 9), the gas flow is still restricted mainly to the vault after 65 years (Figure 4-28d and Figure 4-28e). In Case 10, the fracture zone starts to play an important role for gas flow out from the vault (Figure 4-28f). Increasing the gas production rate by one order of magnitude promotes a faster gas flow. After 65 years, the gas has spread through a large zone around the vault, reaching the top boundary (see, e.g. Figure 4-28g). This is more evident in the Case 14 (Figure 4-28h), because the high permeability zone crossing the vault in Section B.

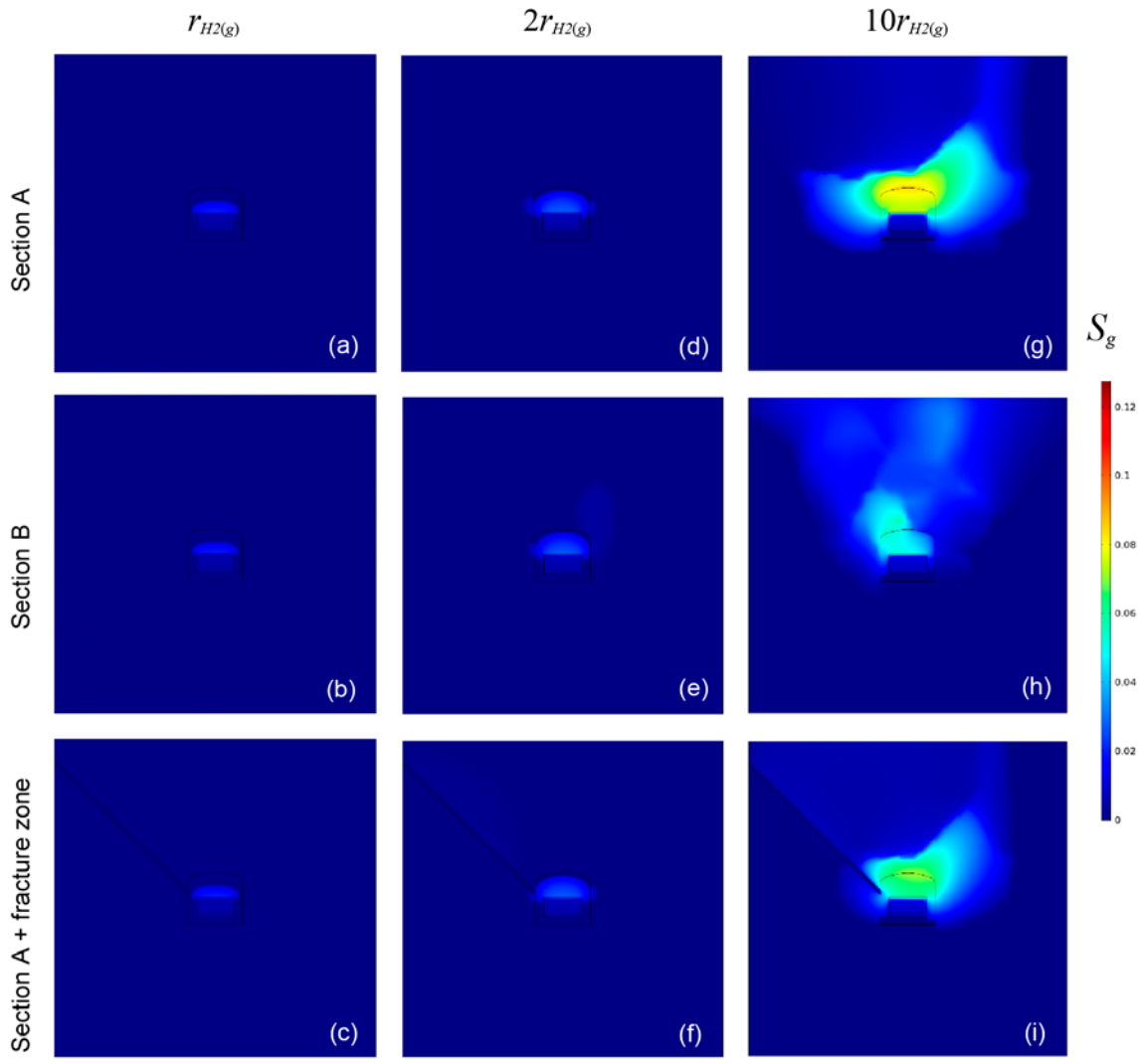

Figure 4-28. *Gas saturation at 65 years for (a) Case 3, (b) Case 4, (c) Case 5, (d) Case 8, (e) Case 9, (f) Case 10, (g) Case 13, (h) Case 14, (i) Case 15.*

Doubling the gas production rates (Cases 8 and 9) causes gas to flow out from the vault after 100 years. As shown in Figure 4-29d and Figure 4-29e, the gas saturation profiles are like those developed with the base gas production rate after 150 years (Cases 3 and 4, see Figure 4-5c and Figure 4-5d).

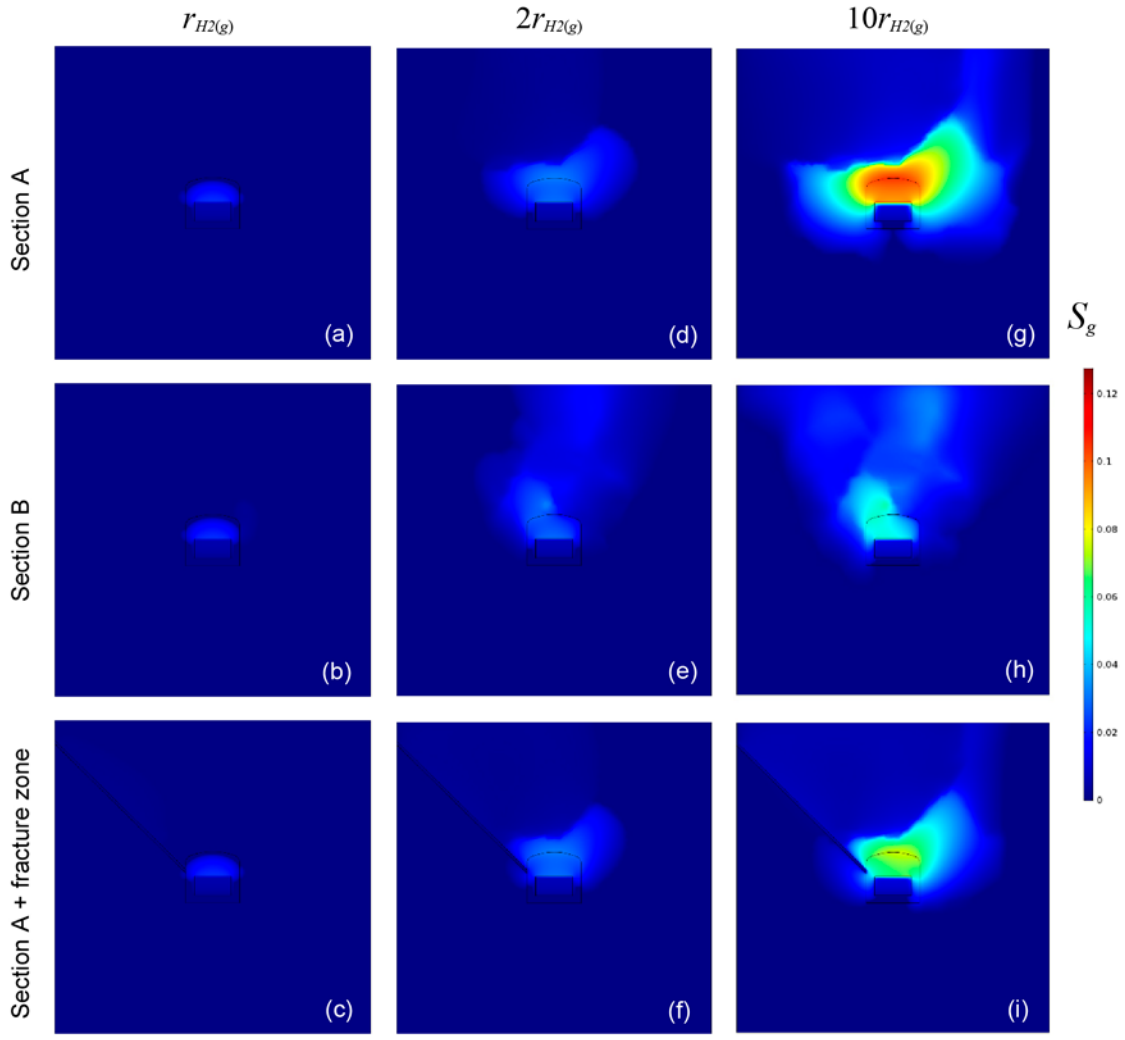

Figure 4-29. *Gas saturation at 100 years for (a) Case 3, (b) Case 4, (c) Case 5, (d) Case 8, (e) Case 9, (f) Case 10, (g) Case 13, (h) Case 14, (i) Case 15.*

Due to the presence of low permeability zones in the heterogeneous host rock, especially in Section A, the quasi-steady state is reached later, even for very high gas production rates (compare Figure 4-29g and Figure 4-30g). Increasing the gas production rate by 1 order of magnitude contributes to spread the gas laterally and downwards after 1 000 years (see Figure 4-30g, Figure 4-30h and Figure 4-30i). Nevertheless, although the gas saturations developed in the Case 13 are significantly higher than in the remaining cases, the gas does not reach the lateral boundaries after 1 000 years.

The maximum saturation of gas is about 8 %, 3.9 %, 5.1 %, 12.8 %, 5.7 % and 7.6 % for Cases 8, 9, 10, 13, 14 and 15, respectively (see, Figure 4-30). Thus, in heterogeneous low permeability rock (Section A), the maximum gas saturation increases 23 % and 100 % by increasing the gas production rate 2 and 10 times, respectively. These increases are about 22 % and 78 % for gas flow in highly heterogeneous host rock (Section B).

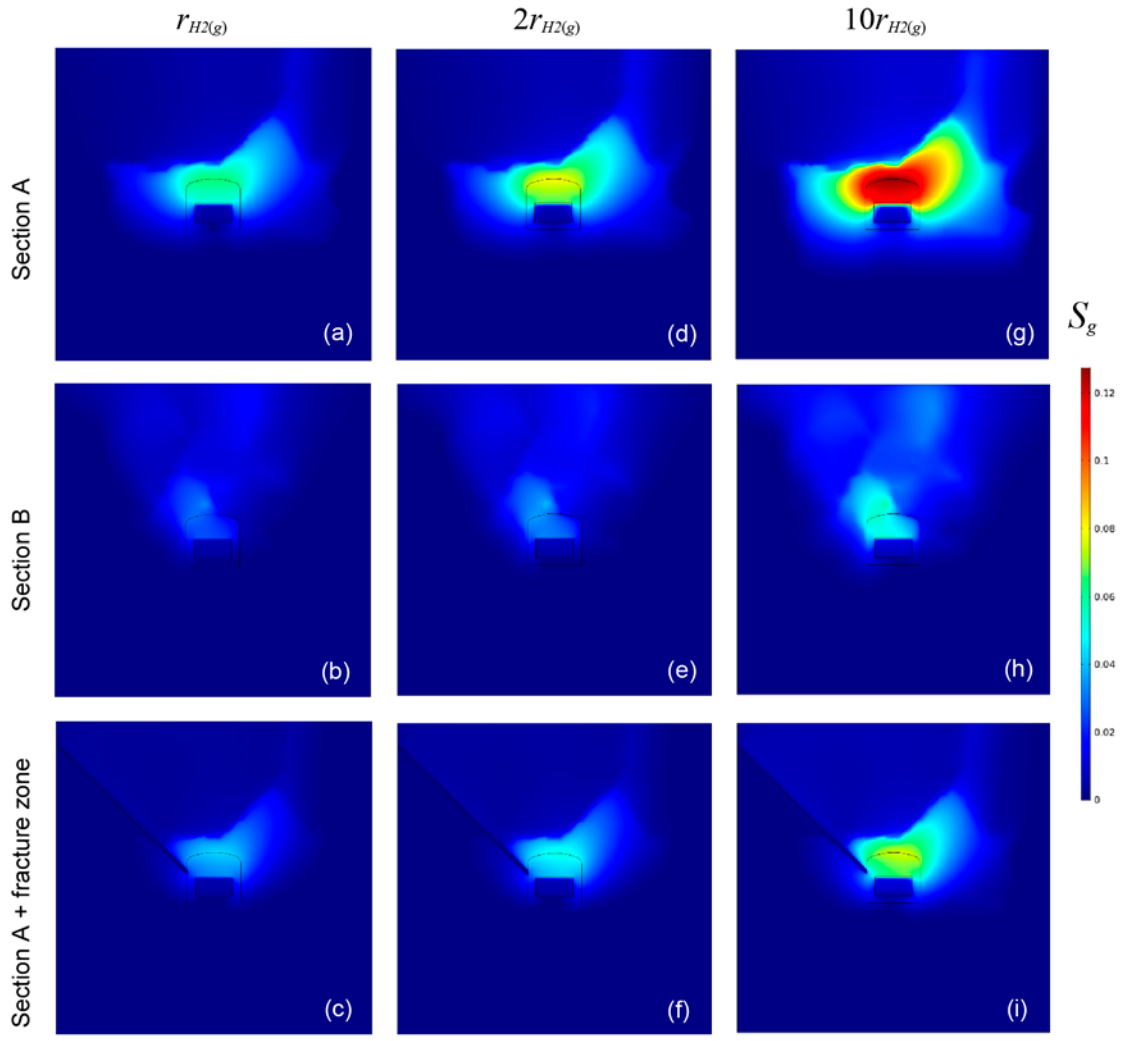

Figure 4-30. *Gas saturation at 1 000 years for (a) Case 3, (b) Case 4, (c) Case 5, (d) Case 8, (e) Case 9, (f) Case 10, (g) Case 13, (h) Case 14, (i) Case 15.*

Figure 4-31 and Figure 4-32 shows the impact of gas generation rate (Equation (2-4)) on the average gas pressure and overpressure in the BHK vault when the host rock is represented by Section A and B, respectively. When the BHK vault is enclosed by a rock of very low permeability, the average pressure increases by 0.5 and 2 bar when the hydrogen generation rate increases by a factor of 2 and 10, respectively (Figure 4-31a). For the heterogeneous rock model with high permeability (Section B), the average pressure in the BHK vault is close to that simulated with the homogeneous rock model (compare Figure 4-32 and Figure 4-25). This is because the average permeability of the rock adjacent to the vault is close to the permeability considered in the homogeneous rock model (Case 1).

The maximum overpressure ranges between 3.0 and 5.0 bar in the Section A model (Cases 3, 8 and 13, Figure 4-31b), and between 1.8 and 2.7 bar in the Section B model (Cases 4, 9 and 14, Figure 4-32b). In the Section A model, the maximum overpressure increases by 0.5 and 1.8 bar, when the hydrogen generation rate increases 2 and 10 times, respectively. For the Section B model, these increases are 0.3 and 1.0 bar.

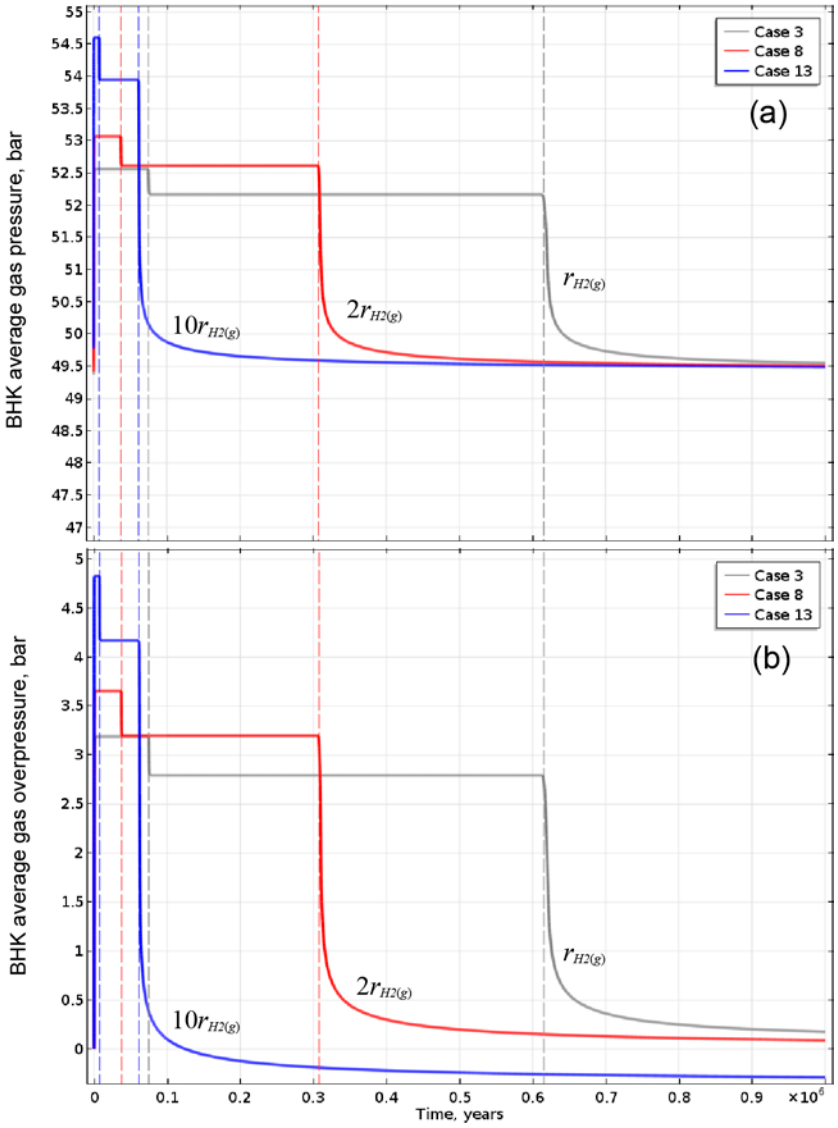

Figure 4-31. *Effect of the gas production rate on the evolution of (a) the average gas pressure and (b) overpressure, in the BHK, for heterogeneous rock (Section A). Vertical dashed lines denote the duration of the two corrosion regimes, for each gas production rate.*

Including a fracture zone within low permeability host rock (Section A, Cases 5, 10 and 15) contributes to reduce the average gas pressure in the vault in 2.0 bar (compare Figure 4-31a and Figure 4-33a). Overpressures decreases in about 0.9 to 1.2 bar. The impact of gas production rates is qualitatively the same as observed for Cases 3, 8 and 13.

In the long-term the initial pressures are recovered and overpressures tends to zero. The exception is the Case 13 where the average gas pressure in the vault drops below the initial average pressure after 125 000 years. This time is approximately 10 % of the total simulation time. Such a percentage is equal to the reduction in the corrosion time due to the increase by 1 order of magnitude in the production rates. Therefore, the pressures recovery simulated in Case 3 should be compared to the pressures recovery at 500 000 and 100 000 years, simulated in Case 8 and Case 13, respectively.

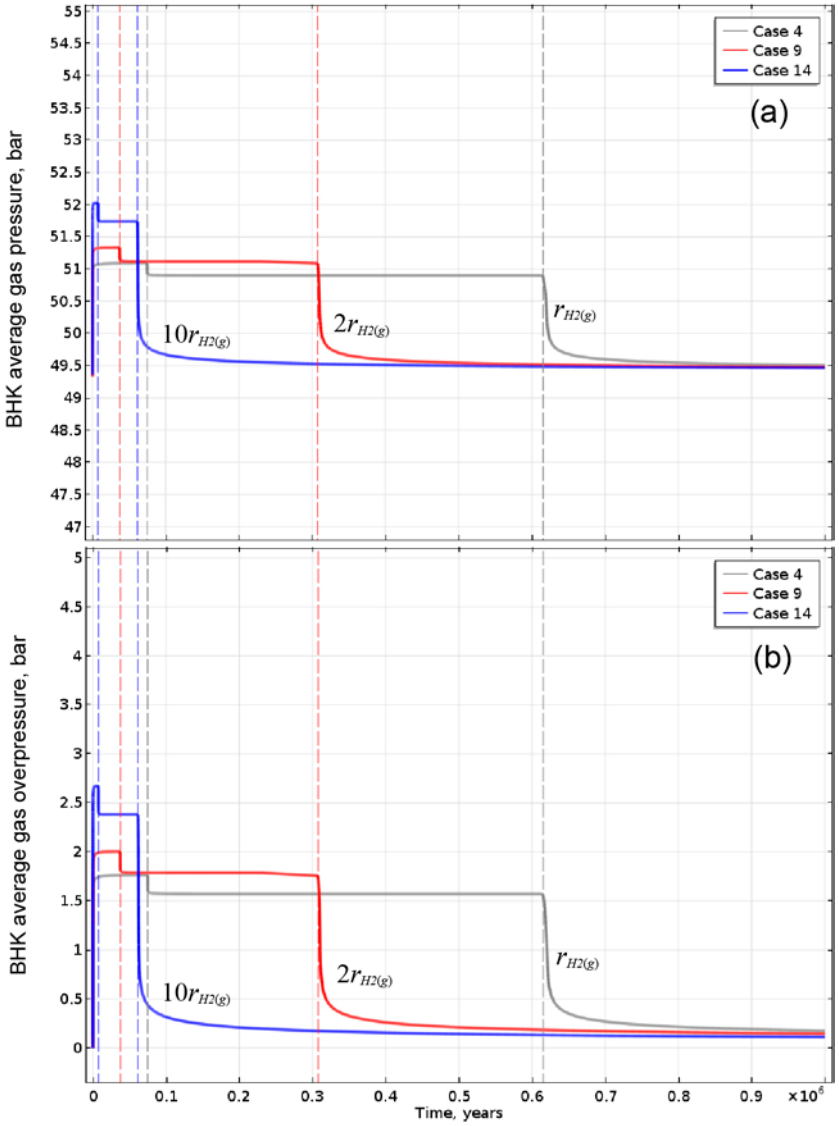

Figure 4-32. *Effect of the gas production rate on the evolution of (a) the average gas pressure and (b) overpressure, in the BHK, for heterogeneous rock (Section B). Vertical dashed lines denote the duration of the two corrosion regimes, for each gas production rate).*

This comparison is shown in Figure 4-34. Note that the initial gas pressure in the system is equal to the initial liquid pressure. The gas generation in the waste causes a gas pressure increase in the backfill with respect to the initial pressure. This gas overpressure is higher in the top backfill (see Figure 4-34). At the same time, due to the gas buoyancy the gas pressure decreases with respect to the initial pressure within the waste. This pressure reduction is about 0.05 bar after 1 000 000 years for Case 3, 0.09 bar after 500 000 years for Case 8, and 0.45 bar after 100 000 years for Case 13. Also, for a gas production rate of 1 order of magnitude higher (Case 13) larger zones of pressure reduction are developed in the backfill after 100 000 years (Figure 4-34c). Consequently, the average gas overpressure in the vault gets negative after steel corrosion has stopped (at about 125 000 years in Case 13).

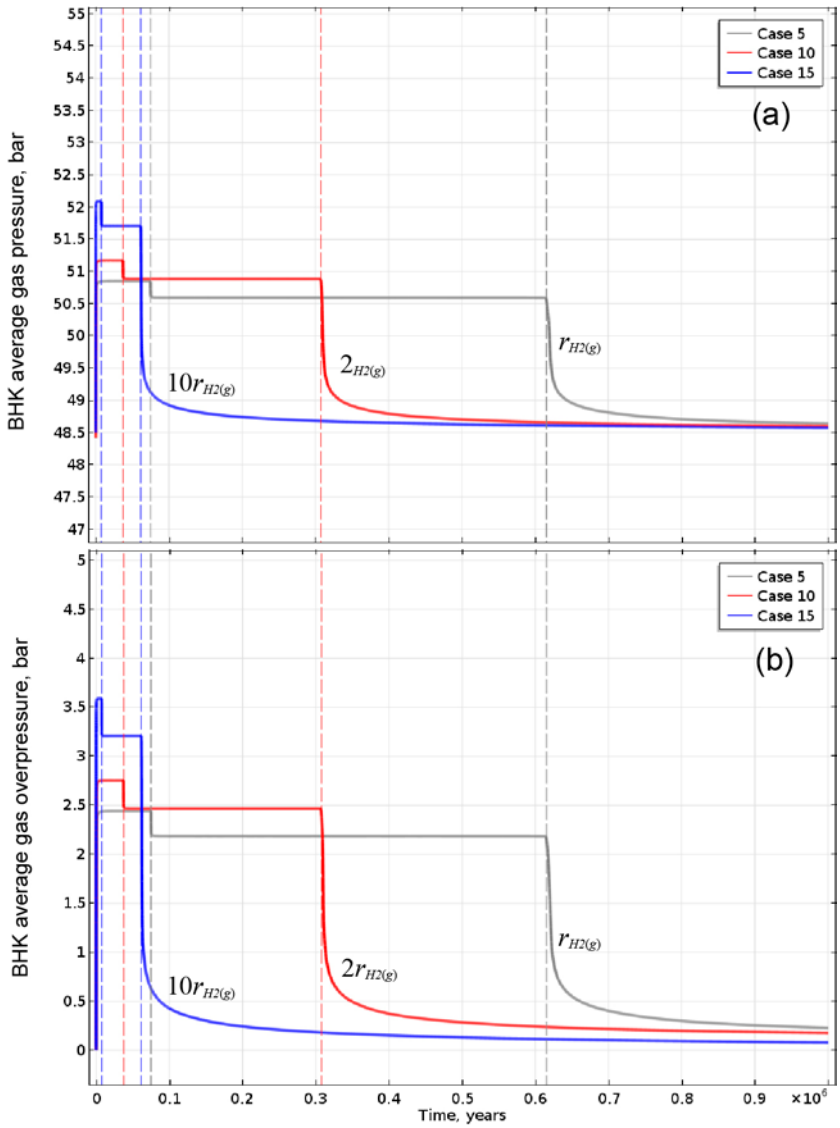

Figure 4-33. *Effect of the gas production rate on the evolution of (a) the average gas pressure and (b) overpressure, in the BHK, for heterogeneous rock (Section A) including a fracture zone. Vertical dashed lines denote the duration of the two corrosion regimes, for each gas production rate.*

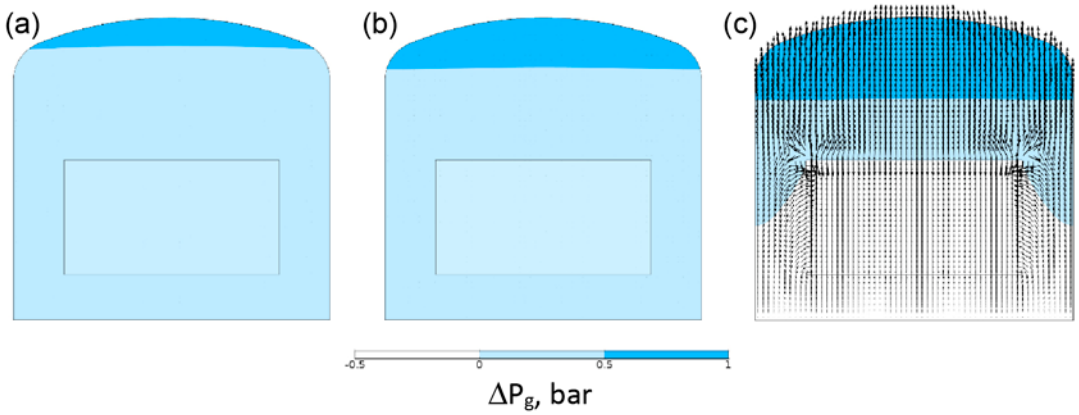

Figure 4-34. *Gas overpressure (ΔP_g) and velocity fields within the BHK vault at (a) 1 000 000 years for Case 3, (b) 500 000 years for Case 8, (c) 100 000 years for Case 13.*

4.2.3 Groundwater flow

Figure 4-35 shows the liquid pressure distributions obtained after 1 000 years when the host rock is homogeneous. The results show that increasing the gas production rate does not impact the groundwater pressure distributions, even when the host rock include a fracture zone. This also occurs when the host rock is heterogeneous, as shown in Figure 4-36a, b, d, e, g and h. It is concluded that although gas saturations of around 12 % can develop in the NF of the vault for a gas production rate of $10r_{H2(g)}$, water flow is close to quasi-stationary throughout the entire simulation.

Large gas production rates have an impact on water flow when the Section A includes a fracture zone (Cases 5, 10 and 15), as shown in Figure 4-36c, f and i. The results indicate that increasing the gas production rate by a factor of 10 causes an increase of approximately 42 % in the water flow through and around the fracture zone. Despite this increase, Figure 4-36 also shows that the water flow region obtained with a gas generation rate of $10r_{H2(g)}$ (Case 15) is smaller compared to Cases 5 and 10. This is because for a gas production rate 10 times higher, the gas flow through the fracture and around the vault in Section A is significantly higher, as shown in Figure 4-37.

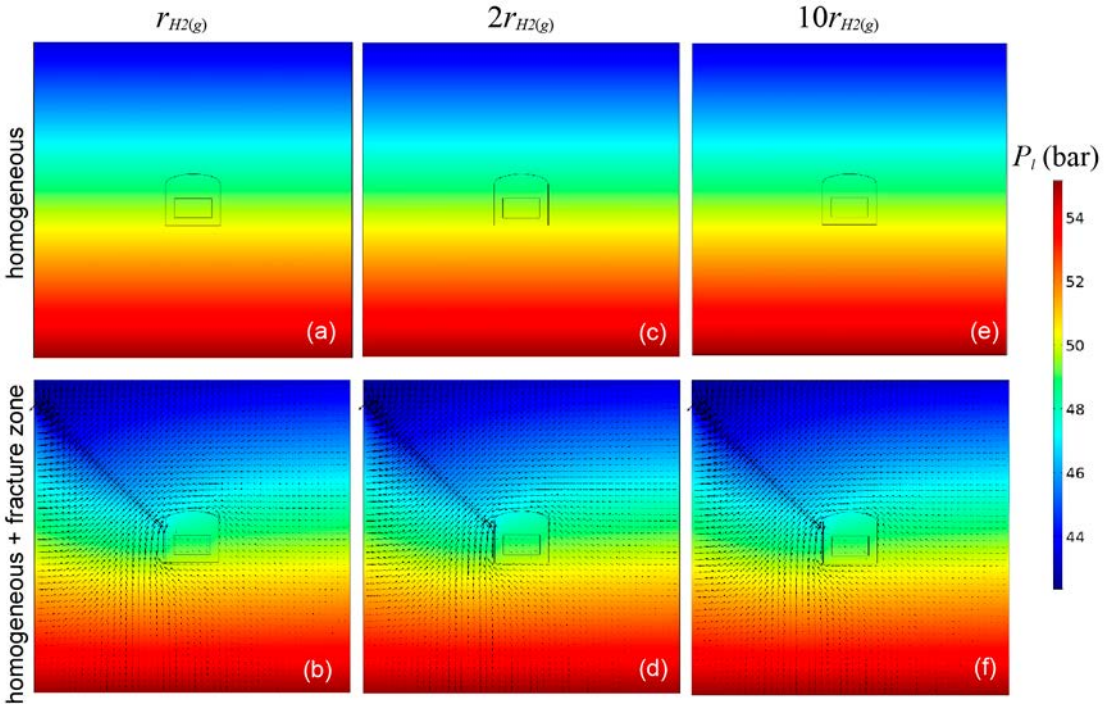

Figure 4-35. *Water pressure distributions obtained after 1 000 years with homogeneous host rock: (a) Case 1, (b) Case 2, (c) Case 6, (d) Case 7, (e) Case 11, (f) Case 12.*

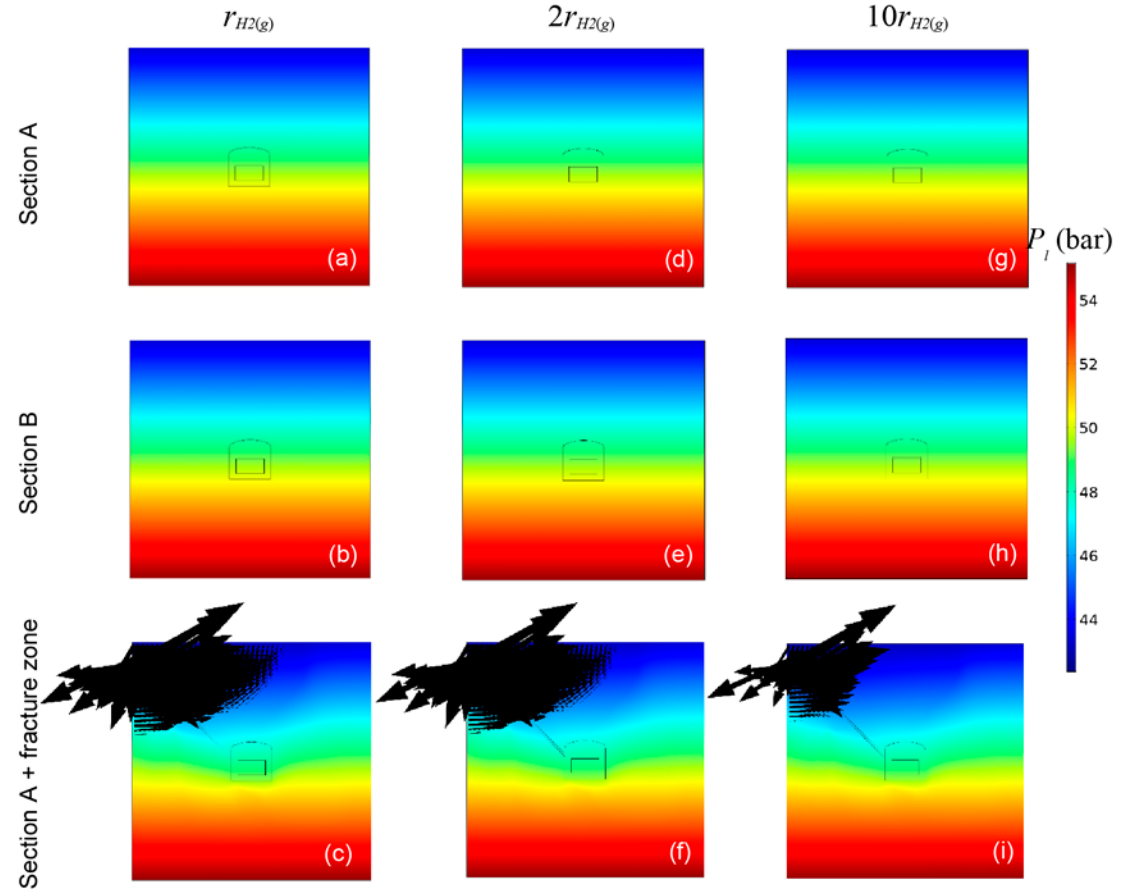

Figure 4-36. *Water pressure distributions obtained after 1 000 years with heterogeneous host rock: (a) Case 3, (b) Case 4, (c) Case 5, (d) Case 8, (e) Case 9, (f) Case 10, (g) Case 13, (h) Case 14, (i) Case 15.*

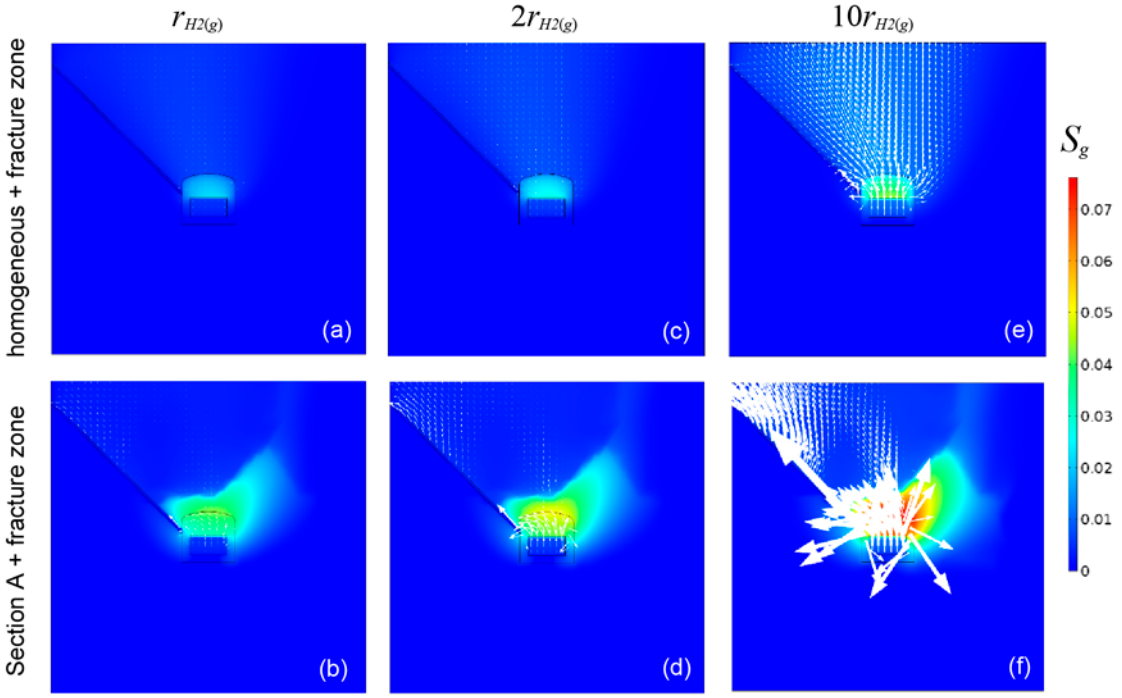

Figure 4-37. *Gas Darcy flux vector (black arrows) and gas saturation after 1 000 years in a rock including a fracture zone (a) Case 2, (b) Case 5, (c) Case 7, (d) Case 10, (e) Case 12, (f) Case 15.*

4.2.4 Inflow and outflow rates

The inflow and outflow rates to/from the BHK vault and the waste compartment (see Equation (4-2)) obtained for simulation Cases 6 to 15 are presented in Table 4-4. These flowrates have been calculated analogously to the flowrates calculated in Section 4.1.4.

Gas flowrates during the first 1 000 years can be compared, because during that time carbon and stainless steel corrodes simultaneously for the 3 gas production rates simulated. In general, both for the homogeneous and heterogeneous host rock models, the gas outflow rates from the vault and waste increase 2 and 10 times, when the gas production rates increase in the same factors. Nevertheless, for the heterogeneous rock model and Section A, increasing the gas production rates 2 and 10 times causes an increase of 2.4 and 15.7 times in the gas outflow rates from the waste. This is due to the enhanced internal flow caused by the gas recirculation flow cells explained in Section 4.1.1 (see Figure 4-13c).

Table 4-4. Influence of higher gas production rates on the inflow and outflow rates (m^3/year) of water (Q_l) and gas (Q_g) to/from the BHK vault and the waste compartment.

Time, years		BHK vault			Waste compartment		
		$Q_{l,in}$	$Q_{l,out}$	$Q_{g,out}$	$Q_{l,in}$	$Q_{l,out}$	$Q_{g,out}$
Case 6	0	0	0	0	0	0	0
	500	0	0	7.75E−03	0	0	7.95E−03
	1 000	0	0	7.76E−03	0	0	7.95E−03
	37 500	0	0	5.15E−03	0	0	4.37E−03
	74 900	0	0	4.20E−03	0	0	4.31E−03
	307 500	0	0	3.90E−03	0	0	4.00E−03
	500 000	0	0	2.42E−08	0	0	6.81E−09
	615 000	0	0	1.25E−08	0	0	3.62E−09
	1 000 000	0	0	3.93E−09	0	0	1.27E−09
Case 7	0	3.90	3.90	0	4.92E−01	4.92E−01	0
	500	3.23	3.40	8.10E−03	3.48E−01	3.47E−01	7.79E−03
	1 000	3.23	3.39	8.10E−03	3.47E−01	3.45E−01	7.79E−03
	37 500	3.26	3.42	5.21E−03	3.53E−01	3.50E−01	4.25E−03
	74 900	3.28	3.45	4.38E−03	3.56E−01	3.54E−01	4.22E−03
	307 500	3.28	3.45	4.23E−03	3.57E−01	3.54E−01	4.08E−03
	500 000	3.74	3.92	2.85E−08	4.70E−01	4.63E−01	7.43E−09
	615 000	3.74	3.93	1.45E−08	4.72E−01	4.65E−01	3.99E−09
	1 000 000	3.75	3.94	4.51E−09	4.76E−01	4.69E−01	2.42E−09
Case 8	0	0	0	0	0	0	0
	500	0	0	6.83E−03	0	0	6.00E−02
	1 000	0	0	7.33E−03	0	0	6.54E−02
	37 500	0	0	6.19E−03	0	0	5.33E−02
	74 900	0	0	3.98E−03	0	0	3.10E−02
	307 500	0	0	3.87E−03	0	0	3.00E−02
	500 000	0	0	7.38E−08	0	0	8.86E−09
	615 000	0	0	3.18E−08	0	0	4.49E−09
	1 000 000	0	0	7.78E−09	0	0	1.46E−09
Case 9	0	0	0	0	0	0	0
	500	0	0	7.64E−03	0	0	9.21E−03
	1 000	0	0	7.65E−03	0	0	9.22E−03
	37 500	0	0	5.43E−03	0	0	5.37E−03
	74 900	0	0	4.13E−03	0	0	4.93E−03
	307 500	0	0	3.79E−03	0	0	4.51E−03
	500 000	0	0	3.05E−08	0	0	7.31E−09
	615 000	0	0	1.53E−08	0	0	3.91E−09
	1 000 000	0	0	4.63E−09	0	0	1.30E−09

Time, years		BHK vault			Waste compartment		
		$Q_{l,in}$	$Q_{l,out}$	$Q_{g,out}$	$Q_{l,in}$	$Q_{l,out}$	$Q_{g,out}$
Case 10	0	4.80E−02	4.80E−02	0	3.87E−02	3.87E−02	0
	500	3.45E−02	3.67E−02	7.72E−03	3.01E−02	2.97E−02	1.42E−02
	1 000	3.41E−02	3.63E−02	7.76E−03	2.98E−02	2.94E−02	1.42E−02
	37 500	3.46E−02	3.52E−02	6.02E−03	3.02E−02	2.93E−02	9.64E−03
	74 900	3.51E−02	3.73E−02	4.18E−03	3.06E−02	3.01E−02	7.50E−03
	307 500	3.51E−02	3.74E−02	4.03E−03	3.07E−02	3.02E−02	7.20E−03
	500 000	4.32E−02	4.54E−02	7.79E−08	3.63E−02	3.56E−02	9.66E−09
	615 000	4.34E−02	4.56E−02	3.63E−08	3.64E−02	3.57E−02	5.34E−09
	1 000 000	4.36E−02	4.57E−02	9.59E−09	3.64E−02	3.58E−02	2.71E−09
Case 11	0	0	0	0	0	0	0
	100	0	0	3.84E−02	0	0	3.92E−02
	1 000	0	0	3.85E−02	0	0	3.92E−02
	7 500	0	0	3.09E−02	0	0	2.44E−02
	61 500	0	0	1.87E−02	0	0	1.90E−02
	74 900	0	0	1.23E−06	0	0	3.47E−07
	100 000	0	0	2.66E−07	0	0	7.44E−08
	615 000	0	0	5.34E−09	0	0	1.64E−09
	1 000 000	0	0	2.60E−09	0	0	9.33E−10
Case 12	0	3.89	3.89	0	4.88E−01	4.88E−01	0
	100	3.04	3.19	4.02E−02	3.12E−01	3.11E−01	3.84E−02
	1 000	3.02	3.17	4.03E−02	3.08E−01	3.05E−01	3.84E−02
	7 500	3.05	3.20	3.01E−02	3.16E−01	3.11E−01	2.32E−02
	61 500	3.10	3.26	2.12E−02	3.21E−01	3.19E−01	2.02E−02
	74 900	3.67	3.86	1.16E−06	4.51E−01	4.43E−01	3.13E−07
	100 000	3.70	3.89	2.81E−07	4.59E−01	4.51E−01	7.84E−08
	615 000	3.75	3.94	6.81E−09	4.75E−01	4.68E−01	1.97E−09
	1 000 000	3.76	3.94	3.09E−09	4.77E−01	4.70E−01	9.75E−10
Case 13	0	0	0	0	0	0	0
	100	0	0	2.19E−02	0	0	2.11E−01
	1 000	0	0	3.63E−02	0	0	4.33E−01
	7 500	0	0	3.03E−02	0	0	3.96E−01
	61 500	0	0	1.91E−02	0	0	2.04E−01
	74 900	0	0	6.65E−06	0	0	2.50E−06
	100 000	0	0	1.15E−06	0	0	1.63E−07
	615 000	0	0	1.14E−08	0	0	1.96E−09
	1 000 000	0	0	4.80E−09	0	0	1.02E−09
Case 14	0	0	0	0	0	0	0
	100	0	0	3.78E−02	0	0	4.67E−02
	1 000	0	0	3.80E−02	0	0	4.69E−02
	7 500	0	0	3.09E−02	0	0	3.30E−02
	61 500	0	0	1.97E−02	0	0	2.40E−02
	74 900	0	0	1.81E−06	0	0	4.41E−07
	100 000	0	0	3.62E−07	0	0	8.63E−08
	615 000	0	0	6.22E−09	0	0	1.67E−09
	1 000 000	0	0	3.01E−09	0	0	9.44E−10
Case 15	0	5.80E−02	5.80E−02	0	4.85E−02	4.85E−02	0
	100	3.14E−02	3.46E−02	3.74E−02	2.80E−02	2.78E−02	7.14E−02
	1 000	3.02E−02	3.22E−02	3.90E−02	2.67E−02	2.61E−02	7.40E−02
	7 500	3.33E−02	2.48E−02	3.28E−02	2.81E−02	2.51E−02	5.54E−02
	61 500	3.17E−02	3.37E−02	2.04E−02	2.80E−02	2.74E−02	3.84E−02
	74 900	4.16E−02	4.40E−02	4.13E−06	3.55E−02	3.47E−02	9.24E−07
	100 000	4.24E−02	4.47E−02	8.84E−07	3.59E−02	3.51E−02	1.30E−07
	615 000	4.35E−02	4.56E−02	1.50E−08	3.63E−02	3.57E−02	2.19E−09
	1 000 000	4.37E−02	4.57E−02	6.31E−09	3.64E−02	3.57E−02	1.06E−09

In general, during steel corrosion gas outflow rates from the waste are higher than outflow rates from the vault for all corrosion rates and heterogeneous host rock. After steel corrosion has stopped (after 615 000, 307 500 and 61 500 years for $r_{H2(g)}$, $2r_{H2(g)}$ and $10r_{H2(g)}$, respectively) gas outflow rates from the vault are higher than gas outflow rates from the waste, independently the rock type.

On the other hand, increasing the gas production rate does not impact the water flowrates through the vault and waste when the host rock does not include a fracture zone (Cases 6, 8, 9, 11, 13 and 14). In contrast, larger gas production rates reduce the water flowrates in the simulation Cases 7, 10, 12 and 15. On average, this reduction is about 3 % and 10 % when the gas production rate increases to $2r_{H2(g)}$ and $10r_{H2(g)}$, respectively. This is because for higher gas production rates, the fracture zone enhances the gas outflow from the vault, as explained in Section 4.2.3 (Figure 4-37). This increase in the gas flow around the vault and the fracture zone leads to a reduction in the water flow in this zone.

5 Results of FF models

As stated in the objectives, the NF two-phase flow models were extended to simulate several cases of hydrogen gas generation and migration in the FF. The results of the models describing the gas migration from the BHK vault up to the bedrock/regolith interface are presented in this section. The permeability and porosity heterogeneity of the host rock is accounted by simulating two cross-sections: the less permeable Section A and the more permeable and connected Section B (see Section 2.1.2). Two simulation cases assuming the gas generation rate considered in Silva et al. (2019) are analyzed in the Section 5.1. In the Section 5.2 the impact of larger gas production rates is evaluated. A summary of the models described in this section is shown in Table 5-1.

The analysis of results is done with the same variables used in the NF models. In addition, the following two variables are considered to evaluate the impact of gas migration at FF scale:

- Gas and water mass fluxes through the boundaries of the model (kg/m^2-s).
- Total gas mass flowrate through the regolith-bedrock interface (Q_{reg}) (i.e. the top boundary of the model) (kg/s), given by

$$Q_{reg} = \int_{\Sigma, \mathbf{J}_g \cdot \mathbf{n} < 0} \mathbf{J}_g \cdot \mathbf{n} \, dS \qquad \text{(Eq 5-1)}$$

In Equation (5-1), Σ is the top boundary of the system, and $\mathbf{J}_g$ (kg/m^2-s) is the "boundary flux" internal function of COMSOL.

Table 5-1. Cases to study gas migration in the FF of the BHK vault.

Case #	Cross-section	Gas production rate, kg/m^3-s	$t_{c,ss}$ (years)	$t_{c,cs}$ (years)
16	Section A	$r_{H2(g)}$	74 920	615 313
17	Section B			
18	Section A	$2r_{H2(g)}$	37 460	307 656.5
19	Section B			
20	Section A	$10r_{H2(g)}$	7 492	61 531.3
21	Section B			

5.1 FF heterogeneous host rock model

The flow of the gas released from the BHK towards the regolith-bedrock interface is analyzed in this section. Two heterogeneous host rock sections are studied: Section A, where the BHK vault is surrounded by a very low permeability zone (Case 16); and Section B that presents a high permeable zone crossing the vault (Case 17). The setup of these models is described in Section 2.6 and Section 3.1.3.

5.1.1 Gas flow behavior

The evolution of the gas saturation is shown in Figure 5-1 for Case 16 and in Figure 5-2 for Case 17. The low density of the hydrogen gas promotes its upwards migration, despite the water flow in the surroundings of the vault moves downwards (see Figure 2-17). The buoyancy forces drive the gas flow and no or little influence of the water flow can be appreciated. The gas accumulates in areas with lower rock permeability, e.g. around the vault and in the middle-left part of the domain in Case 16 (compare Figure 5-1 with Figure 2-17a).

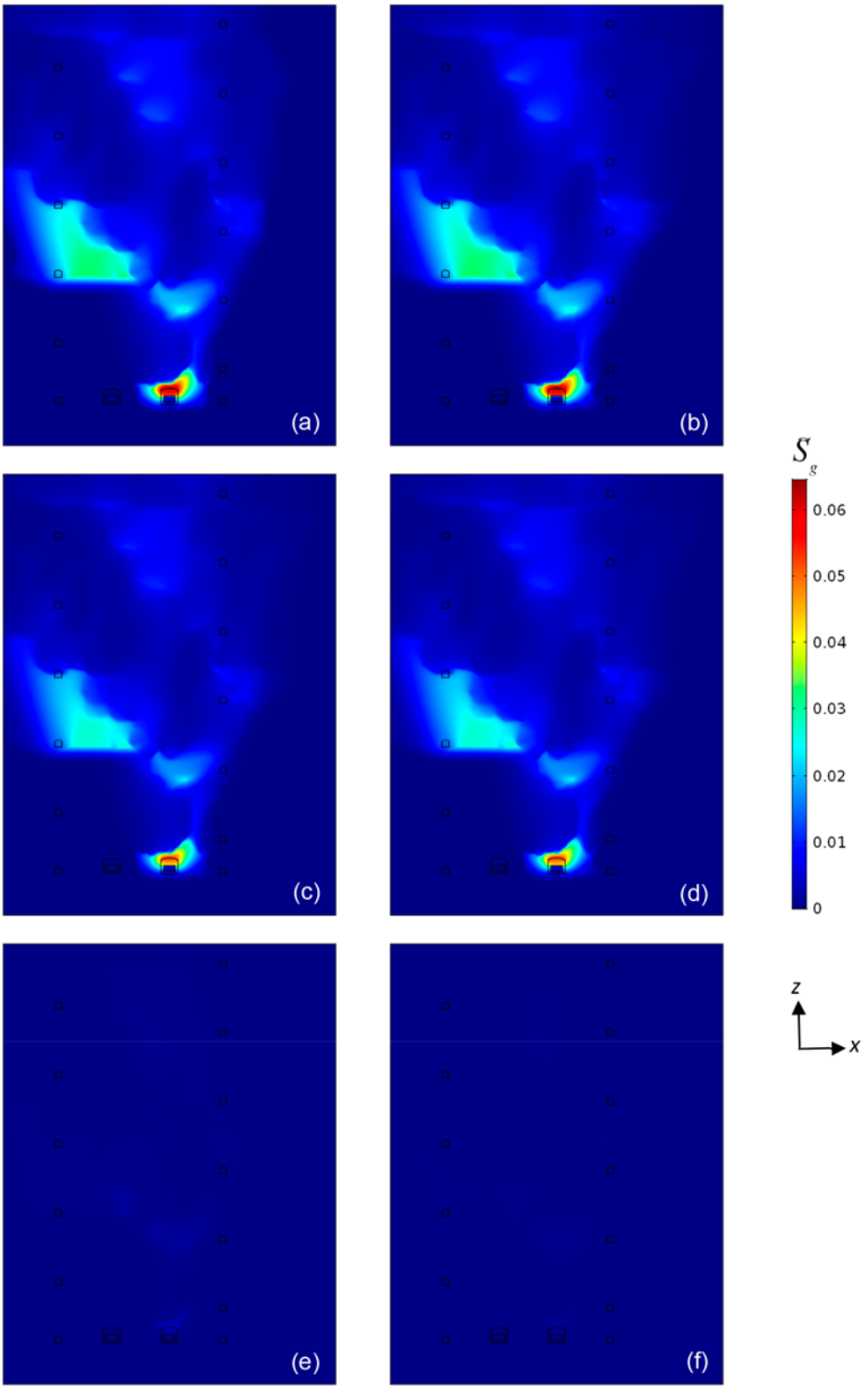

Figure 5-1. *Gas saturation for the Case 16 at (a) 1 000 years, (b) 70 000 years, (c) 80 000 years, (d) 600 000 years, (e) 700 000 years and (f) 1 000 000 years.*

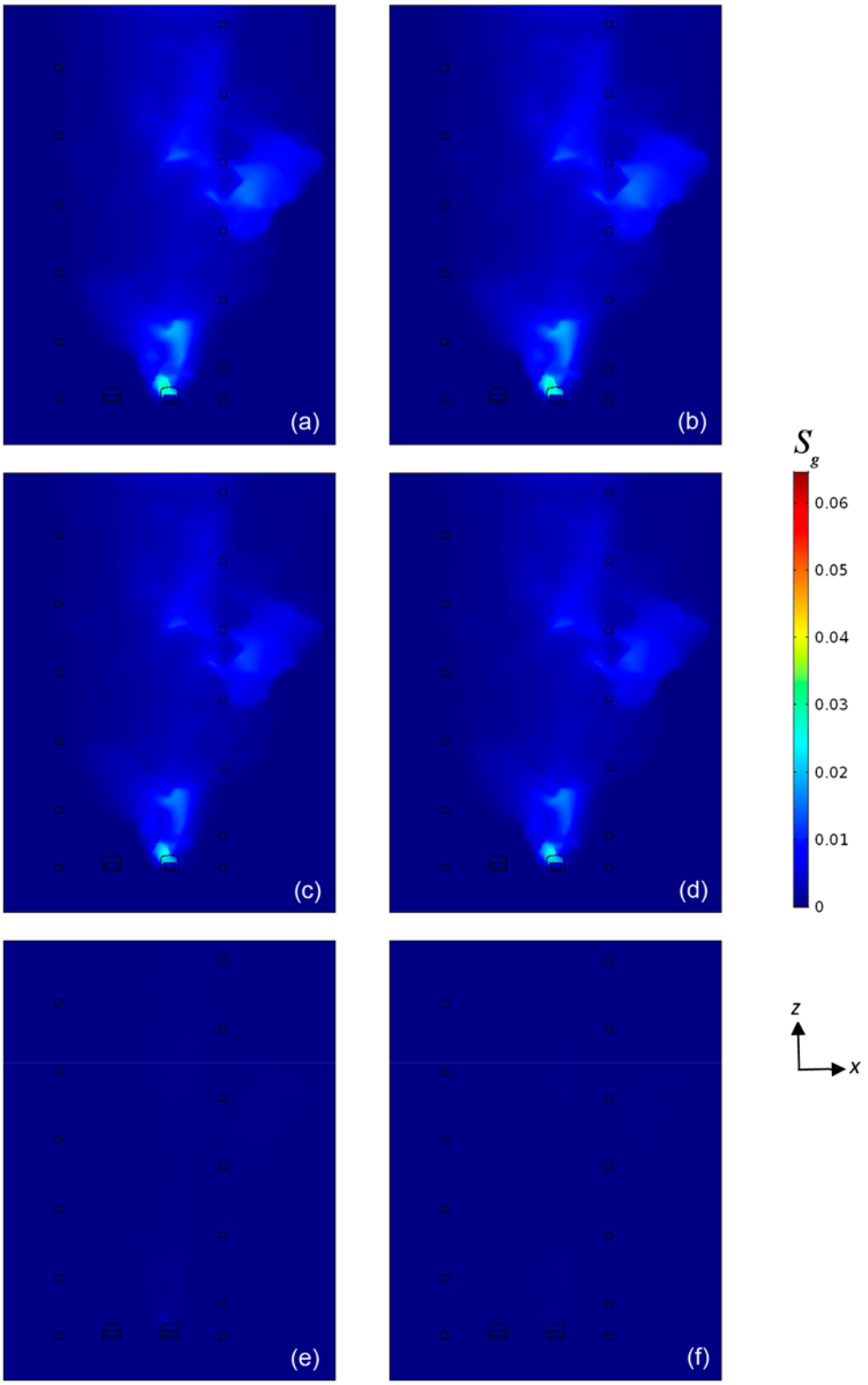

Figure 5-2. *Gas saturation for the Case 17 at (a) 1 000 years, (b) 70 000 years, (c) 80 000 years, (d) 600 000 years, (e) 700 000 years and (f) 1 000 000 years.*

The gas flows upwards preferentially through the highly permeable zones. When these zones are connected, the gas can migrate up to the regolith interface and leave the model domain at Darcy velocities of the order of 1.5×10^{-11} m/s. In contrast, if these highly permeable areas are separated by low permeable zones, the gas requires more time to reach the surface (Darcy velocities of 1 to 2 orders of magnitude lower). The size of the low permeable zones or the separation distance between highly permeable zones also impacts the gas migration dynamics. Consequently, low flow or stagnant zones with higher gas saturation are generated. Note that the location of the BHA vault and the access tunnels is shown in the figures. However, their hydraulic properties are not considered. Although the presence of highly permeable materials in the access tunnels would affect the gas migration, such effects cannot be captured by a 2D model.

The gas saturation distribution varies as function of the gas production regime. The maximum gas saturation occurs when the carbon steel and stainless steel corrode simultaneously (a and b in Figure 5-1 and Figure 5-2). The gas saturation distribution when only the carbon steel corrodes displays the same pattern, but with lower saturation levels (c and d in Figure 5-1 and Figure 5-2). Finally, when all the steel has been consumed and no gas is released from the BHK vault, the gas leaves the domain in about 10 000 years (see Figure 5-5 and Figure 5-6). In the very long-term, there is only a residual amount of gas in the domain (e and f in Figure 5-1 and Figure 5-2). The gas flow responds rapidly to the variations on the corrosion rate, arriving in about 1 000 years to a quasi-steady state for each gas generation rate. Therefore, little variations in the gas distribution is observed between 1 000 and 70 000 years, between 80 000 and 600 000 years and between 700 000 and 1 000 000 years.

Figure 5-1 and Figure 5-2 show the same range of gas saturations. Clearly, the accumulation of gas in the domain is higher in Case 16 than in Case 17. Case 16 has a maximum gas saturation of 6.5 % twice as large as Case 17 (3.3 %). When the production of gas is only due to the corrosion of carbon steel, the maximum saturations are 5.4 % and 2.8 %, respectively. The host rock in Section B (Case 17) presents a much higher connectivity between permeable zones (see Figure 2-17b). This causes a faster and more direct migration of gas towards the surface and lower retention of hydrogen in the system (compare Figure 5-1e and Figure 5-2a).

5.1.2 Gas fluxes at the regolith/bedrock interface

Besides evaluating the gas saturation distributions, gas flow behavior can also be analyzed by inspecting the gas streamlines crossing the top and lateral boundaries of the BHK (Figure 5-3). In the models, less than a 0.15 % of the gas leaves through the lateral boundaries. The streamlines density increases in areas where the gas flow is higher (i.e. the permeability of the rock is higher). In the heterogeneous Section B, there is a relatively direct pathway for the hydrogen towards the surface (see Figure 5-3b, d and f). In contrast, the low connectivity of the permeable zones in Section A leads to an expansion of the streamlines towards both sides of the vault. The distribution of gas streamlines reaching the regolith/bedrock interface in the Case 16 is broader than in Case 17.

The gas flux through the regolith/bedrock interface is directly linked to the gas flow streamlines. As shown in Figure 5-4, in Case 16 hydrogen is more dispersed at the regolith/bedrock interface than in Case 17. The gas pathways towards the surface are relatively straight in Case 17. The gas flux at the regolith-bedrock interface follows a unimodal distribution with its maximum located above the BHK vault. In the less connected Section A there is a bimodal gas flux distribution at the top boundary. One of the peaks is located above the BHK vault and the other above the BHA vault. Note that streamlines are uniformly distributed across the BHK vault. They only give information about the pathways followed by the gas released from the vault. The density of the gas streamlines is not directly correlated with the mass of gas or the magnitude of gas fluxes. For instance, the area with a high density of streamlines at the left side of vault in Case 17 is not correlated with a peak in the hydrogen flux at the regolith/bedrock interface. Nevertheless, Figure 5-4 suggests that a relationship exists between the hydrogen flux at the regolith/bedrock interface and the rock permeability field that is just below this boundary. The unimodal distribution of hydrogen flux obtained in Case 17 is associated with a more uniform distribution of permeability at the top of the host rock (Figure 5-4 right). In contrast, the first 150 m of Section A include a less permeable zone (Figure 5-4 bottom left). The location of this zone coincides with the valley between the peaks displayed by the hydrogen flux profile (Figure 5-4 top left).

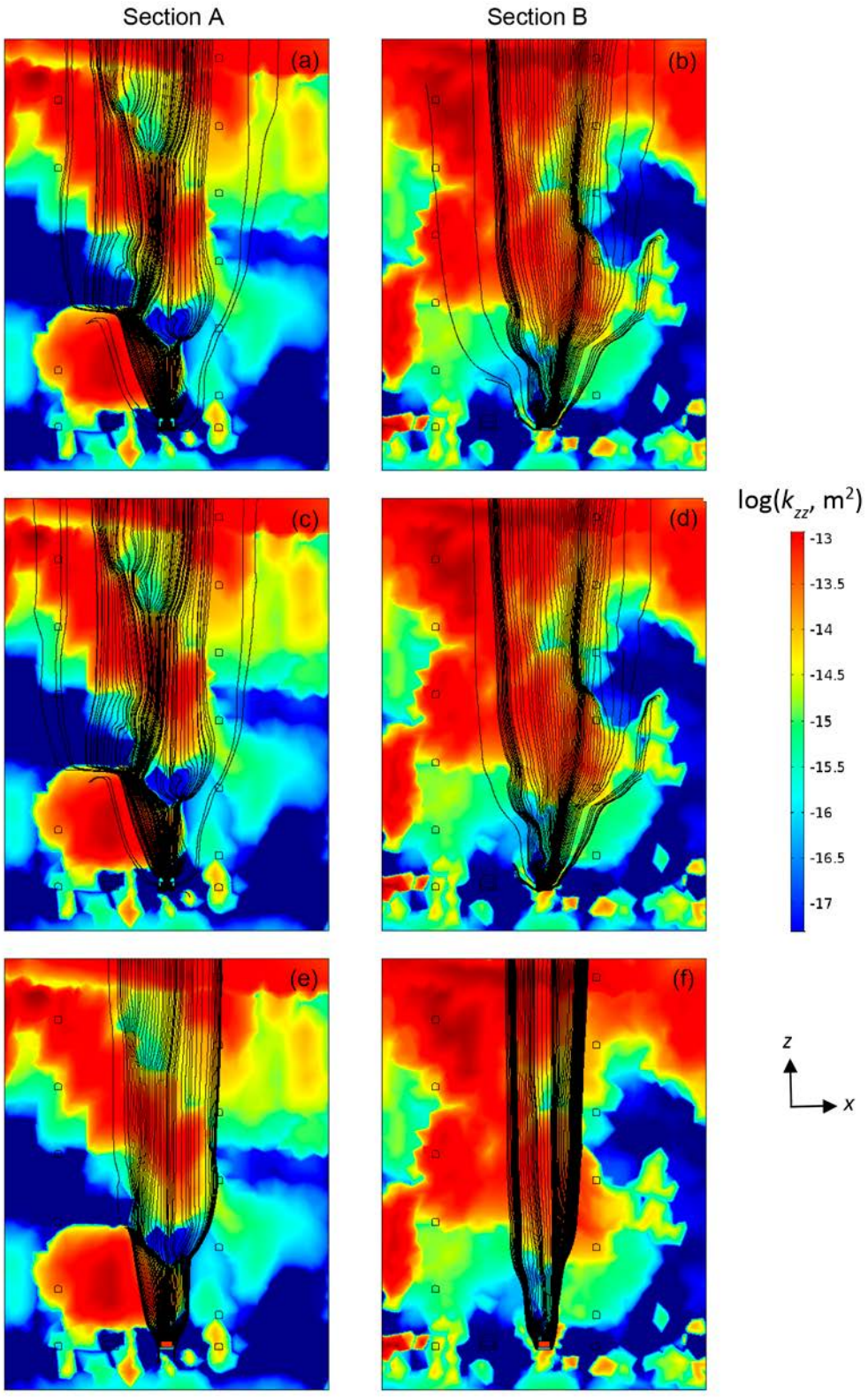

Figure 5-3. *Gas streamlines crossing the upper and lateral boundaries of the BHK for the Case 16 (left) and Case 17 (right) at (a, b) 70 000 years, (c, d) 100 000 years, (e, f) 800 000 years. Vertical permeability is included as reference.*

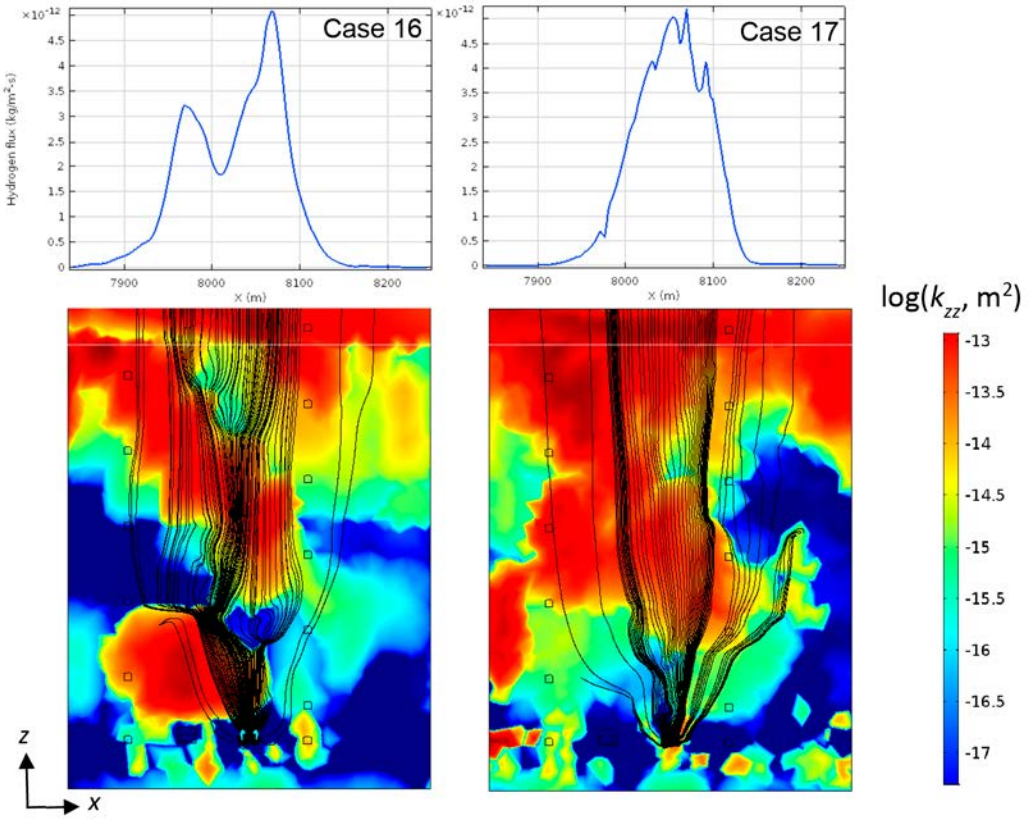

Figure 5-4. *Hydrogen gas flux through the regolith/bedrock interface (top) and gas streamlines crossing the top and lateral boundaries (bottom) at 70 000 years. Vertical permeability is included in the streamlines plot as reference.*

The shape of the gas flux distribution across the bedrock/regolith interface approximately the same for the entire simulation (Figure 5-5). The hydrogen flux is controlled by the gas production rate and the rock permeability distribution. Initially, the gas flux increases to a maximum that is maintained until the exhaustion of the stainless steel (a and b in Figure 5-5). Because the rock permeability in Section B is higher and more connected than in Section A, the hydrogen flux increases faster in Case 17 than in Case 16. The maximum hydrogen flux (5.1×10^{-12} kg/m^2-s) is almost equal in both models. Then, the hydrogen flux decreases around a 45 % (until 2.8×10^{-12} kg/m^2-s) (c and d in Figure 5-5). This value remains constant until the total depletion of the steel (615 313 years), when the hydrogen flux decreases again, being almost negligible in the long-term. Note that the hydrogen flux decrease after the complete corrosion of stainless steel is proportional to the corresponding reduction in the gas production rate (see Equation (2-4), Section 2.1.5).

The evolution of the total hydrogen flux through the regolith-bedrock interface (Equation (5-1)) is also similar in both cases (Figure 5-6). The amount of gas leaving the domain depends mainly on the gas production rates. It has a maximum of 5.1×10^{-12} kg/s during the simultaneous corrosion of carbon and stainless steel. This maximum decreases to 2.75×10^{-12} kg/s during the gas production due to carbon steel corrosion. In both Case 16 and Case 17 the response of the total hydrogen flux to the variations of the gas generation rate is fast. This is because the whole system rapidly responds to the new rate, achieving a new steady state. The only difference between the models is the velocity of the response to the gas generation rate variations. The time needed to achieve the plateau of maximum hydrogen flux is larger (about 2 000 years) in Case 16 than in Case 17 (about 800 years). Similarly, the decrease in the gas flow towards the regolith has a small delay in the Case 16. This is due to the poor connectivity of the highly permeable zones in Section A. These differences in the gas break-through at the regolith/bedrock interface cause a larger amount of gas to leave the system in Case 17 than in Case 16. This is consistent with the results displayed by the gas saturation distributions, which suggest that Section A retains more gas in the long-term.

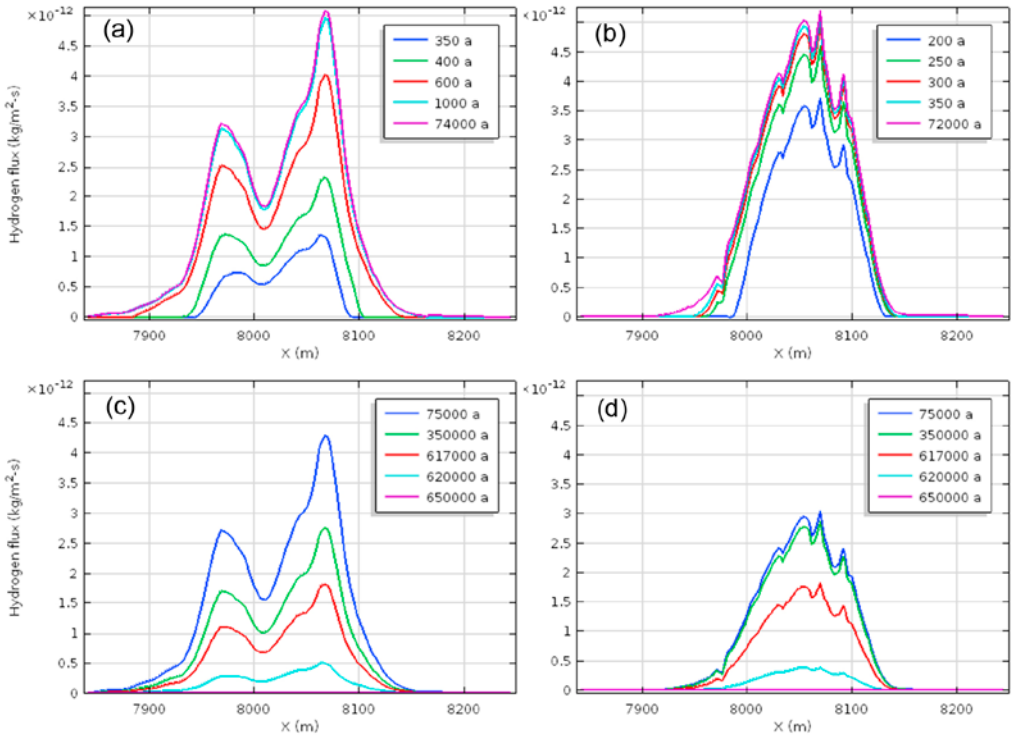

Figure 5-5. *Hydrogen gas flux through the regolith/bedrock interface for the Case 16 (a, c) and Case 17 (b, d). Plots on top correspond to the period of simultaneous corrosion of carbon and stainless steel. Bottom plots are for the periods of carbon steel corrosion and after the complete steel corrosion.*

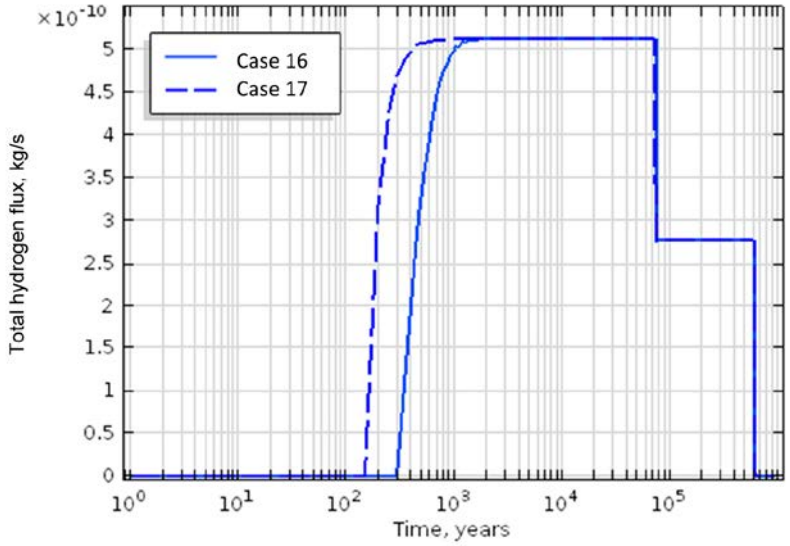

Figure 5-6. *Evolution of the total hydrogen gas flux at the regolith/bedrock interface. Note the logarithmic scale in the x axis.*

5.2 Influence of larger hydrogen gas production

The effect of larger gas production rates on the gas and water flow and their distributions is analyzed in this section. The amount of steel in the waste is assumed constant but the corrosion rate is increased by a factor of 2 and 10. This leads to higher gas generation volumes in a shorter period (see Section 2.1.2). The complete corrosion of stainless-steel occurs, then, at 37 460 and 7 492 years for a twice and ten times higher corrosion rate, respectively. Similarly, the total corrosion of carbon steel takes place after 307 656.5 and 61 531.3 years, respectively.

The resultant higher gas generation rates are studied for both, Section A and B. These leads to a set of 4 simulation cases (Table 5-1). Simulation Cases 18 and 20 were run with the less permeable Section A and Cases 19 and 21 with the more connected Section B. The gas generation rate at Cases 18 and 19 is twice higher and at Cases 20 and 21 is 10 times higher than in Cases 16 and 17. The setups of these models are described in Section 2.6 and Section 3.1.3.

5.2.1 Gas flow behavior

The gas saturation distributions simulated with higher gas generation rates display a behavior similar to that obtained with a rate of $r_{Hg(g)}$ (see Equation (2-4) and Section 2.1.5). Gas accumulates in the same areas of low permeability (Figure 5-7 and Figure 5-8). The amount of gas in the system and the gas saturation depend on the rate of gas production. The maximum gas saturation occurs during the simultaneous corrosion of stainless and carbon steel. This maximum is maintained until the stainless steel is exhausted (37 460 years and 7 492 years for a twice and ten times higher gas production rate, respectively).

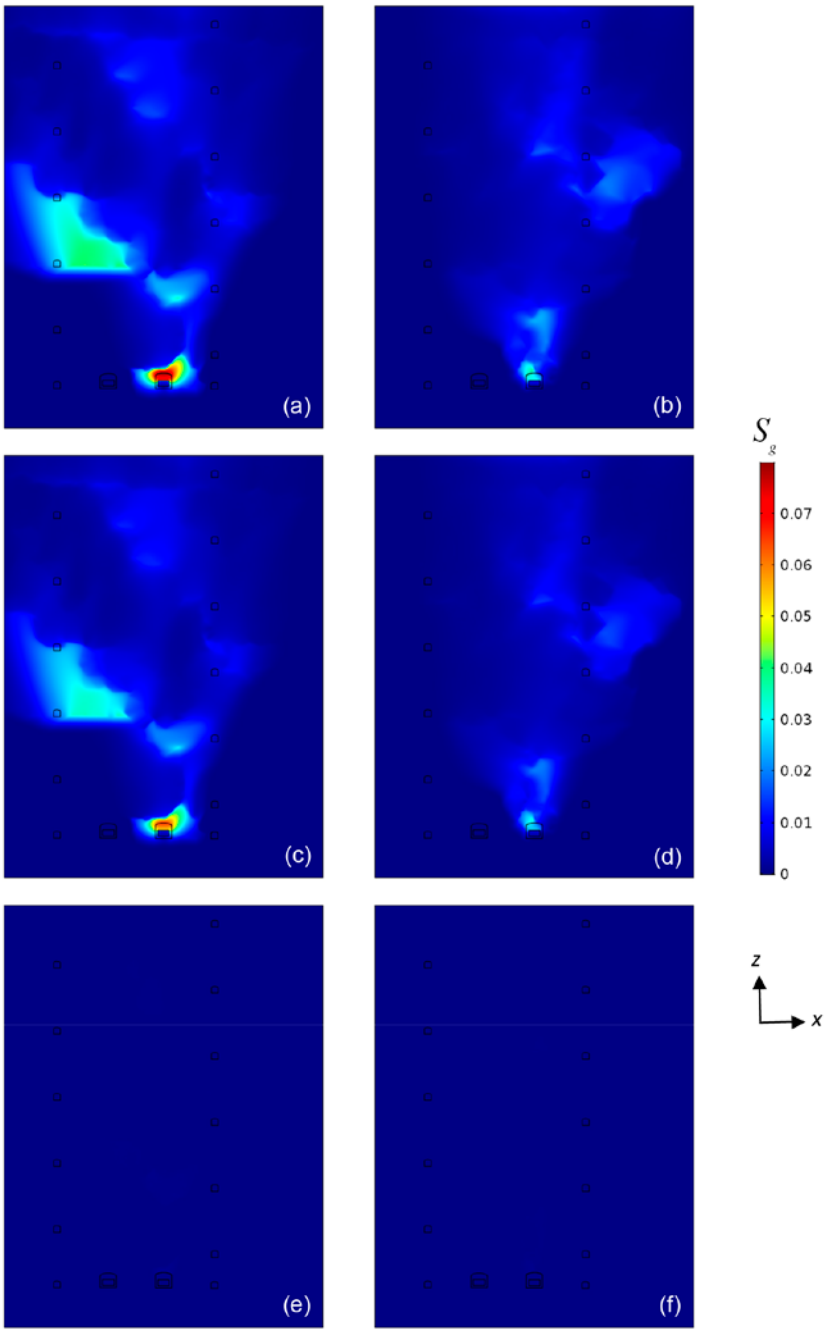

Figure 5-7. *Gas saturation for a gas production rate of $2r_{H2(g)}$ in the Case 18 (left) and Case 19 (right) at (a, b) 37 000 years, (c, d) 300 000 years, (e, f) 1 000 000 years.*

During the gas production period associated with carbon steel corrosion, the maximum gas saturation decreases around 85 %. In the long-term, when no gas is generated from the waste, the gas within the domain is almost negligible.

Figure 5-9a shows the maximum gas saturation in the domain as a function of the ratio between the gas generation rate and the rate considered by Silva et al. (2019). For all the gas production rates, the maximum gas saturation found in the simulation cases with Section B is half of the one in cases with Section A (Figure 5-9a). This is due to the larger connectivity of the highly permeable areas in Section B that cause a faster gas migration to the surface and a lower gas accumulation.

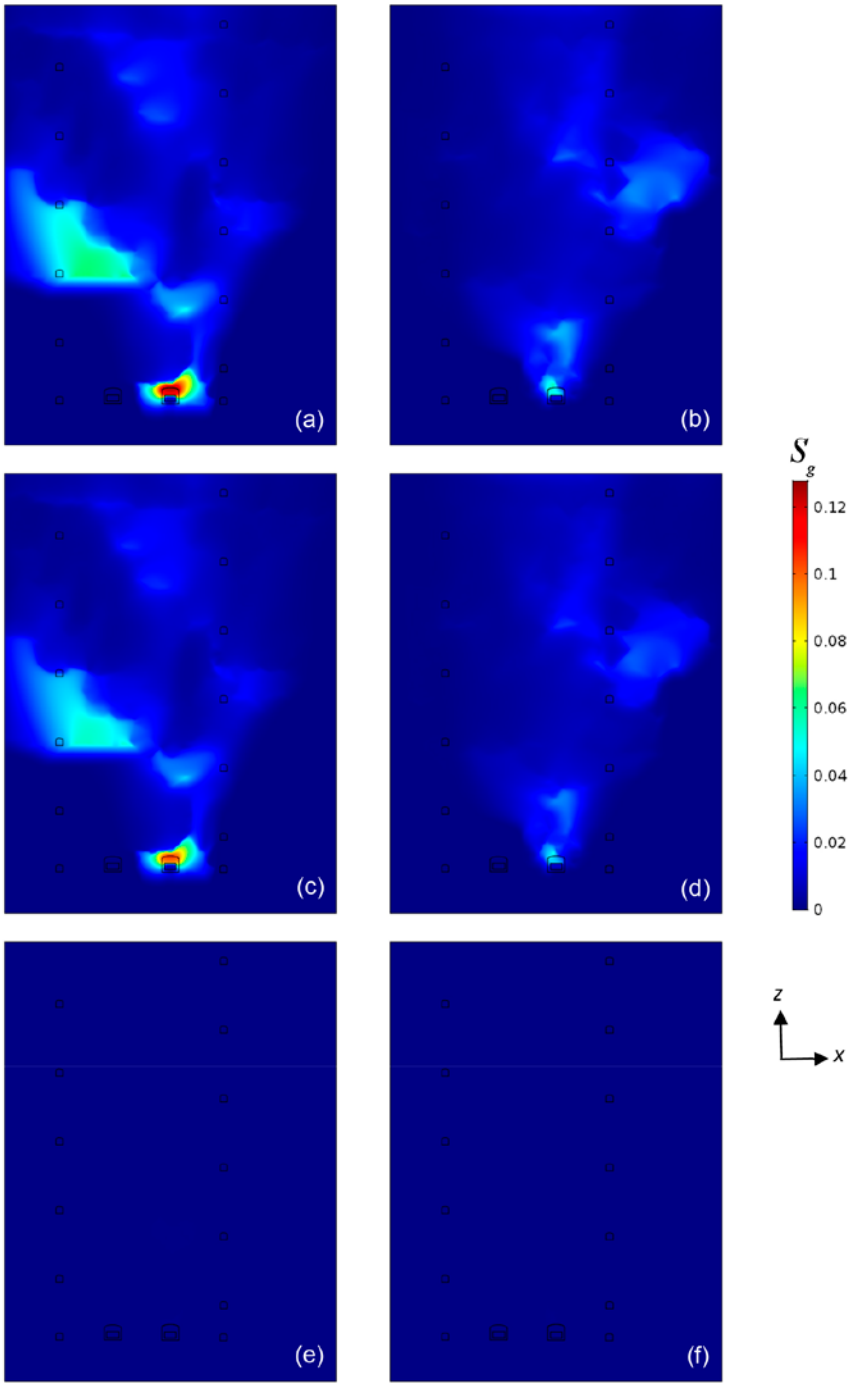

Figure 5-8. *Gas saturation for a gas production rate of $10r_{H2(g)}$ in the Case 20 (left) and Case 21 (right) at (a, b) 7 000 years, (c, d) 60 000 years, (e, f) 100 000 years.*

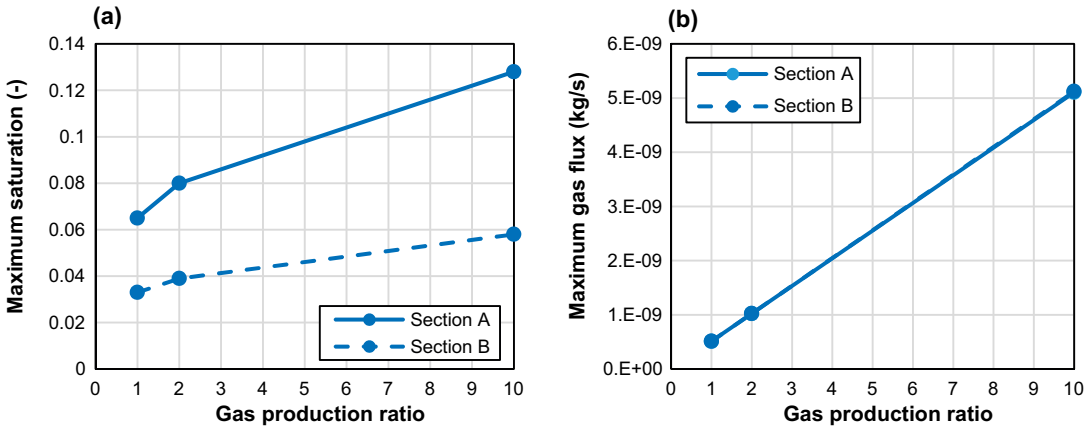

Figure 5-9. *(a) Maximum gas saturation in the domain and (b) maximum total gas flux at the regolith/bedrock interface. The gas production ratio is the quotient between the gas generation rate and the rate considered by Silva et al. (2019).*

On the other hand, the migration of gas in lateral direction is nearly unaffected by increasing the gas production rate in 1.0 order of magnitude (compare Figure 5-8 with Figure 5-1 and Figure 5-2). This is a consequence of the combined effect of: (i) gas buoyancy dominating over groundwater water flow, (ii) zones of very low permeability in the bottom half of the domain (see, e.g. Figure 2-17a) and (iii) the connectivity of more permeable zones mainly through the center of the domain (see, e.g. Figure 2-17b).

5.2.2 Gas fluxes at the regolith-bedrock interface

The gas streamlines simulated with higher gas generation rates are similar to those presented in Section 5.1 (compare Figure 5-10 bottom with Figure 5-3a and b). The gas flows through the same pathways towards the bedrock-regolith interface. Also, the same bimodal and unimodal distributions are observed in the hydrogen fluxes at the top boundary. Despite the higher amount of hydrogen in the system, gas streamlines do not expand much laterally. Most of the gas exits the domain through the top boundary (Table 5-2). The gas footprint at the regolith/bedrock interface, calculated as the area of that surface through which the hydrogen fluxes are higher than 10^{-16} kg/m^2-s, is shown in Figure 5-11. The gas footprint responds to the changes in the gas generation rate due to the different steel corrosion periods. Note that the area of regolith/bedrock interface in the present model is 403.6 m^2. Figure 5-11 shows that the gas footprint is equal or lower than this area for all the gas production rates. For Section A, the maximum gas footprint increases from 386.2 m^2 to 392.2 m^2 and 403.6 m^2, when the gas production rate increases 2 and 10 times, respectively. For Section B, these higher production rates cause the maximum gas footprint to increase from 353.1 m^2 to 360.2 m^2 and 396.2 m^2. Note that Section A includes a zone of high permeability inclined to the left. Part of the gas flows upwards through this zone. This results in a small mass of gas flowing out through the top of the left boundary in Cases 16, 18 and 20 (see sixth column in Table 5-2).

Table 5-2. Total mass of gas leaving the system through each boundary and the percentage that represents.

	Total mass of gas (kg)			% of total gas mass		
Case #	Top boundary	Left boundary	Right boundary	Top boundary	Left boundary	Right boundary
16	1.88E−04	2.20E−07	0.00	99.88	0.12	0.00
17	1.88E−04	0.00	3.94E−09	100.00	0.00	0.00
18	1.88E−04	3.35E−07	0.00	99.82	0.18	0.00
19	1.88E−04	0.00	1.26E−08	99.99	0.00	0.01
20	1.88E−04	6.84E−07	8.42E−11	99.64	0.36	0.00
21	1.88E−04	5.16E−11	7.84E−08	99.96	0.00	0.04

The only relevant difference of the models assuming a faster steel corrosion is the enhanced gas flow. Figure 5-12 shows the influence of gas production rate on the maximum hydrogen gas flux at the regolith-bedrock interface. It is observed that the maximum hydrogen flux increases linearly with the gas production rate. When increasing the rate twice, the maximum flux profile is doubled and when the gas production rate is ten times higher, it increases in a factor of 10. As in Cases 16 and 17, the maximum hydrogen flux for both Sections, A and B, is almost equal for the same gas production rate. The same linear relation between the maximum total gas flux at the regolith/bedrock interface and the gas production ratio is found for Sections A and B (Figure 5-9b).

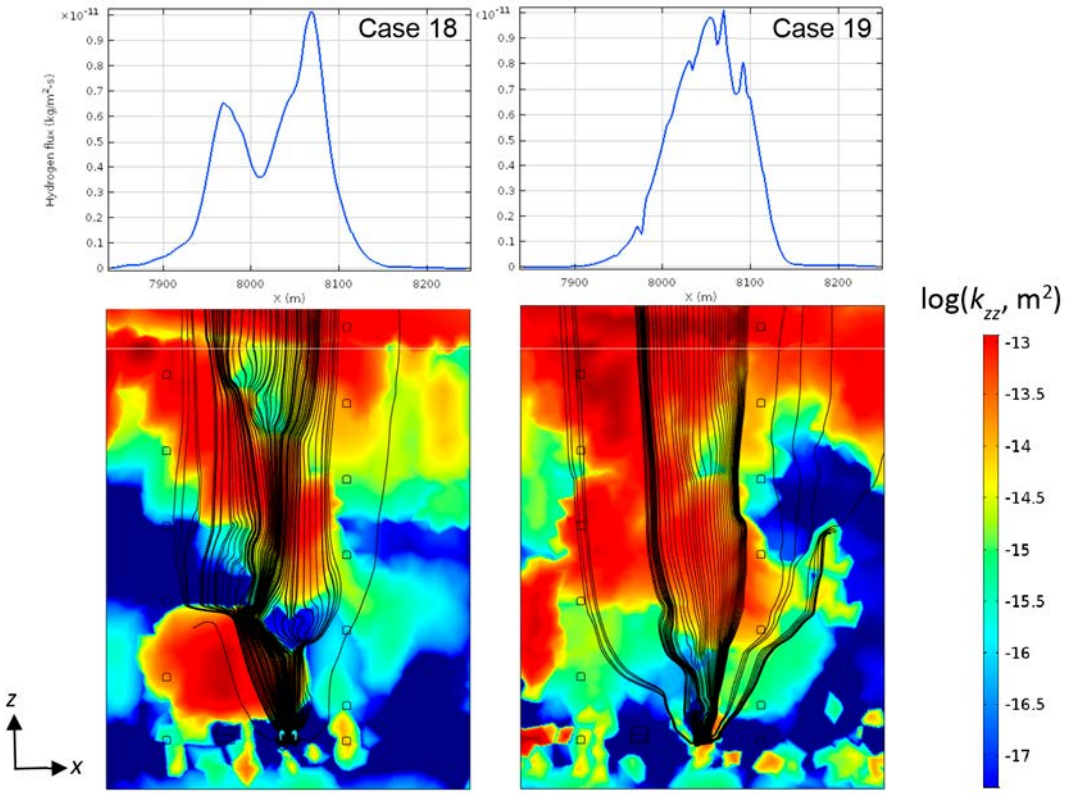

Figure 5-10. *Hydrogen gas flux through the regolith/bedrock interface (top) and gas streamlines crossing the top and lateral boundaries (bottom) at 37 000 years. Vertical permeability is included in the streamlines plot as reference.*

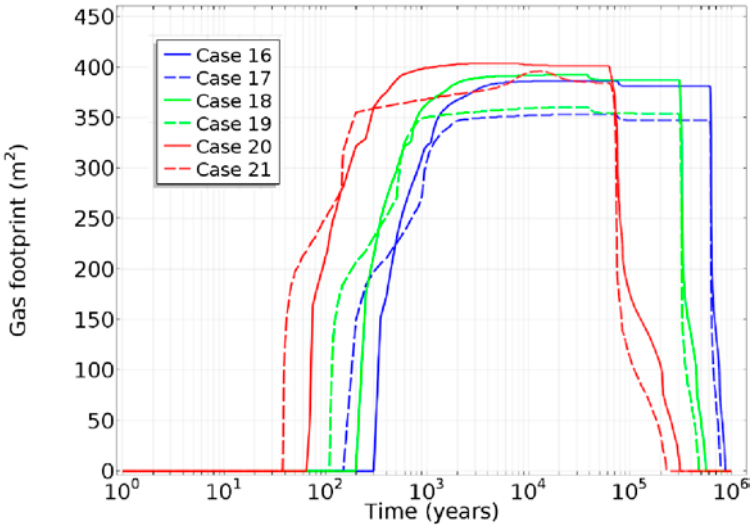

Figure 5-11. *Impact of gas production rate on the gas footprint at the regolith/bedrock interface. Solid and dashed lines are for Section A and Section B, respectively.*

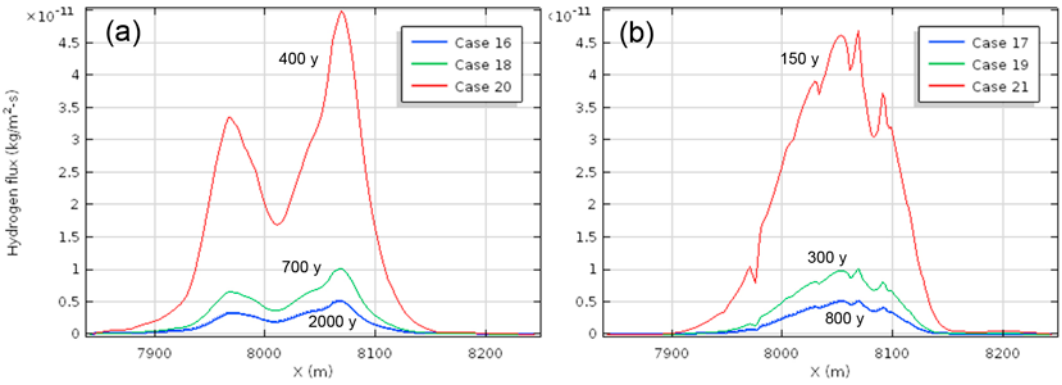

Figure 5-12. *Effect of gas production rate on the maximum gas flux profile at the regolith/bedrock interface for (a) Section A and (b) Section B. The time to reach the maximum is added to the curve of each simulation case.*

The gas production rate controls the gas outflow rates through the regolith-bedrock interface Figure 5-13 shows that, for a given gas production rate, the maximum total hydrogen fluxes are equal, independently of the heterogeneous section considered. The system responds rapidly to the changes in the gas generation rate, arriving to a new steady state for each rate. The outflow of gas through the regolith/bedrock interface of Section B (Cases 17, 19 and 21) is faster than for Section A (Cases 16, 18 and 20). This is due to the greater connectivity of the highly permeable areas in Section B that leads to faster gas flow. The delay in the gas outflow between Cases 16 and 17 is about 150 years. Increasing the gas production rate 2 and 10 times reduces this delay to 80 and 30 years, respectively. Moreover, the times needed to achieve the plateau of maximum hydrogen flux are reduced almost proportionally to the gas production rate increase. These times are about 700 and 300 years in Cases 18 and Case 19, and about 400 and 150 years in Cases 20 and 21.

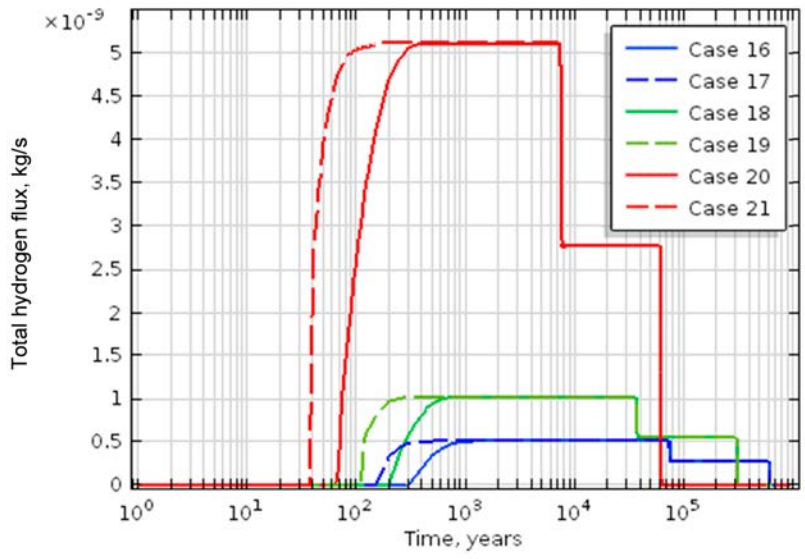

Figure 5-13. *Effect of the gas production rate on the evolution of the total gas flux at the regolith/bedrock interface.*

5.2.3 Effect on groundwater flow

For Cases 16 and 17, the groundwater flows generally downwards and horizontally from left to right (see Figure 2-17). The groundwater concentrates in the zones with a high permeability. In both sections the diagonal highly-permeable area conveys the water from the upper left corner towards the bottom-right. At the left boundary, water flows into the system, except in a high permeable zone in the bottom half of Section B. Water exits the domain at the right boundary excluding the first 100 m of the top where water flows into the domain. This right-to-left current rapidly changes its direction and leaves the system through the upper or right boundary. In the bedrock/regolith interface, the water inflows into the system in the left half and exits in the right half. The water outflow is higher than the inflow in the top boundary. At the bottom boundary, the water outflows the system. Around the vault the groundwater flows downwards. The magnitude of the water flow is higher in the more permeable Section B.

Overall, the groundwater is driven by the regional pressure gradient and little influence of the gas flow is appreciated. Even with a 10 times faster gas generation rate, at the time of higher gas content in the system, no variation is observed in the FF groundwater flow (Figure 5-14). Figure 5-14 shows the groundwater flow through Section B obtained for different gas production rates. Similar conclusions arise from the groundwater flow behavior through Section A. This is because in the FF the gas saturations are lower than 4 % in all the cases (see Figure 5-7 and Figure 5-8).

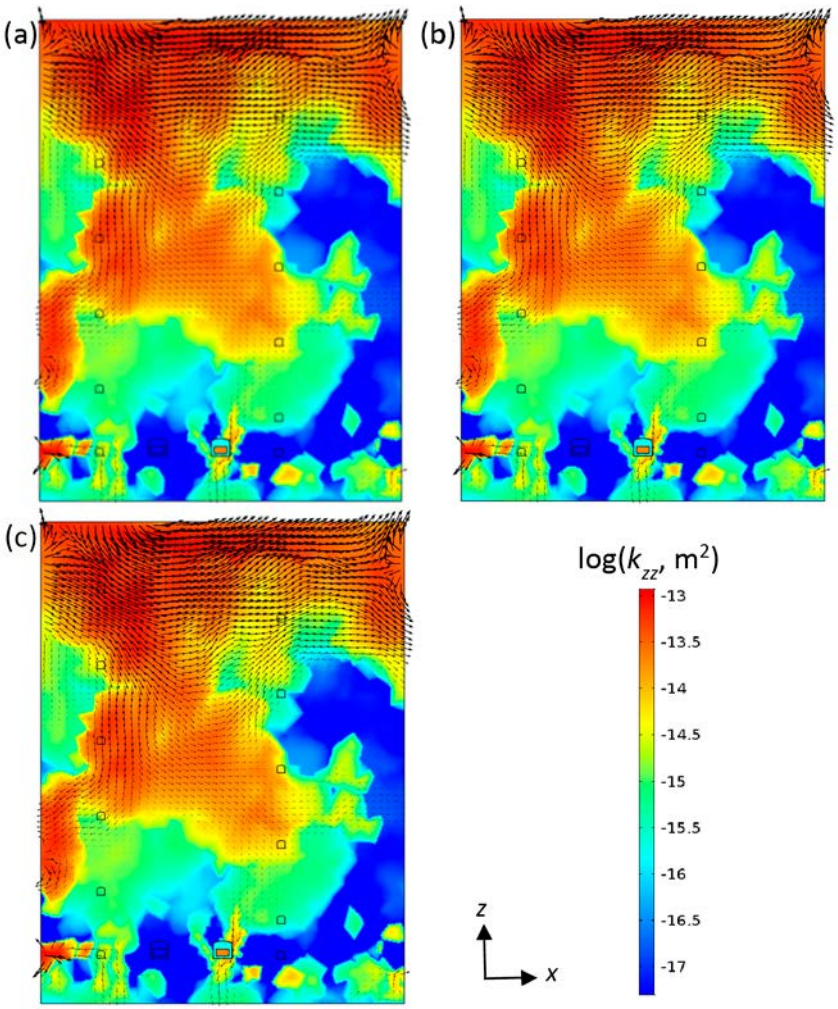

Figure 5-14. *Water velocity fields (black arrows) at the time of maximum gas saturation: (a) Case 17 at 70 000 years, (b) Case 19 at 37 000 years and (c) Case 21 at 7 000 years. Vertical permeability field is included for reference. Arrows are plotted with the same logarithmic scale.*

The total water flux at the bedrock-regolith interface (Figure 5-15) shows only a minor influence of the gas generation rate. The small variation of the groundwater flow is driven by the presence of gas and, consequently, depends directly on the variations of the gas production rate. The more gas is produced, the less water flows through the regolith-bedrock interface. The total water flux adapts rapidly to changes in the gas generation rate due to the different corrosion regimes, arriving to a new steady state for each rate. However, when gas production stops, the total water flux at the regolith-bedrock interface increases gradually. After complete steel consumption, there is still some gas distributed along the domain that continue to migrate towards the surface. This upward gas migration leads to a gradual increase of the total water flux at the regolith/bedrock interface. At the end of the simulations the water flux is lower than initially due to the residual gas content in the porous media. This difference is lower than 0.85 % in all the cases. The different regimes displayed by the total water flux are associated to different regimes in the total hydrogen flux at the regolith-bedrock interface. Therefore, the impact of gas production rate on the duration of each regime is almost the same.

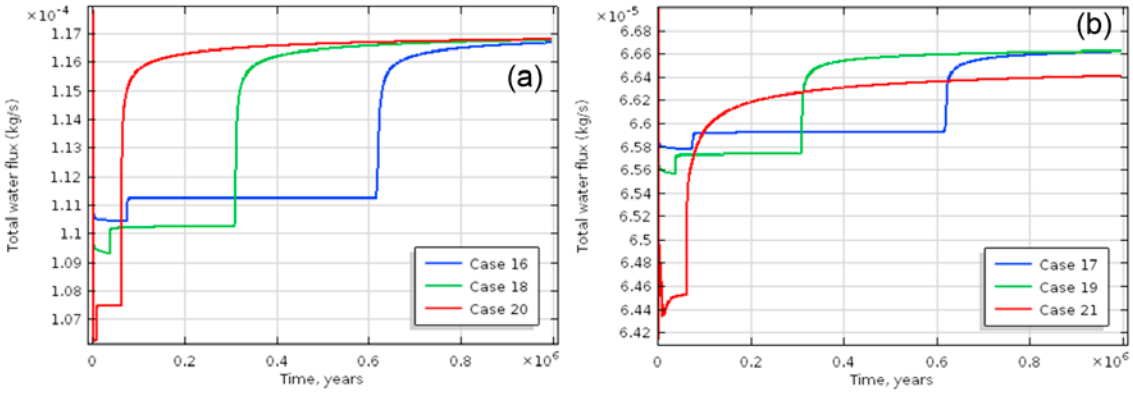

Figure 5-15. *Effect of the gas production rate on the evolution of the total water flux at the regolith/bedrock interface of (a) Section A and (b) Section B.*

6 Conclusions

The two-phase immiscible flow model developed in Silva et al. (2019) was extended to simulate gas release and migration both in the NF and FF of the BHK vault. On one hand, the results of Silva et al. (2019) were complemented in this work by including the effect of: (i) host rock heterogeneity and (ii) higher hydrogen generation rates. Secondly, larger models including the rock heterogeneity and regional groundwater flow were implemented to study the gas release and migration in the FF of the BHK vault. The gas fluxes at the interface between the regolith and bedrock were quantified and the impact of larger gas production rates assessed.

A total of 21 simulation cases were run encompassing different combinations of host rock type and heterogeneity, hydrogen gas production rate and domain scale (NF vs FF). The simulation horizon was 1 000 000 years in all cases. When larger gas production rates are assumed, the different gas generation periods are decreased inversely proportional to the increase in the hydrogen generation rates.

The comparison of the models of gas flow in homogeneous and heterogeneous host rock in the NF points to the following conclusions. First, both homogeneous and heterogeneous host rock models result in the same flow behavior during the first 100 years, when the gas generated flows only within the BHK vault. In general, gas flow in heterogeneous host rock causes higher gas saturations and pressures in the NF of the BHK vault than those simulated with homogeneous rock. Especially, when the vault is surrounded by a very low permeability zone like in Section A the gas accumulates around the vault. Under the above conditions, gas flows through the heterogeneous host rock more slowly than in homogeneous rock. On the contrary, when the heterogeneity of the rock permeability is high, as in Section B, the differences with the homogeneous rock model are minor. This is because the average permeability of the rock adjacent to the vault is close to the permeability assumed in the homogeneous rock model. It can be concluded that gas release from the BHK vault strongly depends on the contrast between the backfill permeability and the average rock permeability. Also, the gas flow within the backfill of the vault is controlled by the permeability contrast between the host rock and the backfill. The rock heterogeneity not only affects the gas release but also its redistribution within the vault, which can affect the evolution of internal pressures. This was demonstrated by comparing the evolution of gas streamlines obtained in simulation Cases 1 to 5. The gas streamlines clearly show how the gas flows through the rock and within the vault. For highly heterogeneous host rock (Section B), the streamlines distribute mainly through zones of high permeability, which clearly indicates preferential pathways for gas flow. For heterogeneous rock with low permeability zones surrounding the vault, the streamlines display a recirculation flow pattern within the vault. This is associated to higher internal gas pressures. Pressures and overpressures obtained in a heterogeneous host rock including very low permeability zones, are about 1.5 bar higher than those obtained when the permeability of a homogeneous rock is relatively high. The gas pressures around the vault are lower than 55 bars. The maximum gas overpressure is in the range of 1.5 to 3.2 bar and is reached when stainless and carbon steel corrode simultaneously.

The presence of fracture zones close to the BHK vault contributes to release the gas faster. This confirms the results already found in Silva et al. (2019) for homogeneous host rock. Particularly, when the vault is embedded into a zone of very low permeability of a heterogeneous host rock, a fracture zone helps to release significantly the internal pressures. The reductions in the average gas pressure and overpressure are 1.5 and 0.5 bar, respectively, when a fracture zone is embedded into the Section A. Reductions in the average gas pressure of about 0.6 bar can be expected for a fracture zone included in the Section B. This estimation comes from the results of Silva et al. (2019) and because the average permeability of the host rock closest to the vault in Section B is close to the permeability of the homogeneous rock. For fracture zone permeabilities similar to the average permeability of the rock closest to the vault, the gas release through the fracture zone is minor. This could be the case for Section B if the permeability would be lower than 10^{-13} m^2.

As in Silva et al. (2019), due to the low gas generation rates, under hydrostatic conditions in a heterogeneous host rock gas production does not affect the water pressure field, and water flow is quasi-stationary through the entire simulation time. In contrast, when Section A includes a fracture zone, the water flow through the fracture zone increases significantly above the zone of very low permeability. In this zone of Section A, the rock permeability is about 1 order of magnitude higher than the permeability of the homogeneous rock. This causes that the liquid Darcy fluxes through the fracture zone in the heterogeneous rock is about 1 order of magnitude higher than when the rock is homogeneous. Because of this and the higher gas flow through the fracture zone, the water flow through the fracture zone is higher than when the rock is homogeneous.

Larger hydrogen gas production rates accelerate the gas flow processes. Hydrogen gas is released faster from the vault, and higher gas saturations are reached around the same zones. As expected, the maximum gas saturations, pressures and gas outflow rates increase proportionally to the increase in the gas generation rate. In the homogeneous rock model, the average pressure in the BHK vault increases about 1.0 bar when the hydrogen generation rate increases 1 order of magnitude. The maximum overpressure in the BHK vault increases in 0.2 and 0.8 bar, when the hydrogen generation rate increases 2 and 10 times, respectively. The impact of larger gas production rates is greater when the host rock is heterogeneous and low permeability zones enclose the vault. For Section A, the average gas pressure increases 0.5 and 2 bar when the hydrogen generation rate increases 2 and 10 times, respectively. These higher production rates cause the maximum overpressure to increase in 0.5 and 1.8 bar. Concerning the model with Section B, increasing the gas production rate in one order of magnitude causes an overpressure increase of 1.0 bar. Silva et al. (2019) showed that for different water flow conditions the BHK vault can withstand internal gas pressures below 61 bars. Based on this, it is concluded that under hydrostatic flow conditions the BHK vault can also withstand pressure buildups caused by gas production rates up to 10 times higher.

The simulations show that, under hydrostatic conditions larger gas production rates do not affect the water pressure field, and water flow is quasi-stationary through the entire simulation time. Also, larger gas production rates have an impact on water flow close to the vault when the Section A includes a fracture zone. Increasing the gas production rate by a factor of 10 causes an increase of approximately 42 % in the water flow through and around the fracture zone. Higher gas flow through the fracture zone displaces the water flow region upwards. Moreover, larger gas production rates reduce the water flowrates through the vault and waste in about 3 % and 10 % when the gas production rate increases to $2r_{H2(g)}$ and $10r_{H2(g)}$, respectively. In addition, the maximum gas saturations that can be expected are about 12 % if the gas production rate is 10 times higher than that assumed by Silva et al. (2019). The assumption of fully saturated conditions for radionuclide transport analysis would be unrealistic under these high gas production rates.

The results of the FF simulation cases show that buoyancy is the main driving force for gas flow and there is little influence of the regional groundwater flow. The gas flows upwards preferentially through highly permeable zones and accumulates in areas with low permeability. If the highly permeable areas are connected, the gas migrates fast towards the surface. In contrast, when these highly permeable areas are separated by low permeable zones, the gas requires more time to find a pathway towards the surface. In this case, gas accumulation in low permeable disconnected zones can be a source of a long-term residual gas content. The simulations showed that higher gas flows and lower saturations are found in the more connected Section B than in the less permeable Section A.

The gas pathways are relatively straight even for the less connected host rock Section A. Most of the gas (more than 99 %) leaves the model domain through the bedrock/regolith interface. The gas streamlines distribution displays the preferential pathways followed by the gas. In Section A the flow of gas at the regolith is more dispersed than in Section B. Also, the distribution of hydrogen flux at the regolith/bedrock interface is significantly affected by the host rock permeability field below that boundary. Uniform distributions of rock permeability close to the regolith (Section B) cause unimodal distributions of hydrogen fluxes. Heterogeneous rock permeability (Section A) leads to a bimodal distribution of hydrogen fluxes, with peaks and valleys located over more and less permeable zones, respectively. The maximum gas footprint at the regolith/bedrock interface is 386.2 m^2 for Section A and 353.1 m^2 for Section B.

Gas flow depends directly on the gas production rate and the heterogeneity of the rock permeability, which affects the gas breakthrough at the regolith-bedrock interface. This causes that a larger amount of gas leaves the system through Section B than through Section A. However, the maximum total gas flux at the regolith-bedrock interface reached during each corrosion regime is independent of the permeability field. The system responds rapidly to the changes in the gas generation rate, arriving to a new steady state for each rate. Simulation cases considering the less connected Section A, arrive to the steady state a little later than the cases considering Section B. In the very long-term, when no gas is generated the gas saturation in host rock, especially in Section B, tends to zero. The low permeability zones in Section A that promote the accumulation of gas in the rock lead to a small residual gas content in the long-term.

Higher gas production rates cause similar gas distributions and gas flow than lower production rates. The only difference is the magnitude of the gas saturation and flow. The maximum total hydrogen flux through the regolith/bedrock interface increases linearly with the gas production rate and does not depend on the permeability field. For Section A, increasing the gas generation rate by a factor of 2 and 10 causes the maximum gas footprint at the regolith/bedrock interface to increase up to 392.2 m^2 and 403.6 m^2, respectively. For Section B, the maximum gas footprint increases up to 360.2 m^2 and 396.2 m^2 when the gas production rate increases 2 and 10 times, respectively. The maximum gas saturation in the system increases around an 100 % when the gas production rate increases in one order of magnitude. Gas migration and distribution has little influence on the groundwater flow. Even considering very high gas generation rates, the gas saturations in the system are too low (below 13 %) to affect the groundwater.

It should be noted that the present 2D models do not capture totally the regional groundwater flow. There might be connections between highly permeable zones of the rock in the longitudinal direction to the vaults. Those connections would affect the water and gas migration in the area. The impact of the highly permeable materials of the access tunnels could be especially significant. 3D models with a full description of the hydraulic conductivities can give a more accurate estimation of the internal pressures in the vaults. The assessment of the impact of gas on the regolith would also be improved.

The results of the present work suggest that heterogeneous host rock including high permeable and fracture zones intersecting the BHK vault are advisable from the safety point of view. For the evaluated repository conditions, the above rock features favor the gas release and keep the overpressures in the vault low.

References

SKB's (Svensk Kärnbränslehantering AB) publications can be found at www.skb.com/publications.

Abarca E, Sampietro D, Miret M, von Schenck H, 2016. Initial modelling of the near-field hydrogeology. Exploring the influence of host rock characteristics and barrier properties. Report for the safety evaluation SE-SFL. SKB R-16-02, Svensk Kärnbränslehantering AB.

Abarca E, Sampietro D, Molinero J, 2019. Modelling of the near-field hydrogeology – Temperate climate conditions. Report for the safety evaluation SE-SFL, SKB R-19-03, Svensk Kärnbränslehantering AB.

Amec, 2014. ConnectFlow Technical Summary, Release 11.2. AMEC/ENV/CONNECTFLOW/15, AMEC, UK.

Baroghel-Bouny V, Mainguy M, Lassabatere T, Coussy O, 1999. Characterization and identification of equilibrium and transfer moisture properties for ordinary and high performance cementitious materials. Cement and Concrete Research 29, 1225–1238.

Bear J, Bachmat Y, 1991. Introduction to modeling of transport phenomena in porous media, printed in Dordrecht by Kluwer.

Chung T H, Ajlan M, Lee L L, Starling K E, 1988. Generalized multiparameter correlation for nonpolar and polar fluid transport properties. Industrial & Engineering Chemistry Research 27, 671–679.

Elfwing M, Evins L Z, Gontier M, Grahm P, Mårtensson P, Tunbrant S, 2013. SFL concept study. Main report. SKB TR-13-14, Svensk Kärnbränslehantering AB.

Finsterle S, Pruess K, 1995. Solving the estimation-identification problem in two-phase flow modeling. Water Resources Research 31, 913–924.

Hjerne C, Nordqvist R, Harrström J, 2010. Compilation and analyses of results from cross-hole tracer tests with conservative tracers. SKB R-09-28, Svensk Kärnbränslehantering AB.

Jarsjö J, Destouni G, Gale J, 2001. Groundwater degassing and two-phase flow in fractured rock: Summary of results and conclusions achieved during the period 1994–2000. SKB TR-01-13, Svensk Kärnbränslehantering AB.

Joyce S, Appleyard P, Hartley L, Tsitsopoulos V, Woollard H, Marsic N, Sidborn M, Crawford J, 2019. Groundwater flow and reactive transport modelling of temperate conditions. Report for the safety evaluation SE-SFL. SKB R-19-02, Svensk Kärnbränslehantering AB.

Lindström M, Lundqvist J, Lundqvist T, 2000. Sveriges geologi från urtid till nutid. 2nd ed. Lund: Studentlitteratur.

Peng D-Y, Robinson D B, 1976. A new two-constant equation of state. Industrial & Engineering Chemistry Fundamentals 15, 59–64.

Rhén I, Forsmark T, Hartley L, Jackson P, Roberts D, Swan D, Gylling B, 2008. Hydrogeological conceptualisation and parameterisation. Site descriptive modelling, SDM-Site Laxemar. SKB R-08-78, Svensk Kärnbränslehantering AB.

Silva O, Coene E, Molinero J, Laviña M, Idiart A, 2019. Gas release from the BHK vault – Multiphase flow modelling of the near-field. Report for the safety evaluation SE-SFL. SKB R-19-06, Svensk Kärnbränslehantering AB.

SKB, 2014. Data report for the safety assessment SR-PSU. SKB TR-14-10, Svensk Kärnbränslehantering AB.

van Genuchten M T, 1980. A closed-form equation for predicting the hydraulic conductivity of unsaturated flow. Soil Science Society American Journal 44, 892–898.

Vidstrand P, Rhén I, 2011. On the role of model depth and hydraulic properties for groundwater flow modelling during glacial climate conditions. SKB R-10-74, Svensk Kärnbränslehantering AB.

Vidstrand P, Rhén I, Zugec N, 2010. Groundwater flow modelling of periods with periglacial and glacial climate conditions – Laxemar. SKB R-09-25, Svensk Kärnbränslehantering AB.

Xu T, Senger R, Finsterle S, 2008. Corrosion-induced gas generation in a nuclear waste repository: Reactive geochemistry and multiphase flow effects. Applied Geochemistry 23, 3423–3433.

Appendix A

Internal gas pressures

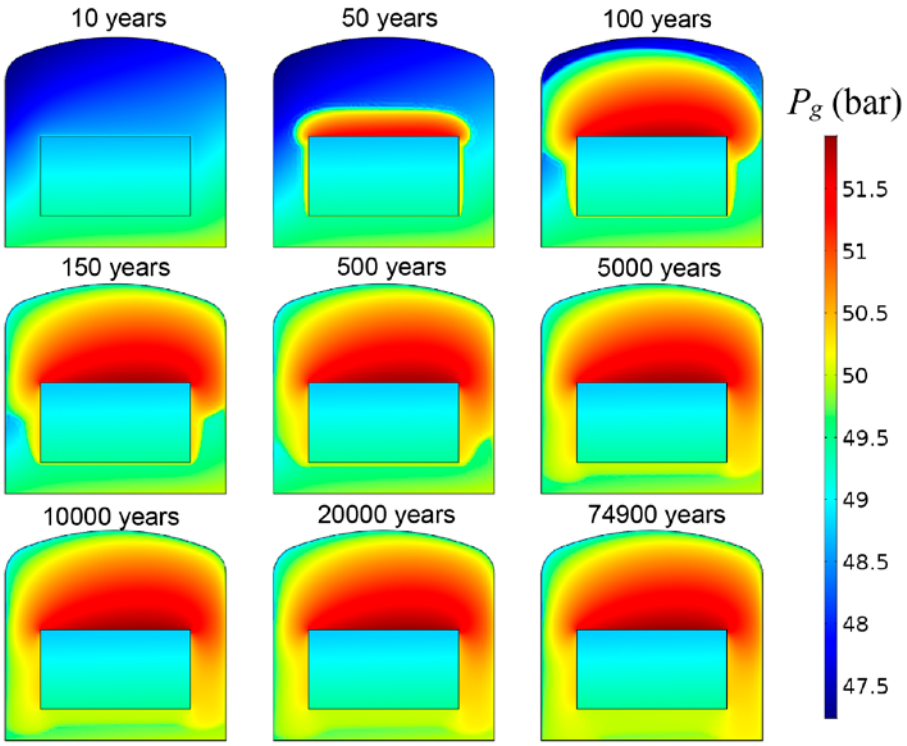

Figure A-1. *Evolution of the gas pressure within the BHK vault during the stainless-steel corrosion period obtained in Case 2.*

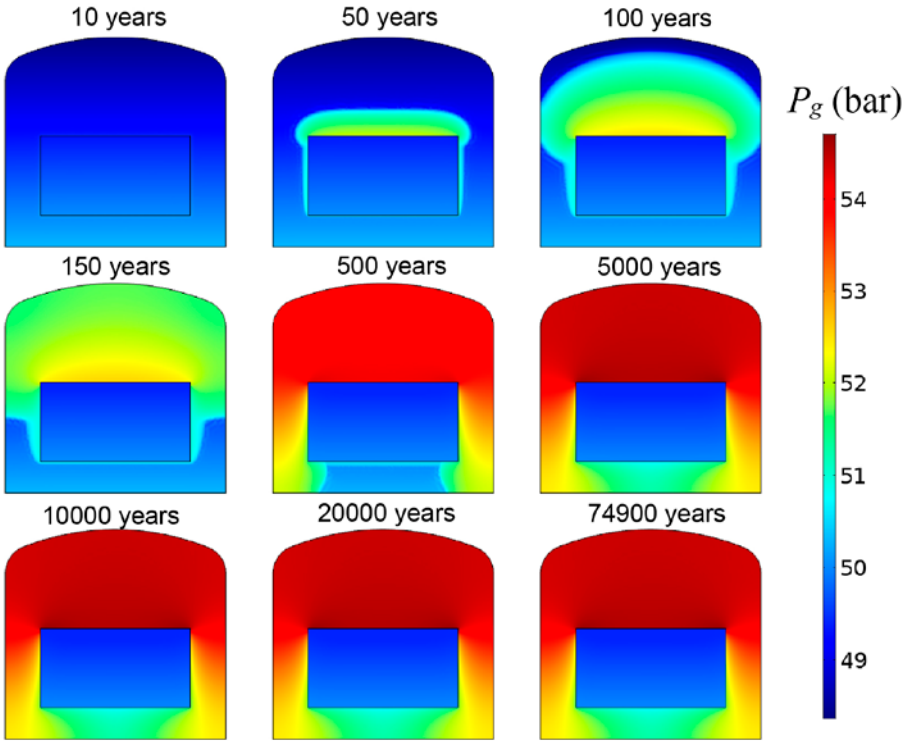

Figure A-2. *Evolution of the gas pressure within the BHK vault during the stainless-steel corrosion period obtained in Case 3.*

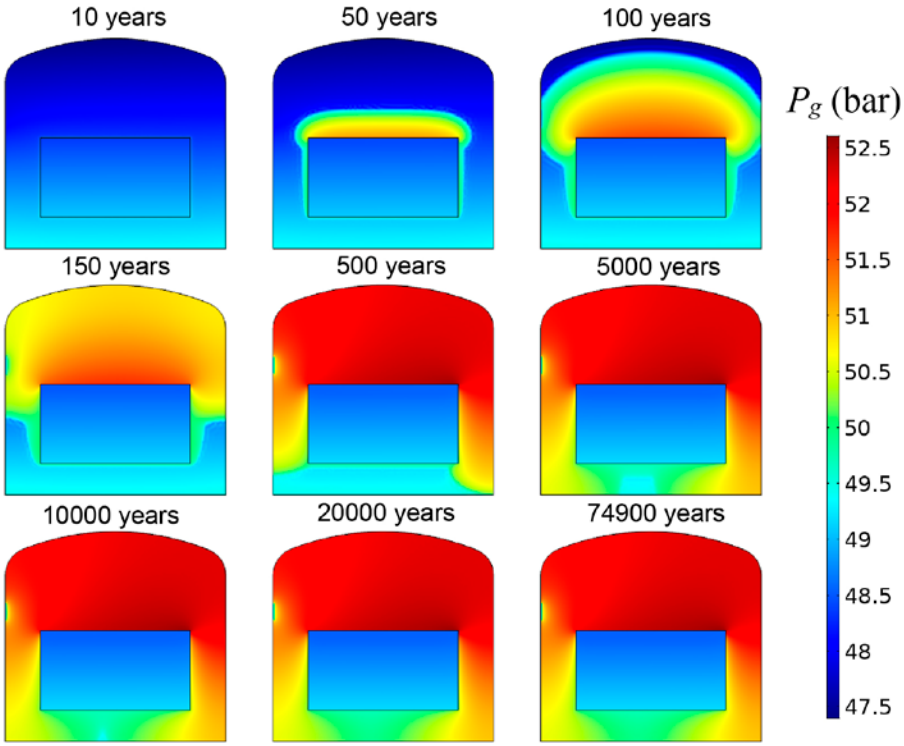

Figure A-3. *Evolution of the gas pressure within the BHK vault during the stainless-steel corrosion period obtained in Case 5.*